
Paleoenvironmental Signatures of Aeolian and Fluvial Sedimentary End-Members off NW Africa

Dissertation

Zur Erlangung
des Doktorgrades der Naturwissenschaften

am Fachbereich Geowissenschaften
der Universität Bremen

vorgelegt von

Janna Just

- 1. Gutachter:** Prof. Dr. Tilo von Dobeneck, Universität Bremen
- 2. Gutachter:** Dr. Mark J. Dekkers, Universität Utrecht

Januar 2012

Declaration

Name: Janna Just

Address: Olgastraße 18, 28203 Bremen

Herewith I declare that

- I. This document and the accompanying data has been composed by myself, and describes my own work
- II. Material from the published or unpublished work of others, which is referred to in the dissertation, is credited to the author in the text
- III. This work has not been submitted for any other degree

Bremen, 31th January, 2012

.....

(Signature)

Summary

Assessing the multi-proxy characteristics of terrigenous sediments is an essential step in the aim to distinguish and quantify aeolian and fluvial inputs to the oceans. The reconstruction of these fluxes enables paleoclimatic reconstructions, i.e., more arid conditions are reflected by higher aeolian input and more humid conditions by higher fluvial input. Moreover, the characteristics of fluvial and aeolian sediments mirror the environmental conditions in the source areas and also the physical conditions during transport.

This thesis presents a new approach to characterize and cross-validate the multi-parameter properties of fluvial and aeolian material deposited at the continental margin at the border of arid and subtropical Africa. Grain-size distributions, geochemical compositions, and magnetic parameters of core material from off the Gambia (GeoB 13602-1, 13°32.71' N, 17°50.96' W) and Senegal Rivers (GeoB 9508-5, 15°29.90' N; 17°56.88' W) were analyzed. End-member unmixing was performed for each data set to obtain the mixing coefficients and properties of terrigenous fractions. The multi-parameters properties of the terrigenous fractions could be reconstructed by non-negative least square fitting between the volumetric contributions of grain-size EMs and the geochemical and magnetic data. Based on the volumetric EM representations, the approach additionally enabled to budget fluxes of aeolian and fluvial material over the past 70 ka.

The statistical analyses elucidate that off the Gambia and Senegal Rivers the aeolian and, respectively, the fluvial sediments have comparable grain sizes and geochemical composition, while their magnetic mineral assemblage differs. It is suggested that the source-to-sink distance influences the grain-size distribution of the accumulated fluvial sediments. Consequently, sea-level variations have a strong impact on the accumulation at the continental margin. Precipitation in the hinterland, i.e., water discharge of the river, additionally influences the accumulation, and has a first-order impact during sea-level stagnancy. For aeolian material, the grain-size distribution is dependent on wind strength and distance to the source area. Since the weathering conditions (physical or chemical) influence the major element composition of terrigenous fractions, the distinction of fluvial and aeolian fractions originating from areas with contrasting climatic environments was possible. The formation of pedogenic magnetic minerals is very sensitive to the humidity and temperature of soils, pH, and organic matter content. Therefore, the variability of the magnetic inventory allows a more specific distinction of different sources than the major element geochemical composition. It is inferred that the magnetic mineralogy of fluvial material off the Gambia and Senegal Rivers

expresses the differences in the soil composition of both catchments. Distinct magnetic properties of the aeolian end-members indicate that dust is derived from at least three source areas. At both core locations coarse dust transported by the NE trade winds accumulated. The magnetic mineralogy suggests that this coarse dust comes from two different source regions. A finer aeolian end-member was unraveled off the Senegal River, which originates from a more distant dust source and was probably transported by the African Easterly Jet.

During the Last Glacial Maximum fluxes of proximal dust from the continent were ~5 times higher than during the Late Holocene, indicating a wider extent of the desert and stronger winds. Extremely dry conditions prevailed on the African continent coinciding with Heinrich Events in the North Atlantic. During the respective Heinrich Stadials, the ratio of aeolian vs. fluvial material was even higher. The highest dust accumulation of $400 \text{ g m}^{-2}\text{yr}^{-1}$ occurred during HS 1 which corresponds to a 100 times higher flux with respect to the Late Holocene. Such high values of dust accumulation have not been reported yet off NW Africa. This finding emphasizes that short term disturbances of the meridional overturning circulation, arising from fresh-water input during Heinrich Events, cause dramatic environmental changes also in low-latitudes.

Kurzfassung

Die Multi-Proxy Charakterisierung terrigener Sedimente ist ein wichtiger Schritt um den Eintrag von Staub und fluviatitem Material ins Meer zu quantifizieren. Da trockene Bedingungen auf dem Kontinent mit erhöhtem Staubeintrag und feuchte Bedingungen mit erhöhtem Flusseintrag einher gehen, ermöglicht deren quantitative Auswertung paläoklimatische Rekonstruktionen. Darüber hinaus spiegeln die Eigenschaften von wind- und flustransportiertem Material die Umweltbedingungen an Land und die physikalischen Transportmechanismen wider.

In dieser Arbeit wird ein neuer Ansatz vorgestellt, um Multi-Parameter Eigenschaften von äolischem und fluviatitem Material, das am Nordwest afrikanischen Kontinentalrand abgelagert wurde, zu charakterisieren und zu validieren. Die marinen Sedimentkerne wurden vor der Mündung des Gambia (GeoB13602-1, 13°32.71' N, 17°50.96' W) und des Senegal (GeoB9508-5, 15°29.90' N; 17°56.88' W), an der Grenze der ariden und subtropischen Klimazonen gewonnen. Korngrößen-Verteilungen, die geochemische Zusammensetzung und magnetische Parameter wurden gemessen. An jedem dieser Datensätze konnten mit Hilfe statistischer Methoden die Eigenschaften und Mischungsverhältnisse terrigener End-Member bestimmt werden. Basierend auf den Volumenanteilen von Korngrößen End-Membren und den geochemischen und magnetischen Datensätzen wurden Multi-Parameter Eigenschaften berechnet werden. Hierfür diente die Methode der kleinsten Fehlerquadrate mit nicht-negativer Randbedingung. Die volumenbezogenen Mischungsverhältnisse der terrigenen End-Member ermöglichten neben der Rekonstruktion der Multi-Parameter Eigenschaften auch eine Budgetierung des äolischen und fluviatilen Eintrags über die vergangenen 70 ka.

Die statistischen Analysen zeigen dass vor der Mündung des Gambia und des Senegal die äolisch und fluviatil eingetragenen Sedimente jeweils vergleichbare Korngrößen und geochemische Zusammensetzungen haben, sich jedoch in ihrer magnetischen Mineralogie unterscheiden. Es wird angenommen das die *source-to-sink* Entfernung die Korngrößen Verteilung der fluviatil eingetragenen Sedimente steuert. Dadurch haben Meeresspiegelschwankungen einen starken Einfluss. Änderungen des Niederschlags im Hinterland beeinflussen die Akkumulation vorwiegend während Stagnationen des Meeresspiegels. Die Korngrößen von äolischem Material sind neben der *source-to-sink* Entfernung auch von der Windstärke beeinflusst.

Die geochemische Zusammensetzung der terrigenen Fraktionen ist abhängig von den Verwitterungsbedingungen (chemisch oder physikalisch), die in den Staubquellen und Einzugsgebieten der Flüsse vorherrschen. Da äolische und fluviatile Sedimente aus Regionen gegensätzlicher Klima-

zonen angeliefert werden, können sie durch ihre geochemische Zusammensetzung unterschieden werden.

Die Entstehung pedogener magnetischer Minerale hängt von der Bodenfeuchtigkeit und -temperatur sowie vom pH Wert und Anteil von organischem Material ab. Daher ermöglicht eine Analyse der Magnetomineral-Vergesellschaftung eine spezifischere Unterscheidung von Quellgebieten als die Hauptelement-Zusammensetzung. Die Verschiedenheit der magnetischen Mineralogie der fluviatilen End-Member des Gambias und Senegals scheint die Bodeneigenschaften in den Einzugsgebieten widerzuspiegeln. Die magnetischen Eigenschaften der identifizierten äolischen End-Member legen ebenfalls nahe, dass die Staubfraktionen aus wenigstens drei unterschiedlichen Regionen stammen: An beiden Lokationen wurde proximaler Staub, vermutlich durch die Passatwinde transportiert, abgelagert. Auch diese beiden proximalen Staub End-Member haben unterschiedliche magnetische Mineralogien und kommen aus verschiedenen Regionen. Ein feinkörnigeres äolischen End-Member wurde vor der Mündung des Senegal identifiziert. Dieser Staub stammt von einer distalen Staubquelle und wurde vermutlich durch den African Easterly Jet transportiert.

Während des letzten Glazialen Maximums war die Akkumulation von proximalem Staub ~ 5 -mal höher als während des späten Holozäns. Dies spricht für eine weite Ausdehnung von Wüstengebieten und stärkere oder langanhaltendere Winde. Extrem trockene Bedingungen in NW Afrika gehen mit nordatlantischen Heinrich Ereignissen einher. Während der jeweiligen Heinrich Stadiale war das Verhältnis von Fluss- zu Staubeintrag noch niedriger als während des Letzten Glazialen Maximums. Die höchste Staubakkumulationsrate von $400 \text{ g m}^{-2} \text{ yr}^{-1}$; wurde für Heinrich Stadial 1 berechnet. Dies entspricht einem 100 fach höherem Eintrag als während des späten Holozäns. Solch hohe Werte wurden bisher noch nicht für NW Afrika berichtet. Die extrem hohe Staubakkumulation belegt, dass kurzzeitige Störungen der Tiefenwasserproduktion im Nordatlantik durch Frischwasserzufuhr während der Heinrich Ereignisse Auswirkungen auf die klimatischen Bedingungen in niedrigen Breiten hatten.

Acknowledgements

First of all, I would like to thank Prof. Tilo von Dobeneck for his support during the entire three years. It is amazing how your innovative ideas and confidence in my abilities motivated me to get excited in rock-magnetism so that I rose to the challenge of working with statistical methods. I am very grateful to Dr. Mark J. Dekkers for all his effort and patience as well as his intensive and constructive discussions. I benefitted so much from your experiences. I thank Dr. Torsten Bickert for finding an opportunity for me to do a PhD project in the EUROPROX Graduate School. I thank you for all the support and suggestions over the three years. For introducing and helping me with the statistical methods and being patient until all my questions were answered, I thank Dr. Dave Heslop very much.

I am grateful for Prof. Willems as chair of EUROPROX International Graduate College and all EUROPROX members for fruitful discussions during the Coffee and Science meetings. Particularly, I thank Matthias Zabel and Inka Meyer for scientific support.

Thanks to the Fort Hoofddijk people from Utrecht University for having me there for two months. I had a really productive and pleasant time! Especially, I would like to thank Prof. Cor Langereis for offering me a home and for discussing scientific topics over a glass of wine and also Tom Mullender for helping with measurements and discussing results.

Dear Marine Geophysics Group, Liane Brück, Christian Hilgenfeldt, Thomas Frederichs, Hendrik Müller, Heike Piero, Benjamin Baasch, Cletus Itambi, Firoz Kader Badesap, Lucy Korff, Sebastian Razik, Vera-Barbara Bender and Martina Braun: I felt very home with you and thank you for scientific discussions, coffee and distractions while swimming in the Wümme and rolling the balls. You are the best!!! I especially acknowledge the technical and scientific support of Liane, Christian and Thomas. I think, now I know which buttons have to be pushed. Vera, I had a nice time while we were sharing the same the office and enjoyed our coffee breaks. Benni, I am so glad that you like statistics and I am thankful for all your help.

I also like to thank my family Gerhard and Steffen Just and Liane Kringel not only because they were not upset for not getting Christmas presents in 2011 but also for their mental support and trust in me over the three years as well as for the easy time I had when I was visiting Nord Hessen.

I thank the HGLD-group (for whatever that means) Linda, Miriam and Wisa for discussing (scientific) problems with me and refreshing breaks. Last but not least I thank many other PhD students of FB 5. I especially like to mention Bene, Ines, Lutz and Katja. I am happy to know you and thank you for the fun times after work and on the weekends.

And of course I thank all my friends from 'outside' university, especially Laura, Kati, Jenny, Benni, Nina, for the nice weekends in Hamburg and Bremen. Stephan, I thank you for all your support and that you always listened to my problems and for everything else.

This cumulative PhD thesis is embedded in research project 13B of the International Graduate College EUROPROX *Proxies in Earth History*. The studies compiled in the thesis were carried out from February 2009 to January 2011 at the Department of Geosciences at the University of Bremen.

After a general Introduction and the presentation of the objectives of the studies in Chapter 1, three research papers will be presented in Chapter 2, 3, 4. In Chapter 5, general conclusions arising from the studies follow.

Appendix A contains a published manuscript on the Messinian Salinity Crisis. This paper results from my Diploma Thesis and was compiled during my first months at the University of Bremen as a PhD student.

Table of Contents

Chapter 1 - Introduction	1
1.1 Motivation and Objectives	1
1.2 Climatic conditions in NW Africa	4
1.3 Terrigenous material	4
1.3.1 <i>Fluvial material</i>	5
1.3.2 <i>Aeolian material</i>	5
1.4 Proxy data provenance vs. transport	6
1.4.1 <i>Major elements</i>	6
1.4.2 <i>Magnetic mineralogy</i>	7
1.5 Approach and Thesis Outline	8
Chapter 2 - Unmixing signatures of aeolian, fluvial, bacterial and diagenetic magnetic mineral fractions in Late Quaternary marine sediments off Gambia, NW Africa	13
2.1 Introduction	14
2.2 Geological and hydrographic setting	16
2.3 Materials and chronology	17
2.4 Methods	18
2.4.1 <i>Rock Magnetism</i>	18
2.4.2 <i>Scanning and transmission electron microscopy</i>	19
2.4.3 <i>Numerical unmixing</i>	20
2.5 Results	22
2.5.1 <i>Room temperature magnetic measurements</i>	22
2.5.2 <i>End-member analysis</i>	23
2.5.3 <i>IRM component analysis</i>	26
2.5.4 <i>Additional rock magnetic analyses</i>	28
2.6 Discussion	31
2.6.1 <i>Aeolian signature</i>	31
2.6.2 <i>Fluvial signature</i>	33
2.6.3 <i>Bacterial signature</i>	33
2.6.4 <i>Diagenetic signature</i>	34
2.6.5 <i>Paleoclimatic implications</i>	35
2.7 Conclusions	38
Chapter 3 - Multi-proxy characterization and budgeting of terrigenous end-members at the NW African continental margin	45
3.1 Introduction	46
3.1.1 <i>Materials</i>	47
3.1.2 <i>Source areas and transport of terrigenous material</i>	48
3.2 Methods	49
3.2.1 <i>Geochemistry</i>	49
3.2.2 <i>Grain-size analysis</i>	49

3.2.3 <i>Dry bulk density and mass accumulation rates</i>	50
3.2.4 <i>End-member analysis</i>	50
3.3 Results	51
3.3.1 <i>Geochemistry</i>	51
3.3.2 <i>Grain-size distribution</i>	51
3.3.3 <i>Differences and similarities in proxy records</i>	51
3.4 End-member unmixing	53
3.4.1 <i>Element end-members</i>	53
3.4.2 <i>Grain-size end-members</i>	55
3.4.3 <i>Comparison of the end-member models</i>	55
3.5 Multi-proxy approach	55
3.5.1 <i>Multi-proxy properties</i>	58
3.6 Discussion	58
3.6.1 <i>Multi-proxy characteristics of terrigenous end-members</i>	58
3.6.2 <i>Budgeting the accumulation of terrigenous end-members</i>	59
3.6.3 <i>Source areas and transport processes</i>	61
3.7 Conclusion	64
Chapter 4 - Paleoenvironmental influence on the multi-proxy characteristics of terrigenous sediments off NW Africa	
4.1 Introduction	70
4.2 Setting	71
4.3 Material and Methods	72
4.3.1 <i>Rock magnetic measurements</i>	73
4.3.2 <i>End-member unmixing</i>	73
4.3.3 <i>Multi-proxy approach and volume calibration</i>	74
4.4 Results	75
4.4.1 <i>Rock magnetic parameters</i>	75
4.4.2 <i>EM Analyses</i>	75
4.4.3 <i>Multi-proxy characteristics of grain-size end-members</i>	78
4.5. Discussion	80
4.5.1 <i>Interpretation of end-members in GeoB 9508-5</i>	80
4.5.2 <i>Associated properties of grain-size end-members</i>	81
4.5.3 <i>Differing signatures of terrigenous material off Gambia and Senegal</i>	82
4.6. Conclusion	85
Chapter 5 - Synthesis	89
5.1 Grain-size distribution	89
5.2 Major element composition	89
5.3 Magnetic mineralogy	90
5.4 Multi-proxy characteristics	90
5.5 Paleoclimatic implications revealed by end-member analyses	91

Appendix A - Erosion of continental margins in the Western Mediterranean due to sea-level stagnancy during the Messinian Salinity Crisis

1. Introduction

Assessing the factors for desertification in low latitudes and the feedback of expanding deserts on the climate system are important tasks in the evaluation of future climate change. In the recent past, droughts in Africa were apparently controlled by sea-surface temperature anomalies in the Atlantic Ocean (Folland et al. 1986). Future predictions of oceanic circulation indicate a slowing of the Meridional Overturning Circulation (MOC) due to an increase in anthropogenic CO₂ (IPCC 2007). Such disturbances can lead to a cooling of the Atlantic Ocean, to a southward shift of the Inter Tropical Convergence Zone (ITCZ) and thus to an aridification in low latitudes (Dahl et al. 2005).

Expanding deserts and, consequently, enhanced dust concentrations in the atmosphere would change the Earth's radiation budget. For areas with high (i.e., deserts, ice caps) or low albedo (i.e., oceans, forests), dust in the atmosphere results in a warming or, respectively, cooling of the earth surface (Harrison et al. 2001). In the case of the N African continent this albedo effect of dust leads to an enhanced temperature gradient between continent and ocean, and thus, represents a positive feedback mechanism. Additionally, dust particles act as condensation nuclei and therefore contribute to the formation of clouds which also affect the albedo (Shine

and Forster 1999). Iron-rich dust exported to the ocean is a fertilizer and enhances ocean bioproductivity and carbon removal from surface waters. This process is important for the regulation of atmospheric CO₂ (Harrison et al., 2001 and references therein).

To evaluate future impacts of MOC weakening for low-latitude climate, it is worthwhile to investigate the low-latitude response on past changes of oceanic circulation. Terrigenous sediments exported to the oceans represent an excellent archive of paleoclimatic conditions on the continent. Proxy data measured on marine sediments provide information of the environmental conditions in the source areas of the sediments and additionally reflect transport mechanisms and thus, variations in fluvial and aeolian fluxes.

1.1 Motivation and Objectives

During the past decades, the glacial and interglacial climate history of the African continent has been studied by means of various proxy records in marine sediment cores. Changes in grain-size distributions (e.g., Koopmann 1981), elemental ratios (e.g., Matthewson et al. 1995) and environmental magnetic parameters (Bloemendal et al. 1988; Bloemendal et al. 1992) of marine sediments were shown to provide information

about variations of fluvial and aeolian sediment supply to the Eastern Atlantic Ocean. Palynological studies (Lézine and Hooghiemstra 1990; Dupont and Agwu 1992) and reconstructions of vegetation types from the isotopic composition of plant waxes (Schefuß et al. 2005; Niedermeyer et al. 2010; Collins et al. 2011) have been successfully used to reconstruct the retreat and expansion of vegetation zones.

When terrigenous proxies are used to reconstruct variations in the sediment supply from the continent, all factors and processes affecting sediment composition from source to sink (Fig. 1-1) must be considered:

- (1) Lithology of the parent material
- (2) Weathering and pedogenic conditions in the source area
- (3) Gravitational sorting during transport and deposition
- (4) Post-depositional alteration, e.g., dissolution and remineralization

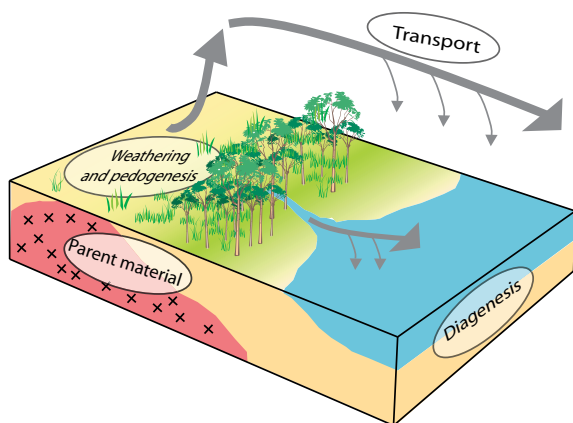


Fig. 1-1: Schematic overview of factors and processes influencing terrigenous sediments from source-to-sink.

Grain sizes of terrigenous material mirror the availability of a certain grain-size class in the source area, the imparted transport energy and the settling conditions. The geochemical composition reflects the properties of the soils in the source area but may be biased by gravitational sorting during transport (Caquineau et al. 1998). The magnetic mineralogy of terrigenous sediments depends on the magnetic inventory of the parent material and on the formation of pedogenic minerals in the source areas (Maher 1986). Because magnetic minerals are associated with physical grain-size classes (Lyons et al. 2010), they are also subject to gravitational sorting during transport (Bloemendal et al. 1992). The complexity of influencing factors on the proxy records in sediments can be assessed by a multi-parameter characterization of the various terrigenous fluxes.

Since the knowledge about relative climate variations for NW Africa is well established, the quantitative assessment of past climatic changes is a challenging task. Recently, Collins et al. (submitted) used δD of plant waxes as a calibrated indicator for past precipitation. The analytical methods are time-consuming and thus inapplicable for high resolution records of past climatic changes. Alternatively, flux changes of aeolian and fluvial material can be used to assess the range of environmental change on the continent. Such studies of past terrigenous fluxes are compiled in the DIRTMAP project (Kohfeld and Harrison 2001). This compilation mainly focuses on specific time slices as

the Last Glacial Maximum (LGM) and the Late Holocene.

Marine sediments represent mixtures of biogenic and terrigenous sediment components from numerous sources, which have to be identified and quantified. End-member (EM) modeling (Weltje 1997) is a suitable method in the aim of unmixing a data set into a given number of components. EM unmixing is an inverse technique, for which the properties and the mixing coefficients are taken as *a priori* unknown.

Grain-size distributions and, respectively, grain-size EMs, can help to estimate volume contributions of terrigenous components derived by different transport regimes. However,

as outlined above, in contrast to geochemical or magnetic properties, grain-size distributions depend mainly on the transport energies and thus cannot serve for source material characterization.

This thesis introduces a novel technique for assessing multi-proxy characteristics of terrigenous EMs. The approach combines EM unmixing and multivariate statistical methods to obtain associated properties for volume related EM contributions. The approach enables the identification of material originating from different provenances and their related transport mechanisms. Additionally, environmental

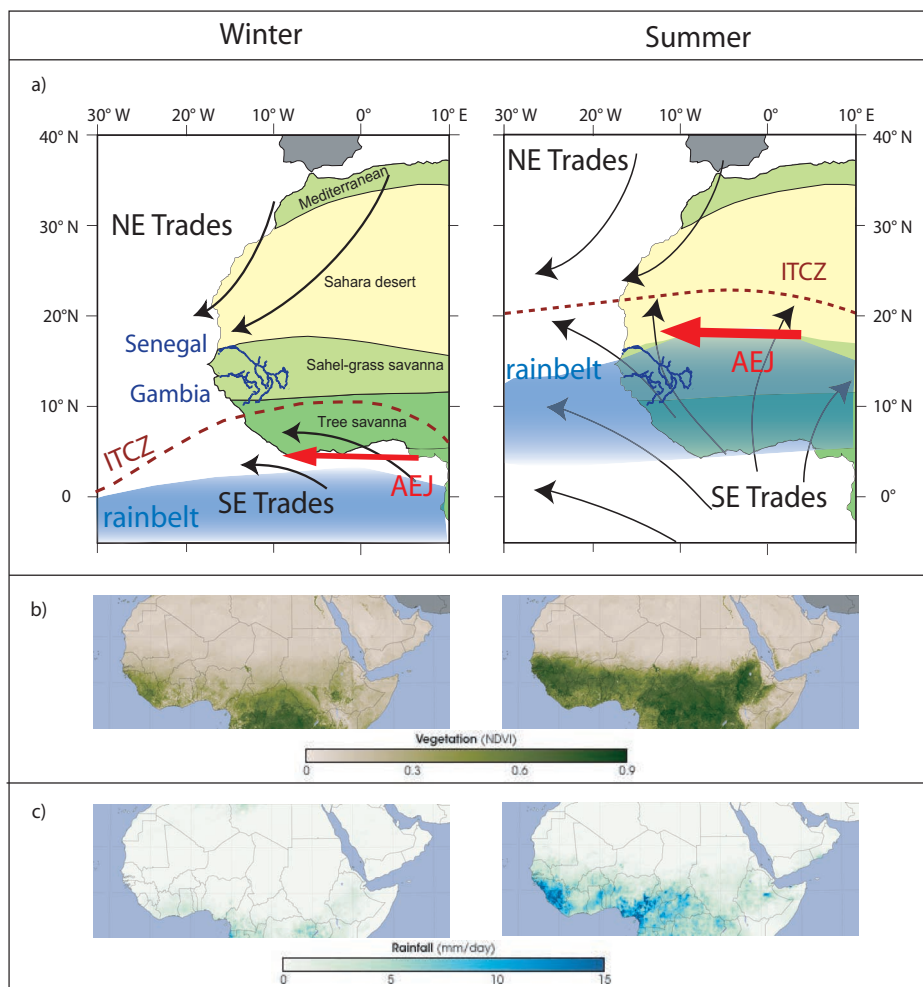


Fig. 1-2: (a) Vegetation zones (White, 1986, modified after Castaneda et al., 2009) and atmospheric features of the West African continent. (b) Seasonal differences in vegetation of subtropical Africa results from the rainfall distribution (c) induced by the migration of the rainbelt (data from <http://earthobservatory.nasa.gov/>). AEJ: African Easterly Jet, ITCZ: Intertropical Convergence Zone.

conditions in the different source areas can be reconstructed. After the identification of aeolian and fluvial EMs, based on the volumetric contributions of each EM, fluxes of aeolian and fluvial material will be calculated.

1.2 Climatic conditions in NW Africa

The climatic conditions of the African continent are controlled by the seasonal migration of the ITCZ, at which the NE and SE trade winds converge, and the associated rain belt (Fig. 1-2 a). The seasonal migration of the ITCZ induces a reorganization of the atmospheric features, leading to a strong seasonality with highest precipitation (Fig. 1-2 b, c) and thus river runoff during boreal summer and a dry and dusty season during winter. Two mechanisms control precipitation in West Africa (Nicholson 2009): Converging trade winds are responsible for

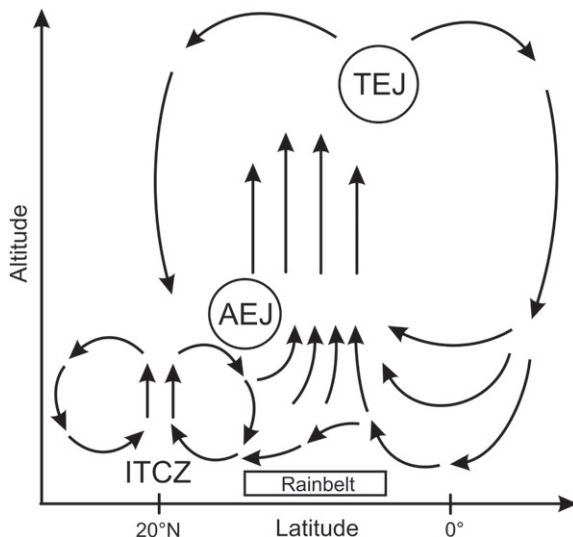


Fig. 1-3: Atmospheric circulation and position of the rainbelt. Maximum rainfall results from ascending air between the African Easterly Jet (AEJ) and Tropical Easterly Jet (TEJ). ITCZ: Intertropical Convergence Zone. From Nicholson 2009; Zarriess and Mackensen 2010.

rainfall over the southern Sahara and northern Sahel. However, maximum precipitation at the African rainbelt results from ascending humid air between the mid-tropospheric African Easterly Jet (AEJ) and the high-tropospheric Tropical Easterly Jet (TEJ, Fig. 1-3).

Paleoclimatic reconstructions reveal that during the LGM, the north African continent experienced much drier conditions with respect to the present (Koopmann 1981; Sarnthein et al. 1981). Numerical models suggest that low temperatures in the North Atlantic during the LGM caused a southward shift of the ITCZ (Chiang and Bitz 2005) and associated atmospheric features. Accordingly, wet-season length and annual precipitation were reduced in North Africa (Collins et al. 2011). Even drier conditions on the N African continent were induced by North Atlantic Heinrich Events during Dansgaard-Oeschger Stadials (Jullien et al. 2007; Mulitza et al. 2008; Itambi et al. 2009). It is suggested that the freshwater input in the North Atlantic led to disturbances of the MOC causing a southward shift of the ITCZ (Street-Perrott and Perrott 1990; Dahl et al. 2005).

1.3 Terrigenous material

Terrigenous sediments exported to the continental margin of NW Africa encompass fluvial material which in our study area is transported by the Gambia and the Senegal Rivers and to dust from the Sahara and Sahel (Fig. 1-2 a).

1.3.1 Fluvial material

The Senegal drains an area of 268,000 km² (Kattan et al. 1987) that is dominated upstream by subtropical climate (savanna vegetation). Downstream, the Senegal flows at the southern border to the desert (Fig. 1-2 a). In contrast, the drainage basin of the Gambia is as small as 78,000 km² and is located in the subtropical zone with savanna vegetation (Lesack et al. 1984). Due to the high seasonality associated with the migration of the ITCZ, the water discharge of the Senegal and Gambia Rivers varies throughout the year. This is also expressed in the volume of particle transport in both rivers: During the rainy season from July to October the concentration of suspended matter at two

stations at the Senegal and Gambia Rivers is 1.5 and 3 times higher, respectively, than during the dry season (Gac et al. 1987).

1.3.2 Aeolian material

The Sahara desert is the most important source of aeolian material of the world. Estimates of emitted dust particles from NW Africa vary between 120 Tg yr⁻¹ and 720 Tg yr⁻¹ (Engelstaedter et al. 2006 and references therein). The most important dust sources in the Sahara are the Bodélé Depression in Chad, a large area in eastern Mauritania, and temporally dry salt lakes, the “chotts”, in Algeria and Tunisia (Prospero et al. 2002). Dust entrainment depends on environmental and atmospheric conditions in the source

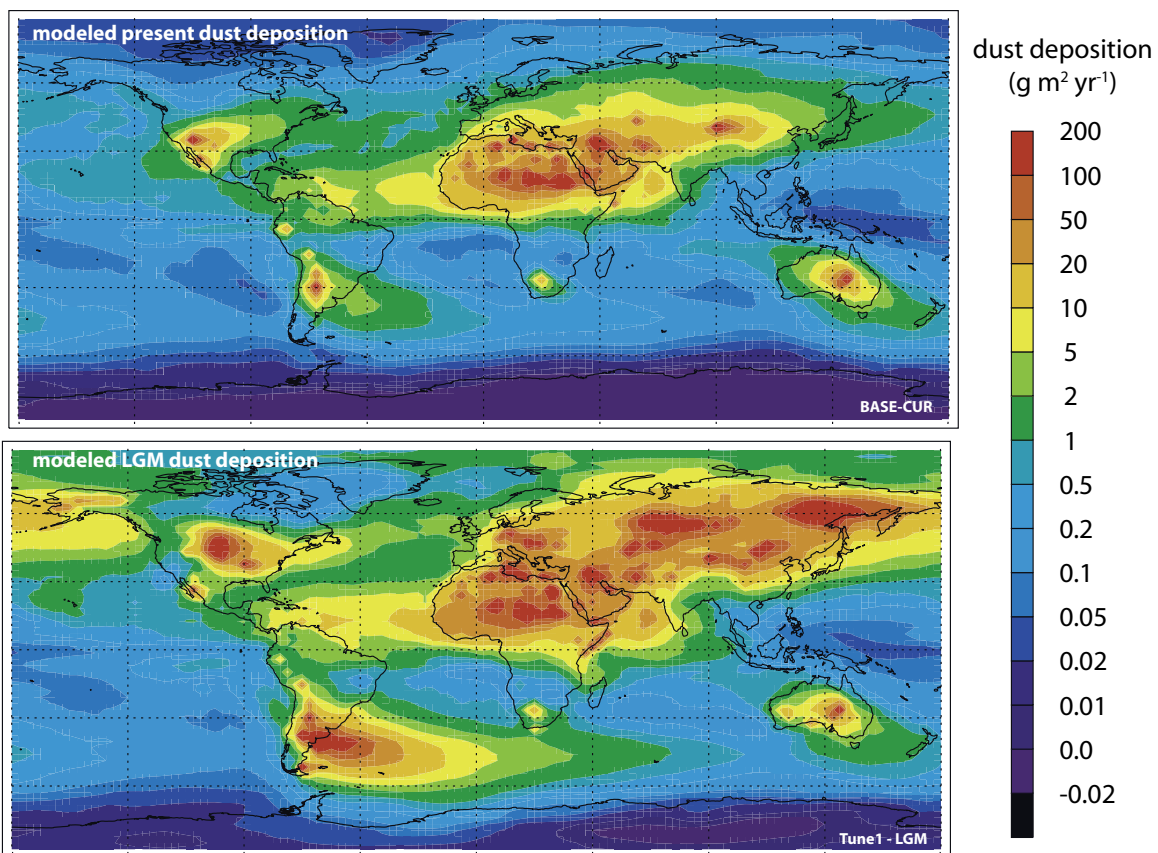


Fig. 1-4: Modeled global dust deposition rates for today and for the Last Glacial Maximum (LGM; Mahowald et al., 2006).

area. The grain sizes of the sediments (Pye 1987), soil moisture and vegetation cover (Chepil and Woodruff 1963) influence the threshold shear strength needed for aeolian deflation. In NW Africa the trade winds constitute the dominant dust transport mechanism during winter, when the ITCZ is located at its southernmost position (Fig. 1-2a). When uplifted, dust of Saharan and Sahelian regions is transported by the NE trade winds at altitudes of 500-1500 m and is exported to the proximal Atlantic Ocean (Pye 1987; Chiapello et al. 1995). Additionally, dust is transported within the higher (up to 3 km) Saharan Air Layer (Sarnthein et al. 1981) and can potentially be transported over the Atlantic Ocean as far as to the Caribbean (Prospero and Carlson 1972). The transport at these altitudes is mainly attributed to the propagation of Easterly Waves, constituting the AEJ and TEJ (Nicholson 2009).

In the proximal Atlantic Ocean off NW Africa modeled deposition rates of dust vary between 5 and 10 g m⁻² yr⁻¹ (Fig. 1-4, Mahowald et al. 2006). This in accordance to analyses of marine surface samples and material collected in sediment traps (Kohfeld and Harrison 2001). During the LGM, dust deposition was 2 to 10 times higher than at present (Kohfeld and Harrison 2001). A higher temperature gradient and thus stronger winds (Sarnthein et al. 1981), and a reduced vegetation cover due to dry conditions (Mahowald et al. 2006) are thought to be responsible for this phenomenon.

1.4 Proxy data provenance vs. transport

1.4.1 Major elements

To track dust samples back to their source areas, satellite images as well as backward trajectories are used. Also, soil samples from potential dust areas are analyzed and compared with the mineralogical and geochemical composition of dust collected close to the African continent and at the western side of the Atlantic Ocean (e.g. Chiapello et al. 1995; Chiapello et al. 1997; Caquineau et al. 1998; Grousset et al. 1998; Caquineau et al. 2002; Chiapello et al. 2005; Stuut et al. 2005).

Dust collected on the Canary Islands has different geochemical signatures, mirroring Moroccan (Al/Si ~ 0.36) and Sahelian (Al/Si ~ 0.29) source areas (Bergametti et al. 1989). Dust emitted from three different sectors over NW Africa was sampled on the Cape Verde Isles (Chiapello et al. 1997). For those samples the Al/Si ratio is highest for dust from the Sahel (0.49), moderate for central Saharan dust (0.45) and lowest for a north and west Saharan origin (0.43). The elemental ratios derived by both studies converge significantly. This points out that some attention has to be paid when using major element proxies for determining the provenance of dust without any further information as satellite images and trajectories. Seemingly, the sampling location and thus transport distance to the source area and/or transport energy (i.e., wind speeds) appears to have an impact on the geochemical signatures. Studies focusing on the influence of transport distance on the mineralogical compo-

sition reveal that the contribution of quartz with respect to mica and kaolinite decreases during long range transport (Glaccum and Prospero 1980). These differences are explained by gravitational fractionation during transport, since coarse grained particles, as quartz, settle much faster than clay. Similar conclusions are drawn by Caquineau et al. (1998; 2002) who analyzed the mineralogy of dust samples collected on the Cape Verdes. They found variable Al/Si ratios of dust samples derived from the same source sectors on the African continent. Consequently, this ratio is not applicable for a differentiation of source areas. Moreover, difficulties for the comparison of present-day dust samples and the signatures of dust in marine sediments arise. Often, dust samples are collected at different places and reflect single dust events (e.g., Stuut et al. 2005). Satellite imaginary and backward trajectories reveal, however, that changes in the wind conditions happen rapidly and dust is often a mixture of re-mobilized material from different areas (Guieu et al. 2002). The dust signature that is conserved in marine sediment cores corresponds to a more averaged signal. However, it is reasonable that the signatures of dust in marine samples could potentially be indicative of super-regional displacements of dust sources, especially when the source regions are subject to differing weathering conditions.

1.4.2 Magnetic mineralogy

As suggested by Bloemendal et al. (1988; 1992), the primary magnetic mineralogy of terrigenous

sediments is controlled by two factors: First, the variability in magnetic mineral content reflects changing contributions from different source areas with distinct magnetic inventories. Second, if magnetic minerals occur as or are associated with certain physical grain-size classes (e.g. hematite coatings on quartz grains), they are subject to gravitational fractionation during transport resulting in enrichments or, respectively, depletions.

There are two different approaches for discriminating terrigenous sediments based on their magnetic mineralogy. First, the characterization of detrital magnetic particles (Hounslow and Maher 1996) or inclusions in host grains (Hounslow and Morton 2004; Maher et al. 2009) can be used to link sediments to the parent rock. Second, the investigation of specific magnetic minerals which are formed during pedogenesis enable the discrimination of source areas, that are dominated by differing environmental conditions, i.e., weathering (Harris and Mix 1999).

Lyons et al. (2010) published magnetic data from potential source areas of dust (soils and sands) in central NW and subtropical Africa. They focused on pedogenic magnetic minerals and linked their occurrence and formation to spatial precipitation variations. As already observed from Chinese loess/palaeosol sequences (Maher et al. 1994; Maher and Thompson 1995), a clear relationship in the formation of fine and ultra-fine magnetite with increasing precipitation is suggested (Lyons et al. 2010). A detailed analysis of magnetic properties of dif-

ferent grain-size classes shows that the magnetic minerals are highly concentrated in the clay fraction. In the Sahelian samples, especially the high-coercivity magnetic minerals (goethite and hematite) peak within the clay fraction (Lyons et al. 2010). In contrast, in the Saharan samples those magnetic phases peak within the coarse sediment fraction ($> 63\mu\text{m}$). These findings reveal that also the magnetic mineralogy of terrigenous sediments from the African continent can potentially be used to discriminate sediments derived from different source regions.

1.5 Approach and Thesis Outline

The aim of this thesis is a quantitative assessment of the properties of terrigenous sediments off NW Africa to detect changing provenance and to budget the fluxes of sediments derived by fluvial and aeolian pathways.

To better constrain the use of proxies for paleoclimatic reconstructions the following general questions arise:

- Which proxies are good discriminators for the terrigenous fraction from different sources?
- Which information about the climatic and environmental conditions in the source area can be inferred from the properties of terrigenous sediments?
- How do properties of fluvial and aeolian material vary on a regional scale?

After the evaluation of the source-to-sink processes, paleoclimatic questions may be addressed:

- How did the fluxes of aeolian material vary over the past 70 ka?
- Which information do variations of terrigenous fluxes reveal about the climatic conditions on the continent?
- How and to what extent are the climatic conditions on the African continent linked to the global climate system?

To address these questions, this thesis includes the following manuscripts.

Chapter 2: Unmixing signatures of aeolian, fluvial, bacterial and diagenetic magnetic mineral fractions in Late Quaternary marine sediments off Gambia, NW Africa

In this manuscript, analytical methods (detailed rock-magnetic measurements and electron microscopy) are combined with end-member unmixing of isothermal remanent magnetization acquisition curves. The combination of all methods reveals the magnetic characteristics of terrigenous sedimentary components and enables an evaluation of the impact of post-depositional formation or reductive dissolution on the magnetic inventory.

Chapter 3: Multi-proxy characterization and budgeting of terrigenous end-members at the NW African continental margin

A multi-proxy approach which enables the characterization of aeolian and fluvial sediments deposited off the Gambia River by means of grain-size distributions and associated major element composition and magnetic mineralogy will be introduced. On this basis, proxies for source area and transport can be distinguished. Based on the volumetric proportion of the EMs, fluxes of aeolian and riverine sediments can be calculated and set into context with the paleoclimatic development of the NW African continent.

Chapter 4: Paleoenvironmental influence on the multi-proxy properties of terrigenous sediments off NW Africa

In this study we apply the multi-proxy strategy on material retrieved off the Senegal River. Based on differing properties of fluvial and aeolian end-members off the Senegal and Gambia Rivers, it is discussed which generic proxies are feasible to discriminate between terrigenous fractions, while others can be used to infer specific information about the environmental conditions of particular source areas.

References

- Bergametti, G., L. Gomes, G. Coude-Gaussen, P. Rognon, and M.-N. Le Coustumer (1989), African Dust Observed over Canary Islands: Source-Regions Identification and Transport Pattern for some Summer Situations, *J. Geophys. Res.*, 94(D12), 14855-14864.
- Bloemendal, J., B. Lamb, and J. King (1988), Paleoenvironmental implications of rock-magnetic properties of late Quarternary sediment cores from the eastern equatorial Atlantic, *Paleoceanography*, 3(1), 61-87.
- Bloemendal, J., J. W. King, F. R. Hall, and S. J. Doh (1992), Rock Magnetism of Late Neogene and Pleistocene deep-sea sediments: Relationship to sediment source, diagenetic processes, and sediment lithology, *J. Geophys. Res.*, 97, 4361-4375.
- Caquineau, S., A. Gaudichet, L. Gomes, and M. Legrand (2002), Mineralogy of Saharan dust transported over northwestern tropical Atlantic Ocean in relation to source regions, *J. Geophys. Res.*, 107(D15), 4251.
- Caquineau, S., A. Gaudichet, L. Gomes, M.-C. Magonthier, and B. Chatenet (1998), Saharan dust: Clay ratio as a relevant tracer to assess the origin of soil derived aerosols, *Geophys. Res. Lett.*, 25(7), 983-986.
- Chepil, W. S., and N. P. Woodruff (1963), The physics of wind erosion and its control.
- Chiang, J., and C. Bitz (2005), Influence of high latitude ice cover on the marine Intertropical Convergence Zone, *Climate Dynamics*, 25(5), 477-496.
- Chiapello, I., C. Moulin, and J. M. Prospero (2005), Understanding the long-term variability of African dust transport across the Atlantic as recorded in both Barbados surface concentrations and large-scale Total Ozone Mapping Spectrometer (TOMS) optical thickness, *J. Geophys. Res.-Atmos.*, 110(D18), 9.
- Chiapello, I., G. Bergametti, B. Chatenet, P. Bousquet, F. Dulac, and E. S. Soares (1997), Origins of African dust transported over the northeastern tropical Atlantic, *J. Geophys. Res.*, 102(D12), 13701-13709.
- Chiapello, I., G. Bergametti, L. Gomes, B. Chatenet, F. Dulac, J. Pimenta, and E. S. Soares (1995), An additional low layer transport of Sahelian and Saharan dust over the northeastern Tropical Atlantic, *Geophys. Res. Lett.*, 22(23), 3191-3194.
- Collins, J. A., E. Schefuß, S. Mulitza, M. Prange, M. Werner, T. Thejna, A. Paul, and G. Wefer (submitted), African rainbelt intensity since the Last Glacial Maximum from hydrogen isotopes of plant waxes, *Quat. Sci. Rev.*
- Collins, J. A., et al. (2011), Interhemispheric symmetry of the tropical African rainbelt over the past 23,000 years, *Nature Geosci.*, 4(1), 42-45.
- Dahl, K. A., A. J. Broccoli, and R. J. Stouffer (2005), Assessing the role of North Atlantic freshwater forcing in millennial scale climate variability: a tropical Atlantic perspective, *Clim. Dyn.*, 24(4), 325-346.
- Dupont, L. M., and C. O. C. Agwu (1992), Latitudinal shifts of forest and savanna in N. W. Africa during the Brunhes chron: further marine palynological results from site M 16415 (9°N 19°W), *Veget. Hist. Archaeobot.*, 1(3), 163-175.
- Engelstaedter, S., I. Tegen, and R. Washington (2006), North African dust emissions and transport, *Earth Sci. Rev.*, 79(1-2), 73-100.
- Folland, C. K., T. N. Palmer, and D. E. Parker (1986),

- Sahel rainfall and worldwide sea temperatures, 1901-85, *Nature*, 320(6063), 602-607.
- Gac, J.-Y., J.-M. Bouchez, B. S. Bamba, M. Carn, D. Orange, and P. Duvert (1987), *Géochimie des eaux du Fouta-Djalon : flux dissous et particuliers en Haute Gambie (Kédougou et Gouloumbou) : contribution à la monographie de la Gambie*, AP : Autres productions Rep., 143 pp, ORSTOM, Montpellier.
- Glaccum, R. A., and J. M. Prospero (1980), Saharan aerosols over the tropical North Atlantic -- Mineralogy, *Mar. Geol.*, 37(3-4), 295-321.
- Grousset, F. E., M. Parra, A. Bory, P. Martinez, P. Bertrand, G. Shimmield, and R. M. Ellam (1998), Saharan wind regimes traced by the Sr-Nd isotopic composition of subtropical Atlantic sediments: Last Glacial Maximum vs today, *Quat. Sci. Rev.*, 17(4-5), 395-409.
- Guieu, C., M. D. Loÿe-Pilot, C. Ridame, and C. Thomas (2002), Chemical characterization of the Saharan dust end-member: Some biogeochemical implications for the western Mediterranean Sea, *J. Geophys. Res.*, 107(D15), 4258.
- Harris, S. E., and A. C. Mix (1999), Pleistocene precipitation balance in the Amazon basin recorded in deep sea sediments, *Quat. Res.*, 51(1), 14-26.
- Harrison, S. P., K. E. Kohfeld, C. Roelandt, and T. Claquin (2001), The role of dust in climate changes today, at the last glacial maximum and in the future, *Earth Sci. Rev.*, 54(1-3), 43-80.
- Hounslow, M. W., and B. A. Maher (1996), Quantitative extraction and analysis of carriers of magnetization in sediments, *Geophysical J. Int.*, 124(1), 57-74.
- Hounslow, M. W., and A. C. Morton (2004), Evaluation of sediment provenance using magnetic mineral inclusions in clastic silicates: comparison with heavy mineral analysis, *Sed. Geol.*, 171(1-4), 13-36.
- IPCC (2007), Summary for Policymakers, in *Climate Change 2007: The Physical Science Basis. Contribution of Working Group I to the Fourth Assessment Report of the Intergovernmental Panel on Climate Change*, edited by S. Solomon, D. Qin, M. Manning, Z. Chen, M. Marquis, K. B. Averyt, M. Tignor and H. L. Miller, pp. 1-18, Cambridge University Press.
- Itambi, A. C., T. von Dobeneck, S. Mulitza, T. Bickert, and D. Heslop (2009), Millennial-scale northwest African droughts related to Heinrich events and Dansgaard-Oeschger cycles: Evidence in marine sediments from offshore Senegal, *Paleoceanography*, 24, PA1205.
- Jullien, E., et al. (2007), Low-latitude "dusty events" vs. high-latitude "icy Heinrich events", *Quat. Res.*, 68(3), 379-386.
- Kattan, Z., J. Y. Gac, and J. L. Probst (1987), Suspended sediment load and mechanical erosion in the Senegal Basin — Estimation of the surface runoff concentration and relative contributions of channel and slope erosion, *J. Hydrol.*, 92(1-2), 59-76.
- Kohfeld, K. E., and S. P. Harrison (2001), DIRTMAP: the geological record of dust, *Earth Sci. Rev.*, 54(1-3), 81-114.
- Koopmann, B. (1981), Sedimentation von Saharastaub im subtropischen Nordatlantik während der letzten 25.000 Jahre, *Meteor Forschungs-Ergebnisse*, 35, 23-59.
- Lesack, L. F. W., R. E. Hecky, and J. M. Melack (1984), Transport of Carbon, Nitrogen, Phosphorus, and Major Solutes in the Gambia River, West Africa, *Limnol. Oceanogr.*, 29(4), 816-830.
- Lézine, A. M., and H. Hooghiemstra (1990), Land-sea comparisons during the last glacial-interglacial transition: pollen records from West Tropical Africa, *Palaeogeogr. Palaeoclimat. Palaeoecol.*, 79(3-4), 313-331.
- Lyons, R., F. Oldfield, and E. Williams (2010), Mineral magnetic properties of surface soils and sands across four North African transects and links to climatic gradients, *Geochem. Geophys. Geosyst.*, 11, Q08023.
- Maher, B. A. (1986), Characterisation of soils by mineral magnetic measurements, *Phys. Earth Plane. Inter.*, 42(1-2), 76-92.
- Maher, B. A., and R. Thompson (1995), Paleorainfall Reconstructions from Pedogenic Magnetic Susceptibility Variations in the Chinese Loess and Paleosols, *Quat. Res.*, 44(3), 383-391.
- Maher, B. A., R. Thompson, and L. P. Zhou (1994), Spatial and temporal reconstructions of changes in the Asian palaeomonsoon: A new mineral magnetic approach, *Earth Planet. Sci. Lett.*, 125(1-4), 461-471.
- Maher, B. A., S. J. Watkins, G. Brunskill, J. Alexander, and C. R. Fielding (2009), Sediment provenance in a tropical fluvial and marine context by magnetic 'fingerprinting' of transportable sand fractions, *Sedimentology*, 56(3), 841-861.
- Mahowald, N. M., D. R. Muhs, S. Levis, P. J. Rasch, M. Yoshioka, C. S. Zender, and C. Luo (2006), Change in atmospheric mineral aerosols in response to climate: Last glacial period, preindustrial, modern, and doubled carbon dioxide climates, *J. Geophys. Res.*, 111(D10), D10202.
- Matthewson, A. P., G. B. Shimmield, D. Kroon, and A. E. Fallick (1995), A 300 kyr High-Resolution Aridity Record of the North African Continent, *Paleoceanography*, 10(3), 677-692.
- Mulitza, S., M. Prange, J. B. Stuut, M. Zabel, T. von Dobeneck, A. C. Itambi, J. Nizou, M. Schulz, and G. Wefer (2008), Sahel megadroughts triggered

- by glacial slowdowns of Atlantic meridional overturning, *Paleoceanography*, 23(4), PA4206.
- Nicholson, S. (2009), A revised picture of the structure of the “monsoon” and land ITCZ over West Africa, *Clim. Dyn.*, 32(7), 1155-1171.
- Niedermeyer, E. M., E. Schefuß, A. L. Sessions, S. Mülitz, G. Mollenhauer, M. Schulz, and G. Wefer (2010), Orbital- and millennial-scale changes in the hydrologic cycle and vegetation in the western African Sahel: insights from individual plant wax [δ D and [δ 13C], *Quat. Sci. Rev.*, 29(23-24), 2996-3005.
- Prospero, J. M., and T. N. Carlson (1972), Vertical and Areal Distribution of Saharan Dust over the Western Equatorial North Atlantic Ocean, *J. Geophys. Res.*, 77(27), 5255-5265.
- Prospero, J. M., P. Ginoux, O. Torres, S. E. Nicholson, and T. E. Gill (2002), Environmental characterization of global sources of atmospheric soil dust identified with the NIMBUS 7 Total Ozone Mapping Spectrometer (TOMS) absorbing aerosol product, *Rev. Geophys.*, 40(1), 1002.
- Pye, K. (1987), *Aeolian dust and dust deposits*, 334 pp., Academic press, London.
- Sarnthein, M., G. Tetzlaff, B. Koopmann, K. Wolter, and U. Pflaumann (1981), Glacial and interglacial wind regimes over the eastern subtropical Atlantic and North-West Africa, *Nature*, 293(5829), 193-196.
- Schefuß, E., S. Schouten, and R. R. Schneider (2005), Climatic controls on central African hydrology during the past 20,000 years, *Nature*, 437(7061), 1003-1006.
- Shine, K. P., and P. M. d. F. Forster (1999), The effect of human activity on radiative forcing of climate change: a review of recent developments, *Global Planet. Change*, 20(4), 205-225.
- Street-Perrott, F. A., and R. A. Perrott (1990), Abrupt climate fluctuations in the tropics: the influence of Atlantic Ocean circulation, *Nature*, 343(6259), 607-612.
- Stuut, J.-B., M. Zabel, V. Ratmeyer, P. Helmke, E. Schefuß, G. Lavik, and R. Schneider (2005), Provenance of present-day eolian dust collected off NW Africa, *J. Geophys. Res.*, 110, D04202.
- Weltje, G. (1997), End-member modeling of compositional data: Numerical-statistical algorithms for solving the explicit mixing problem, *Mathemat. Geol.*, 29(4), 503-549.
- White F (1983) A Descriptive Memoir to Accompany the UNESCO/AETFAT/UNSO Vegetation Map of Africa. In: United Nations Educational, Scientific, and Cultural Organization, Paris.
- Zarriess, M., and A. Mackensen (2010), The tropical rainbelt and productivity changes off northwest Africa: A 31,000-year high-resolution record, *Mar. Micropal.*, 76(3-4), 76-91.

Chapter 2

Unmixing signatures of aeolian, fluvial, bacterial and diagenetic magnetic mineral fractions in Late Quaternary marine sediments off Gambia, NW Africa

Janna Just^{1,2,3}, Mark J. Dekkers^{3,4}, Tilo von Dobeneck^{1,2,3}, Annelies van Hoesel⁵, Torsten Bickert^{1,2,3}

¹ Marine Geophysics, Depart. of Geosciences, Klagenfurter Strasse, University of Bremen,

² MARUM—Center for Marine Environmental Sciences, Leobener Strasse, University of Bremen, Germany

³ International Graduate College EUROPROX

⁴ Paleomagnetic Laboratory 'Fort Hoofddijk', Depart. of Earth Sciences, Budapestlaan 17, Utrecht University, The Netherlands.

⁵ Structural Geology and Tectonics, Depart. of Earth Sciences, Budapestlaan 4, Utrecht University, The Netherlands

To submit to Journal of Geophysical Research

We apply end-member (EM) modeling on 350 acquisition curves of the isothermal remanent magnetization (IRM) measured on samples of two marine gravity cores off NW Africa at the border of arid subtropical and humid tropical environments (GeoB 13602-1, 13°32.71'N; 17°50.96'W, 8.75 m long, spanning 75 ka; and GeoB 13601-4, 12°26.06'N, 18°00.29'W, 8.55 m long, spanning 60 ka). Our approach enables us to discriminate rock magnetic signatures of aeolian and fluvial material and to correct for the considerable imprint of magnetotactic bacteria and reductive diagenesis. The diagenetic EM occurs mainly below the sulfate-methane transition in which hydrogen sulfide is released. This EM was also found in a comparatively thin near-surface organic-rich layer. No less than up to 60% of the IRM signal is allocated to the biogenic EM which testifies the importance of this magnetotactic fraction. Surprisingly, the magnetosomes are preserved even below the modern iron redox boundary, which emphasizes that the identification and quantification of this fraction is crucial before interpreting the magnetic mineralogy in terms of terrigenous fluxes. Temporal variations of the aeolian and fluvial EMs appear to faithfully reproduce and support trends of dry conditions on the continent during Heinrich stadials and a humidification during the African Humid Period enable the quantification of dust input. We estimate that dust fluxes at the continental margin of NW Africa were at least 5 times higher during HS 1 than during the Last Glacial Maximum. Dust export from the Arabian-Asian dust corridor during Heinrich Stadials (HS) appears to be contemporaneous to phases of increased dust fluxes at the continental margin of NW Africa. This finding emphasizes that melt-water discharge in the North Atlantic had an impact on the atmospheric features in the northern hemisphere. Based on the occurrence of pedogenically formed magnetic minerals in fluvial and aeolian sediments, we infer that goethite was formed over hematite in more humid climate zones. Therefore, magnetic minerals prove to be a valid proxy to study (paleo-) environmental conditions in the source areas of terrigenous sediments.

2.1 Introduction

Over the past twenty years, rock magnetic methods have been increasingly used to distinguish sources of terrigenous sediment fractions in marine sediments. Bloemendal et al. (1988; 1992) were the first mapping the distribution of magnetic minerals in the eastern equatorial Atlantic Ocean and linking certain magnetic mineral fractions with their terrigenous source or diagenetic processes. Their studies suggest that Saharan dust contains a particularly high proportion of antiferromagnetic versus ferrimagnetic iron minerals even when expressed in terms of magnetic moments. A widely observed ultrafine magnetite fraction appeared to vary on glacial-interglacial timescales and was associated with either fluvial input or post-depositional bacterial biomineralization (Bloemendal et al. 1988; Bloemendal et al. 1992).

Schmidt et al (1999) presented a fuzzy c-means cluster analysis based on magnetic properties of 194 core-top samples collected from all parts of the South and Equatorial Atlantic. They distinguished ten rock magnetic provinces, each defined by a characteristic lithogenic or biogenic magnetic signature. Source areas are inferred to be nearby deserts, rivers, volcanoes or mid-ocean ridges. Terrigenous rock magnetic fingerprints of marine sediments can be identified and exploited by multi-proxy studies. For example, Larrasoana et al. (2003) and Köhler et al. (2008) combined rock magnetic and geochemical methods to analyze Neogene Mediterranean

sediments and interpreted elevated hematite and titanium contents as indices of enhanced north Saharan dust supply, and hence, of greater aridity. Recently, Itambi et al. (2009; 2010) investigated marine rock magnetic records off Senegal and Gambia to reconstruct southward shifts of the Intertropical Convergence Zone (ITCZ) concurrent with North Atlantic Heinrich events during the respective Heinrich stadials (HS; (Mulitza et al. 2008)), being responsible for arid conditions on the continent. In line with the earlier Bloemendal et al. (1988; 1992) studies, they noticed that the high-coercivity minerals hematite and goethite occurred mainly during more arid glacial and stadial periods and should consequently be of aeolian origin. Very fine grained and generally ubiquitous magnetite present throughout their records was interpreted as fluvial input associated with more humid periods (Itambi et al. 2010). The magnetic properties of Itambi et al. (2009) indicate that the expression of HS 1 is much stronger with respect to the remaining HSs, while HS 3 is less pronounced in their southernmost records. While there is clear and acknowledged evidence for iron oxide reduction in the lower parts of these cores (Itambi et al. 2009), it remains uncertain to what extent bacterial magnetite has contributed to the magnetic fine fraction of modern and past ocean margin sediments offshore NW Africa.

Bacterial magnetite is often considered a subordinate or negligible magnetic mineral phase

in oceanic regions with high terrigenous input. However, it has also been described as an abundant or even dominant magnetic mineral phase in the surficial sediments of upwelling regions off SW Africa (Schmidt et al. 1999; Hilgenfeldt 2000). Unjustified disregard of bacterial magnetite or its incorrect distinction from fluvial magnetite phases necessarily leads to erroneous conclusions concerning continental humidity and runoff.

Interpretation of the terrigenous fraction of NW African marine sediments is further complicated by the existence of various potential dust sources and wind systems. It has been claimed that NE trade winds export more local (coastal) Sahelian and Saharan dust to sea, while the African Easterly Jet (AEJ) releases dust from more distant Central Saharan sources which is further transported over the Atlantic within the Saharan Air Layer (e.g., Pye 1987; Chiapello et al. 1995). Not all studies, however, make this distinction, and little evidence for separate dust sources in rock magnetic or geochemical marine records has been shown so far. To be able to quantify continental climate changes and erosion, sediment fluxes and accumulation rates, detailed characterization of the various terrigenous, biogenic and diagenetic sources and processes is required.

In several other recent rock magnetic provenance studies (Hounslow and Morton 2004; Heslop and Dillon 2007; Maher et al. 2009; Roberts et al. 2011), isothermal remanent magnetization (IRM) acquisition curves serve as

input for mathematically unmixing sediments into their source components. They provide a concentration-dependent numerical representation of the full coercivity spectrum, and, accordingly, of the entire magnetic mineral population of given sedimentary mixtures. IRM acquisition curves obey the principles of linear mixing systems and are therefore suitable for end-member Member (EM) modeling techniques (Egli 2004a; Heslop and Dillon 2007).

In the studies of Itambi et al. (2009) and Bloemendal et al. (1988; 1992) it is well established that the magnetic mineralogy may be used to identify humid and arid phases in NW Africa. For budgeting aeolian and fluvial sediment input, however, we perform a quantitative characterization of the magnetic inventory of those fractions. For this purpose it is essential to evaluate the imprint of reductive diagenesis and the bio-mineralization of magnetic minerals in marine sediments.

We additionally use the magnetic inventory of pedogenically formed magnetic minerals within the fluvial and aeolian fractions to infer about the (paleo-) environmental conditions in their source areas (e.g., Kämpf and Schwertmann 1983).

The contribution of the aeolian and fluvial EMs imply the impact of North Atlantic Heinrich events on the low-latitude climate system and we further investigate the reasons for unequal expressions of HS 3 and HS 1 with respect to the remaining HSs which is also observed in the magnetic records of Itambi et al. (2009), but less

expressed in elemental ratios further to the north (Mulitza et al. 2008).

Two suitable sites on the continental rise at the western border of arid subtropical and humid tropical NW Africa have been selected (Fig. 2-1a): Site GeoB 13602 is located slightly north of the present Gambia River mouth while site GeoB 13601 is situated 100 km further south.

To distinguish the proportion of the various magnetic fractions we perform EM unmixing of IRM acquisition curves. Magnetic characteristics and the mineralogy of each obtained EM are subsequently analyzed by Cumulative Log-Gaussian (CLG) IRM component fitting (Kruiver et al. 2001) and are identified by com-

paring their magnetic mineralogy with data of known or plausible aeolian, fluvial, bacterial, and diagenetic magnetic mineral associations.

To further substantiate our interpretations using this statistical approach, we present high and low temperature magnetic data as well as scanning (SEM) and transmission electron microscope (TEM) images.

2.2 Geological and hydrographic setting

The continental margin off Gambia (NW Africa, Fig. 2-1a) is composed of an approximately 100 km wide and up to 400 m deep shelf and a continental slope descending at an angle of about 2.5° to water depths of 3000 m. From the north,

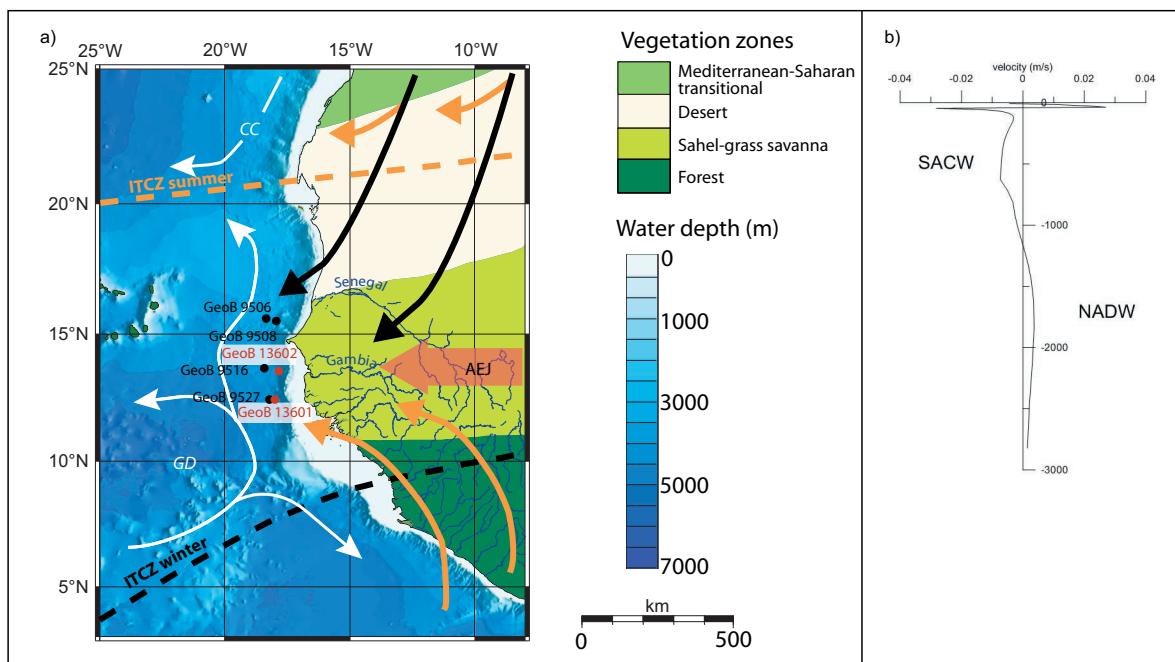


Fig. 2-1: (a) Vegetation belts in NW Africa modified after White (1983). Dust export to the NW continental margin from the Sahara occurs mainly during winter by the NE trade winds (black arrows) while the Inter-Tropical Convergence Zone (ITCZ) is located to the south. At high altitudes (~3000 m), dust is transported by the African Easterly Jet (AEJ). During summer, the SE Trades (orange arrows) and the associated monsoon system are responsible for rainfall in the Sahel. Surface water circulation in the south is controlled by the Equatorial Counter Current and associated anticyclonic circulation around the Guinea Dome (GD) and in the north by the Canary Current (CC). Both are indicated by white arrows. The gravity cores studied here are depicted in red. Gravity cores referred to in this study are indicated in black. (b) Vertical profile of meridional current velocities, SACW: South Atlantic Central Water, NADW: North Atlantic Deep Water.

the study area is under marginal influence of the westward turning Canary Current, which is fed by the easternmost branch of the Azores Current (Knoll et al. 2002). From the south, the seasonal cyclonic circulation around the Guinea Dome influences the study area, inducing a northward transport of surface water. The convergence of this gyre and the Canary current marks the boundary of North Atlantic Central Water and South Atlantic Central Water (Tomczak 2003). The northward-directed surface current of the South Atlantic Central Water entrains the upper 300-600 m of the water column in the study area. Underneath is the southward-directed North Atlantic Deep Water (NADW, 1000-4000 m; Tomczak 2003). The velocity profile of both meridional currents (Fig. 2-1b) reveals that the net transport of suspended material is to the north. Accordingly, satellite images (public data from Naval Research Laboratory, <http://www7320.nrlssc.navy.mil/GLBHycom1-12/equatl.html>) and modeled surface currents (Mittelstaedt 1991) indicate that the freshwater plume, and hence, also the sediment load of the Gambia River is primarily deflected towards the northern site. Aeolian material from the Sahara and Sahel is transported to both sites by NE winter monsoons at lower atmospheric altitude and by the higher AEJ (Pye 1987; Stuet et al. 2005; Mulitza et al. 2008).

2.3 Materials and chronology

The studied gravity cores GeoB 13602-1 (position: 13°32.71' N; 17°50.96' W, water depth:

2395 m, core length: 8.75 m) and GeoB 13601-4 (position: 12°26.06' N, 18°00.29' W, water depth: 2997 m, core length 8.55 m) were retrieved in 2009 during RV *Maria S. Merian* cruise MSM 11/2 on the continental slope (Fig. 2-1a). Both cores mainly consist of siliciclastic, dark olive clays and silts.

To estimate the amount of biogenic material, GeoB 13602-1 samples have been analyzed for biogenic opal (always <2.5%, data not shown), total carbon and total organic carbon using an Elementar Vario EL III. On this basis, the CaCO₃ weight percentages have been calculated. Carbonate content is generally lower than 25 wt % and organic carbon ranges between 2.5% in the uppermost parts of the core and 0.5 % during HS 1 (Fig. 2-2b).

GeoB 13602-1 was sampled at 5 cm intervals, from which specimens of the epibenthic species *Cibicides wuellerstorfi* were picked for stable isotope analyses that were performed with a Finnigan MAT 252 mass spectrometer. The age model was obtained by correlating the oxygen isotope records (Fig. 2-2a) to that of core MD 95-2042 (Shackleton et al. 2000). From six samples at depths of 0.02 m, 0.41 m, 1.01 m, 1.54 m, 2.21 m, 3.52 m, 4.50 m depth, planktonic

Depth in core (cm)	sample code	¹⁴ C age (¹⁴ C a BP)	calender age (a BP)	1σ calender age range (a BP)
2	Poz-35102	modern	modern	modern
41	Poz-41307	7990 ± 70	8454	8380-8521
101	Poz-41304	10890 ± 70	12404	12175-12595
154	Poz-41305	12200 ± 70	13619	13483-13729
221	Poz-35103	12790 ± 60	14403	14103-14567
352	Poz-41306	22800 ± 140	27084	27536-27189
480	Poz-41309	32400 ± 600	36511	35470-37203

Table 2-1: Radiocarbon data for GeoB 13602-1.

foraminifera tests of *G. ruber*, *G. saculifer*, *G. bulloides* and *G. inflata* were selected for radiocarbon analysis with a 1.5 SDH-Pelletron Model Compact Carbon AMS at the Poznań Radiocarbon Laboratory. Assuming a reservoir age of 400 years, raw ^{14}C ages were converted into calendar ages (Table 2-1) using the calibration curve of Reimer et al. (2009). Inclusion of

^{14}C ages from depths of 1.01 and 2.21 m taken within the Younger Dryas and HS 1 intervals, would lead to a misfit with the oxygen isotope records. Since the meltwater discharge during these periods led to changes in NADW production (e.g. Stocker and Wright 1991; Broecker 1998) and thus a possible ingression of southern ocean waters with a different reservoir age, we excluded these ^{14}C ages. The age model of core GeoB 13602-1 was then transferred to core GeoB 13601-4 by correlating their diffuse reflectance spectrophotometry records (data not shown) and rock magnetic parameters. GeoB 13602-1 spans the past 75 ka with a mean sedimentation rate of 11.5 cm/kyr while GeoB 13601-4 spans the past 60 ka with a mean sedimentation rate of 14 cm/kyr. On the basis of the carbonate weight percentages the sedimentation rate of GeoB 13602-1 was split into the biogenic and terrigenous fractions (Fig. 2-2c) assuming the same dry bulk density for both fractions.

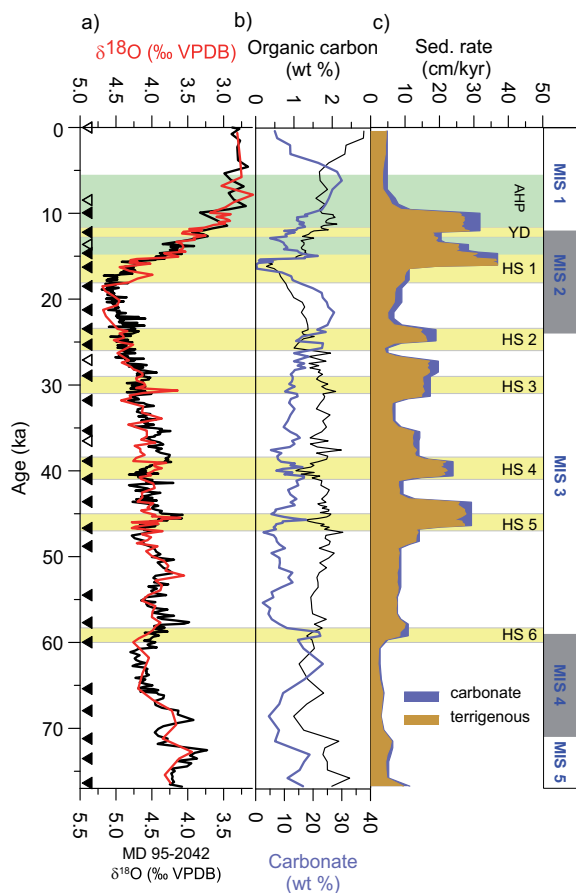


Fig. 2-2: (a) Oxygen isotope records for cores MD 95-2042 (black) (Shackleton et al. 2000) and GeoB 13602-1 (red). Filled triangles indicate the ages derived by correlating the benthic $\delta^{18}\text{O}$ record and open triangles mark radiocarbon ages. (b) Weight % of total organic carbon and CaCO_3 of GeoB 13602-1. (c) Sedimentation rate split into biogenic and terrigenous fraction (based on carbonate weight % and assumed equal dry bulk density of both fractions). The low sedimentation rates in the lower part are most probably due sediment compaction during gravity coring. MIS: Marine Isotope Stage, AHP: African Humid Period (light green), YD: Younger Dryas, HS: Heinrich Stadial (after Sarnthein et al., 2001), LGM: Last Glacial Maximum.

2.4 Methods

2.4.1 Rock Magnetism

Room temperature magnetic measurements

For both cores, rock magnetic properties were measured on 6.2 cm^3 samples taken at 5 cm spacing (~ 400 samples). Low-field magnetic susceptibility (χ), was determined using a Kappabridge KLY-2 (measurement frequency 920Hz) device. Frequency dependence of susceptibility (χ_{fd}), which serves as a measure of the

presence of ultra-fine superparamagnetic (SP (Dearing et al. 1996)) magnetite was measured for GeoB 13602-1 (Bartington susceptibility system MS2B). Measurements of laboratory-induced remanence parameters were performed using an automated 2 G Enterprise 755 R DC superconducting magnetometer. IRM acquisition curves, which have different coercivity distributions for different magnetic minerals (e.g., Eyre 1996; Frank and Nowaczyk 2008) were obtained using the in-line pulse magnetizer and an “external” pulse magnetizer (2G Enterprise). For a more detailed description of the experimental setup, see auxiliary material. We use the magnetic remanence acquired at the 100 mT step ($IRM_{(100\text{ mT})}$) to estimate the multidomain (MD) magnetite content (Frederichs et al. 1999). Anhysteretic remanent magnetization ($ARM_{(100\text{ mT})}$) indicates the presence of fine grained single domain (SD, King et al. 1982; Frederichs et al. 1999). The $ARM_{100\text{ mT}}/IRM_{100\text{ mT}}$ can thus be used as a magnetic grain-size indicator. The S-Ratio

$$S = 0.5[(-IRM_{-300\text{ mT}} / SIRM) + 1]$$

(Bloemendal et al. 1992), represents the ratio of low to high-coercivity magnetic minerals. The hard IRM (HIRM) (Stoner et al. 1996),

$$HIRM = 0.5(SIRM + IRM_{-300\text{ mT}})$$

quantifies the high-coercivity magnetic minerals (Frederichs et al. 1999; Kruijer and Passier 2001; Heslop 2009).

Low- and high-temperature magnetic measurements

High- and low-temperature magnetic measurements have been performed on selected dry bulk samples. Low-temperature cycling experiments between 5 and 300 K (2 K steps) were conducted with the Quantum Design XL7 Magnetic Properties Measurement System (MPMS) at Bremen University (Germany). We measured warming curves after zero-field cooling (ZFC) and after in-field cooling (FC). SIRM warming experiments were performed in a temperature interval of 240-400 K. High-temperature measurements of magnetization vs. temperature were made in air between 25 and 700°C on a modified horizontal translation Curie balance (Mullender et al. 1993, cycling field 20-400 mT). Heating and cooling rates were 10° C/min.

2.4.2 Scanning and transmission electron microscopy

Scanning electron microscopy (SEM) and transmission electron microscopy (TEM) observations were performed on magnetic separates and magnetic extracts.

For SEM observations, the specimens were gold-covered and analyzed on a SUPRA TM 40 high-resolution Field Emission SEM instrument at the Institute of Historical Geology – Paleontology at Bremen University. For imaging, the secondary electron (SE) beam was used at energy levels between 5 and 15 keV. To obtain the elemental composition of the particles, energy dispersive spectroscopy (EDS) with an energy

level of 15 keV was performed.

A FEI Tecnai 20 FEG TEM at the Electron Microscope Centre at Utrecht University was operated in bright field mode with an acceleration voltage of 200 keV. Diffraction patterns have also been analyzed. All shown EDS spectra are normalized to oxygen maxima.

2.4.3 Numerical unmixing

In a mathematical sense, remanence-based sedimentary magnetic records constitute linear combinations of the respective magnetic properties of all contributing source or mineral fractions. EM analysis is an inverse technique aimed at numerically unmixing such components. It assumes that a composite record consists of a small, discrete and *a priori* unknown number of geologically independent and magnetically distinguishable components, whose properties remain constant over time. EM analysis yields a minimal set of EM curves, whose properties best explain the full internal variability of a data set. Basis functions are not needed and the only criterion for the input curves is monotony. To further characterize the magnetic properties of calculated EMs, IRM component analysis (Kruiver et al. 2001) has been applied. This is, in contrast, a forward technique and requires a system of hypothetical basis functions. Multiple cumulative log Gaussian (CLG) basis functions are used to fit the bulk signal (cf. Robertson and France 1994). Because of the different nature of these techniques (inverse and forward), they can be run in conjunction as mutual verification.

End-member analysis

All IRM acquisition curves were unmixed using the IRM Unmixer code by *Heslop and Dillon* (2007), which adopts the algorithm developed by *Weltje* (1997). In the fundamental equation of EM analysis,

$$X=AS + \varepsilon ,$$

X represents a $n*m$ matrix of n observations (= individual samples) in rows and m variables (= IRM steps) in columns. A denotes the abundance of a set of k EMs in columns for the n samples in rows, S represents the m properties of the k EMs, and ε is the error matrix. Because the contributions of each EM must be positive, a non-negativity constraint ($A_{ij} \geq 0$) is included in the algorithm (Heslop and Dillon 2007; Heslop et al. 2007). Error sources are instrumental noise and temporal variations of individual source signatures. The decision on how many EMs to include is a compromise between keeping the number of components as low as possible while having a reasonable correlation of modeled and input data. IRM Unmixer provides decision criteria by performing principal component analysis (PCA) with increasing numbers of components and returning their coefficients of determination (r^2). EMs should be geologically interpretable within their environmental settings (Prins 1999; Weltje and Prins 2007).

Note that the contribution of each EM (A) refers to the SIRM of each sample and cannot directly

be translated to volume or mass percentages. A volume calibration of the EMs would require detailed information about a) the concentration of magnetic minerals in the bulk EMs and b) the geochemistry and crystal structure of the respective minerals.

IRM component analysis

To assess the magnetic mineralogy of the EMs, IRM component analysis has been applied on the IRM acquisition curves that emerge from the EM modeling. IRM acquisition curves of a

mixed magnetic mineralogy can be described as a combination of different CLGs (Robertson and France 1994) $s = Cb + \varepsilon$, where s represents the IRM acquisition curve of each EM, C denotes the IRM acquisition curves of the components and b the proportion of each component to SIRM. CLG components are characterized by their magnitude (corresponding to SIRM contribution), median field $B_{1/2}$ (at which half of the SIRM of the component is acquired) and dispersion parameter DP (reflecting the width of the coercivity distribution which in log space is

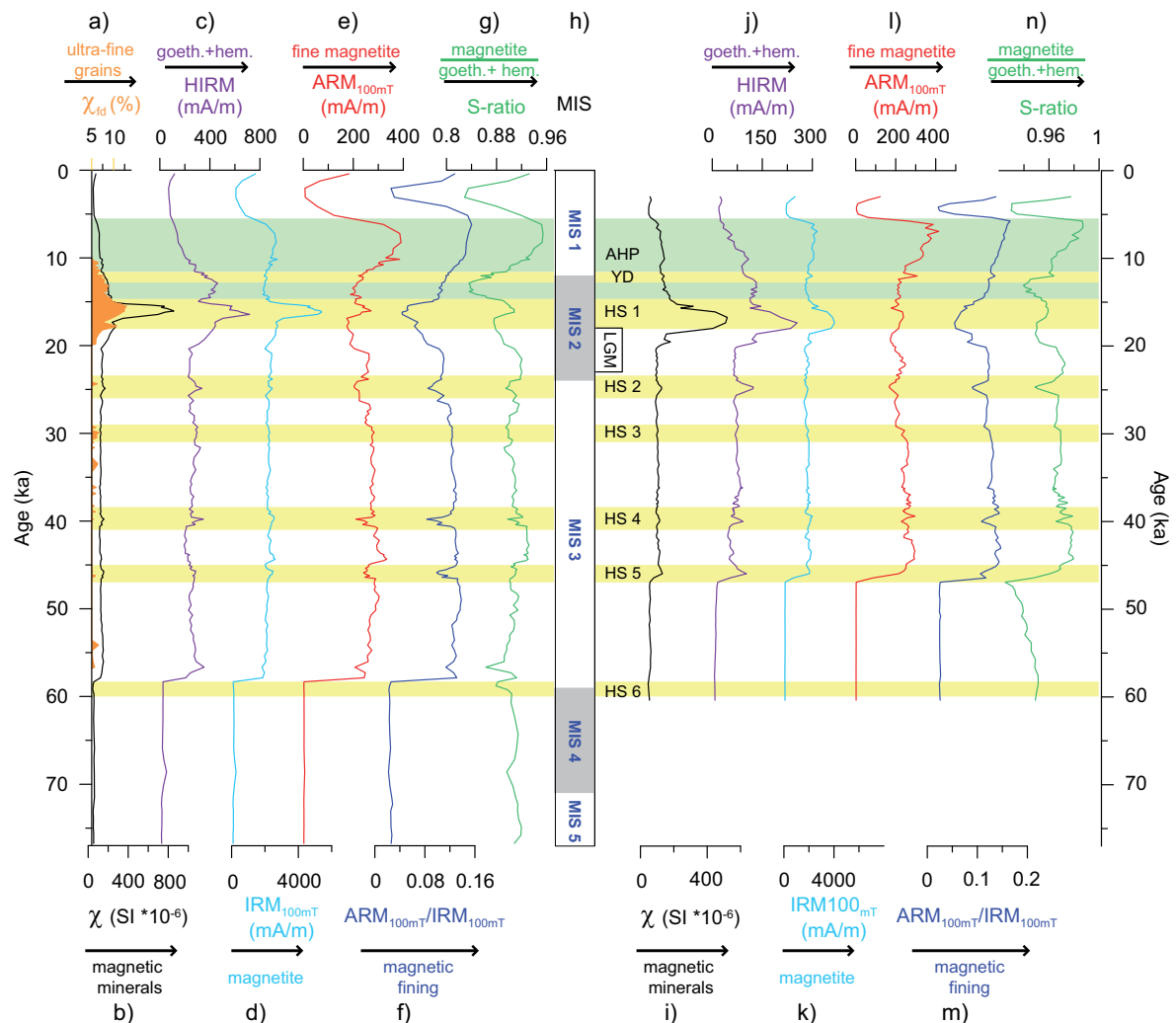


Fig. 2-3: Rock magnetic record for GeoB 13602-1 (a-g) and GeoB 13601-4 (i-n). Marine Isotope Stages (MIS) are depicted in (h). AHP: African Humid Period (light green), YD: Younger Dryas, HS: Heinrich Stadials (after Samthein et al., 2001), LGM: Last Glacial Maximum.

equivalent to one standard deviation). The approach used here has been developed by Kruiver et al. (2001). For further details, see Kruiver et al. (2001) and Heslop et al. (2004). The IRM acquisition curves can depart from log Gaussian functions due to thermal effects, magnetic interaction (Egli 2003) as well as the starting state of the magnetic system (Petrovský et al. 1993; Heslop et al. 2004), which should be taken into account when performing the curve fitting. Estimates of components relate to their magnetic moment, which cannot be converted directly into magnetic mineral concentrations, e.g., the SIRM of magnetite is 1-20 Am²kg⁻¹ (grain-size dependent) and is thus ~200 times higher than for hematite (0.08-0.2 Am²kg⁻¹) and goethite (0.02-0.1 Am²kg⁻¹) (Peters and Dekkers 2003)

2.5 Results

2.5.1 Room temperature magnetic measurements

Core GeoB 13602-1

The lowermost interval of GeoB 13602-1 from 76 to 57 ka (8.75-7.80 m depth) is marked by quasi-absence of magnetic minerals in the fine SD (Fig. 2-3e) and coarser MD (Fig. 2-3d) fractions. Since the loss of ARM is strongest, the residual phase coarsens (Fig. 2-3f). A similar pattern is found in the shallow interval of 4.1-1.2 ka (0.35-0.20 m depth). These conspicuous differences and the sharp boundaries with the remaining part of the records indicate that pervasive reductive diagenesis of the primary iron oxides has affected both intervals (e.g., Karlin

and Levi 1983; Garming et al. 2005; Rowan et al. 2009). The apparently well-preserved remainder of the record from 57 to 21.4 ka has relatively stable values except for shorter intervals that correspond to HSs. A coarsening of the magnetic grain size (Fig. 2-3f), and an absolute increase of high-coercivity magnetic minerals (i.e., hematite and/or goethite, Fig. 2-3c) with related S-ratio minima is observed in the intervals of HS 5, HS 4 and HS 2. Prominent peaks χ , χ_{fd} , HIRM, IRM_{100 mT} and troughs of ARM_{100 mT}/IRM_{100 mT} exist during HS 1. A minimum and successive maximum of the S-ratio (Fig. 2-3g) after 16.4 ka implies changes in the balance of high- to low-coercivity magnetic minerals and additionally an increase of fine grained magnetite (Fig. 2-3e). Around 12.5 ka, during the Younger Dryas (YD), less pronounced maxima and minima exist. In the following, the concentration of magnetite increases, accompanied by a fining magnetic grain size (Fig. 2-3f).

Core GeoB 13601-4

The magnetic record of core GeoB 13601-4 largely matches that of GeoB 13602-1. An equally radical loss in magnetic minerals is present in the lowermost interval from 60 to 45 ka (8.55-7.50 m). Furthermore, the interval from 6 to 3 ka (0.40-0.20 m depth) is partly depleted in magnetic minerals. The intermediate interval from 45 ka to 18.3 ka shows relatively small (10-20%) variations in all magnetic signals. Local deviations during HS 4 and HS 2 imply a relative increase of coarser magnetite grains (Fig.

2-3m), as well as of high-coercivity magnetic minerals (Fig. 2-3j). During HS 1 a peak in χ , HIRM and $IRM_{100\text{ mT}}$ is present, whereas the S-ratio and $ARM_{100\text{ mT}}/IRM_{100\text{ mT}}$ have minima. Another local minimum during the Younger Dryas (12.5 ka) is only present in the S-ratio.

Comparison of cores GeoB 13602-1 and GeoB 13601-4

The magnetic parameters of the northern core GeoB 13602-1 are approximately 20% (χ), 35% (HIRM), 20% ($IRM_{100\text{ mT}}$), and 10% ($ARM_{100\text{ mT}}$) higher with respect to those of the southern core GeoB 13601-4. In particular the fraction of high-coercivity minerals is more pronounced at the northern site. All HS peaks in the northern core are also more pronounced. While other peaks in both cores largely correspond, the maximum at HS 5 in GeoB 13602-1 has no counterpart in the southern core. Note however, that in GeoB 13601-4, HS 5 is located just above the diagenetic zone. The most prominent peak in both records corresponds to HS 1. Peaks in magnetic parameters that coincide with North Atlantic Heinrich Events have been previously reported from the nearby (cf. Fig. 2-1a) gravity cores GeoB 9516-5 and GeoB 9527-5 (Itambi et al. 2009) and were interpreted as periods of massive dust export and thus arid continental conditions in NW Africa. According to this interpretation, our record indicates that aeolian sediments contain a higher amount of coarse grained magnetite, high-coercivity minerals as goethite and hematite, and a higher content of

ultra-fine SP minerals. The latter correspond most likely as pedogenically formed coatings on silicate grains (Sarnthein et al. 1981; Itambi et al. 2009).

2.5.2 End-member analysis

The EM analyses of the individual cores and the pooled data set are compiled in Fig. 2-4. For the southern core GeoB 13601-4, three EMs suffice to reach a high coefficient of determination ($r^2=0.97$, Fig. 2-4a). To unmix the northern GeoB 13602-1 record, four EMs have been selected ($r^2=0.97$, Fig. 2-4a), although three EMs also yield a very reasonable r^2 of 0.96 at the break in slope of the r^2 plot. However, as will be shown later, large similarities between three of the four EMs for GeoB 13602-1 and the three EMs for GeoB 13601-4 justifies consideration of four EMs in the former. For the merged data set, four EMs were used to fit the data ($r^2=0.97$).

End-member characteristics

The EMs derived from the individual and the merged data sets (Fig. 2-4h, i) are similar in terms of coercivity distribution and are therefore labeled correspondingly. We label the calculated EMs as A, F, B and D already anticipating their interpretation in terms of aeolian, fluvial, biogenic and diagenetic origins, respectively. The contributions of modeled EMs to the SIRM are shown in Fig. 2-4d-g, while the outer panels (b, c, h, i) are plots of their respective IRM acquisition curves. Note that Fig. 2-4h and i contain the EMs derived from the merged data set as well

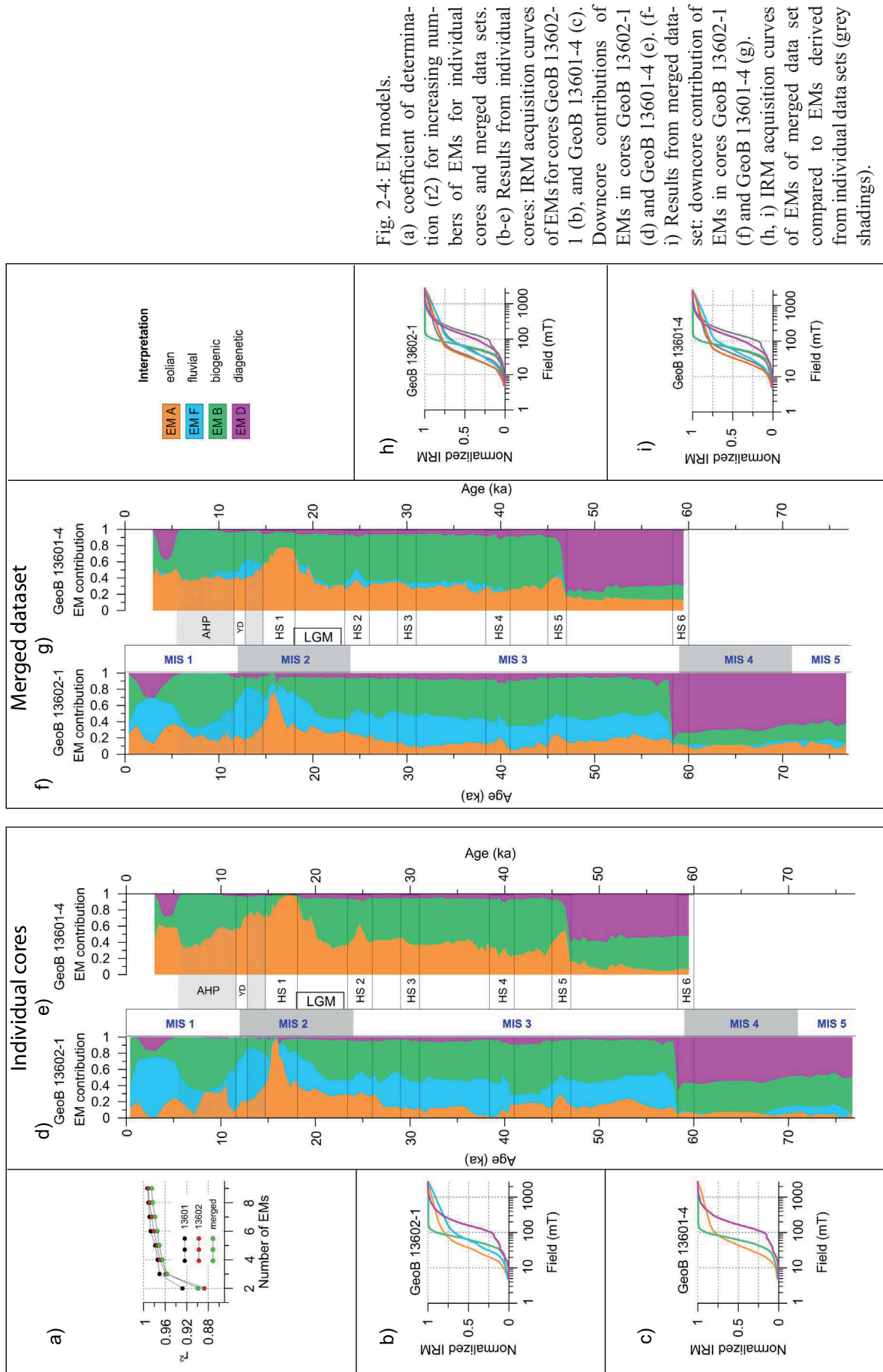


Fig. 2-4: EM models. (a) coefficient of determination (r^2) for increasing numbers of EMs for individual cores and merged data sets. (b-e) Results from individual cores: IRM acquisition curves of EMs for cores GeoB 13602-1 (b), and GeoB 13601-4 (c). Downcore contributions of EMs in cores GeoB 13602-1 (d) and GeoB 13601-4 (e). (f-i) Results from merged data set: downcore contribution of EMs in cores GeoB 13602-1 (f) and GeoB 13601-4 (g). (h, i) IRM acquisition curves of EMs of merged data set compared to EMs derived from individual data sets (grey shadings).

as those from the individual cores (cf. Fig. 2-4b, c) which are depicted in grey for evaluation of differences.

GeoB 13602-1

The magnetically depleted lowermost interval of core GeoB 13602-1 (cf. Fig. 2-3) is marked by a high contribution of EM D and EM B to SIRM (Fig. 2-4d). Above, the influence of EM D diminishes to low levels except for a near-surface layer at 4.6-1.7 ka. However, SIRM is substantially reduced within this zone (cf. Fig. 2-3d). When expressed in absolute amounts, EM D appears to remain approximately constant throughout the core, while the contribution of EM B rises above the diagenetically affected interval. In the interval 58-26 ka, EMs A, F and B are present with relatively stable contributions to SIRM of 15-25%, 20-30% and 40-50%, respectively. EM A has minor peaks at 53.5 and 46.2 ka (the latter is HS 5). During HS 2 and the LGM, the relative proportion of EM A increases at the cost of all other EMs and reaches a dominant peak during HS 1. Above this peak, its impact decreases in favor of EM F, whose proportion peaks from 14.2-12.5 ka (first part of the African Humid Period). At 8.5 ka the contribution of EM B peaks, accounting for 60% of SIRM.

GeoB 13601-4

The magnetically depleted zone in core GeoB 13601-4 below 46 ka and the narrow diagenetic layer near the core top (cf. Fig. 2-3) are equally indicated by greater contributions of EM D (Fig.

2-4e) and EM B. From 46 to 21.2 ka, the relative variations of the EMs A and B are low, however, an increasing trend of EM A is observed. Local peaks of EM A occur during HS 5 and HS 2. During HS 1, EM A reaches a contribution of nearly 100% and remains dominant until about 13 ka. Above, the proportion of EM A decreases in favor of EM B, whose maximum influence appears at 6.8 ka. The influence of EM A then rises.

Merged data set

The contributions of the EMs obtained by unmixing the merged dataset from GeoB 13602-1 and 13601-4 are similar to the EM models for the separate cores (compare Fig. 2-4d and e with 2-4f and g). In the lower interval of the cores, the contribution of EM B is suppressed with respect to EM D when compared to the individual cores. Above the diagenetically affected zones, all trends and local peaks are depicted. However, the merged model has smoother expressions than in the individual GeoB 13601-4 model because of the extra EM in the merged data set. An exception is a peak in EM A during HS 4, which was not expressed in the individual EM models. According to our starting hypothesis, that fluvial sediments are only to be expected at the northern site, the marginal contribution of EM F in GeoB 13601-4 supports such a scenario. This outcome of the EM analysis illustrates that our approach is well suited to unmix the terrigenous fraction.

2.5.3 IRM component analysis

Here, we aim to further elucidate the nature of all EMs through more quantitative analysis of the magnetic mineralogy. The EM model of the merged data set largely matches and supports the findings of the two core-specific EM analyses, therefore we focus on the pooled EM model.

IRM components for the separate EMs are listed in Table 2-2, while we visualize the fit for the EMs of the merged dataset only (Fig. 2-5). The shape of the IRM acquisition curve indicates that EMA is a mixture of low-coercivity and high-coercivity magnetic minerals (magnetite, hematite and/or goethite, respectively). Four components (1-4) with increasing magnetic hardness (Fig. 2-5a) are present. Two magnetically soft components ($B_{1/2} \sim 18$ mT; $B_{1/2} \sim 30$ mT,) account for 11% and 68% of the total SIRM, respectively.

The soft-magnetic component 2 corresponds to magnetite. IRM coercivity spectra of PSD and MD magnetite often depart from a lognormal distributions, i.e. have left-skewed distributions (Egli 2003) due to thermal activation effects (Egli and Lowrie 2002). The left-skew cannot be fitted with the Kruiver et al. (2001) approach and a second associated component is required to properly fit components to the data to account for the skewness. We suggest that component 1 is attributed to this skewness and does not represent an additional magnetic phase. Component 3 ($B_{1/2} \sim 260$ mT) accounts for 11.5% of SIRM and is interpreted as hematite, while component 4 ($B_{1/2} \sim 1660$ mT) contributes only 8% to the total SIRM and is interpreted as goethite.

The IRM acquisition curve for EM F (cf. Fig. 2-5b) is relatively similar to that of EM A. How-

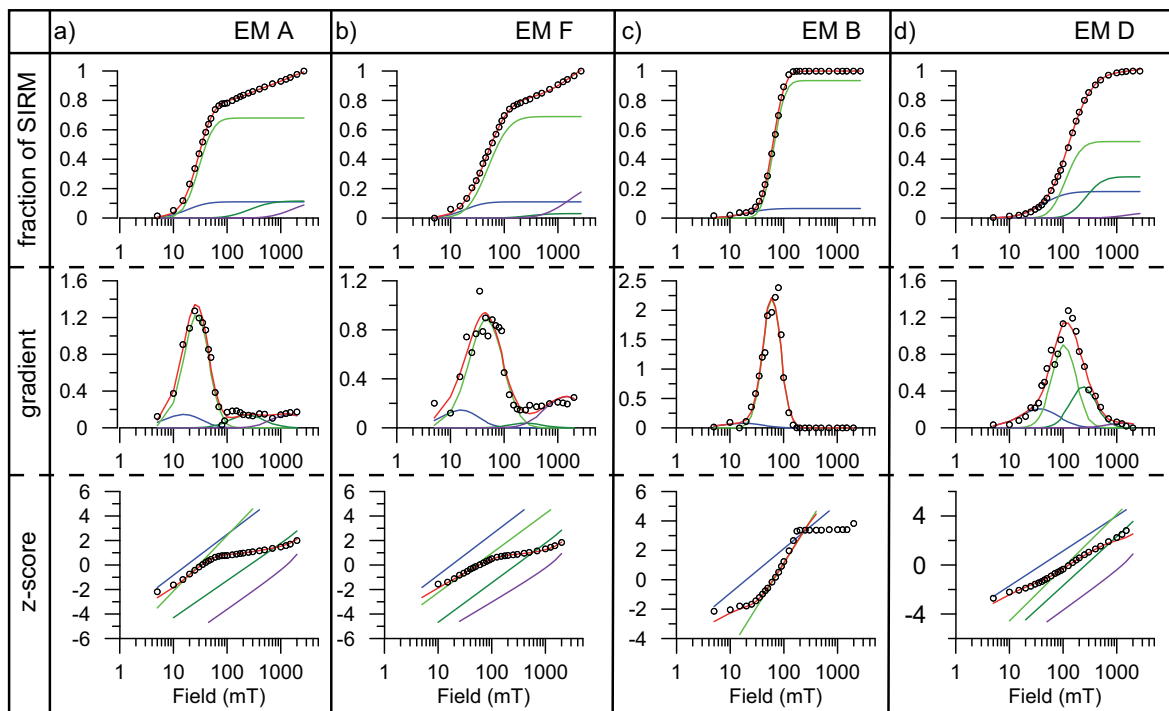


Fig. 2-5: IRM component analyses of EMs (merged dataset). Each column corresponds to one EM. Different colors indicate the components needed to fit (red curve) the IRM acquisition curve (black dots). Upper panels: linear acquisition plot; middle panels: gradient acquisition plot; lower panels: standardized acquisition plot.

ever, acquisition starts at slightly higher fields (20 mT) and its initial slope is less steep and rises linearly (on a logarithmic scale) at higher fields with a somewhat steeper gradient. The proportion of magnetically soft (magnetite) phases relative to the hard antiferromagnetic (hematite/goethite) phases is therefore lower for EM F. Two soft components ($B_{1/2} \sim 18$ mT, $B_{1/2} \sim 50$ mT) that carry 11% and 69% of the total SIRM for EM F, are identified as magnetite with a left-skewed coercivity spectrum (Fig. 2-5b). Compared to EM A ($B_{1/2} \sim 30$ mT), this magnetite is harder and accordingly represents finer grain sizes, which corresponds largely to the observed physical grain sizes of fluvial (Gac and Kane 1986) and aeolian (Stuut et al. 2005) material from dust- or fluvial-dominated periods off the NW African coast (Mulitza et al. 2008). Two high-coercivity components ($B_{1/2} \sim 280$ mT, $B_{1/2} \sim 1660$ mT) contribute to 3% and 25% of the total SIRM and are attributed to hematite and goethite, respectively. The difference between aeolian and fluvial EMs with regard to

hematite (aeolian) and goethite (fluvial) balance is striking.

EM B (Fig. 2-5c) acquires remanence over a narrow field interval and reaches complete saturation at 120 mT. For a CLG fitting of this EM, two components are needed. Component 1 ($B_{1/2} \sim 20$ mT) carries only 6.5% of the SIRM, while Component 2 ($B_{1/2} \sim 65$ mT) contributes the remaining 93.5%. This fraction is interpreted as bacterial magnetite, which owes its relatively high coercivity to the chain-like arrangement of the fossil SD sized magnetosomes (e.g. Petersen et al. 1986; von Dobeneck et al. 1987; Vali et al. 1989). Similarly, ‘biogenic soft’ and a ‘biogenic hard’ components have been identified by *Egli* (2004a).

Remanence acquisition in EM D takes place mainly at intermediate fields from 0.1 to 1 T, where hard ferri- and soft antiferromagnetic minerals acquire an IRM. Component 1 ($B_{1/2} \sim 40$ mT) carries 18%, component 2 ($B_{1/2} \sim 112$ mT) 52%, component 3 ($B_{1/2} \sim 260$ mT) 28%, and component 4 ($B_{1/2} \sim 1580$ mT) ac-

		Component 1			Component 2			Component 3			Component 4		
		SIRM	B1/2	DP	SIRM	B1/2	DP	SIRM	B1/2	DP	SIRM	B1/2	DP
GeoB13602-1	EM A	0.8	28.84	0.29	0.15	199.53	0.42	0.08	1621.81	0.35			
	EM F	0.2	20.42	0.29	0.50	51.29	0.23	0.15	199.53	0.30	0.20	1584.89	0.35
	EM B	0.09	14.13	0.3	0.91	64.57	0.17						
	EM D	0.23	39.81	0.38	0.46	154.88	0.13	0.31	323.59	0.25	0.01	1584.89	0.35
GeoB13601-4	EM A	0.05	15.85	0.35	0.74	36.31	0.26	0.12	158.49	0.33	0.14	1584.89	0.33
	EM F												
	EM B	0.11	16.22	0.29	0.89	64.57	0.17						
	EM D	0.18	39.81	0.38	0.48	147.91	0.12	0.34	331.13	0.24			
merged dataset	EM A	0.21	17.78	0.3	0.56	30.20	0.2	0.13	199.53	0.31	0.13	1584.89	0.31
	EM F	0.2	17.78	0.3	0.56	51.29	0.25	0.07	199.53	0.28	0.20	1258.93	0.35
	EM B	0.065	19.95	0.33	0.94	64.57	0.17						
	EM D	0.18	39.81	0.35	0.52	112.20	0.23	0.28	263.03	0.25	0.00	1584.89	0.32

Table 2-2: IRM component analyses of EMs derived by unmixing each core and the merged dataset.

counts for a mere 4% of the total SIRM. Component 4 probably represents goethite whose significance is not high when expressed on a magnetic basis. However, due to its low SIRM, up to 200-500 times lower than that of magnetite, the quantity of goethite expressed on a molar or mineralogic basis must be high. The relatively hard component 2 most likely represents relict Ti-rich ferrous hemoilmenite or titanomagnetite phases that survived reductive diagenesis (Bloemendal et al. 1993; Emiroglu et al. 2004; Nowaczyk 2011). Component 1 may either represent a left skew of component 2, as argued above, or it may consist of alteration-resistant small magnetic inclusions in a silicate matrix (Hounslow and Maher 1996; Hounslow and Morton 2004; Maher et al. 2009). The latter interpretation is

consistent with the rock magnetic record, where EM D is only prominent in the magnetically depleted lower parts of both cores.

2.5.4 Additional rock magnetic analyses

To supplement and further support the EM model analysis and IRM component interpretation, we performed high- and low-temperature rock magnetic measurements for three samples from GeoB 13602-1 with dominant biogenic (8.2 ka), fluvial (13.6 ka) and aeolian (15.5 ka) EM contributions, respectively.

Low- and high-temperature magnetic properties

The ZFC and FC warming curves of the EM A and EM F samples converge with increasing temperature, in particular in the interval 20-100 K

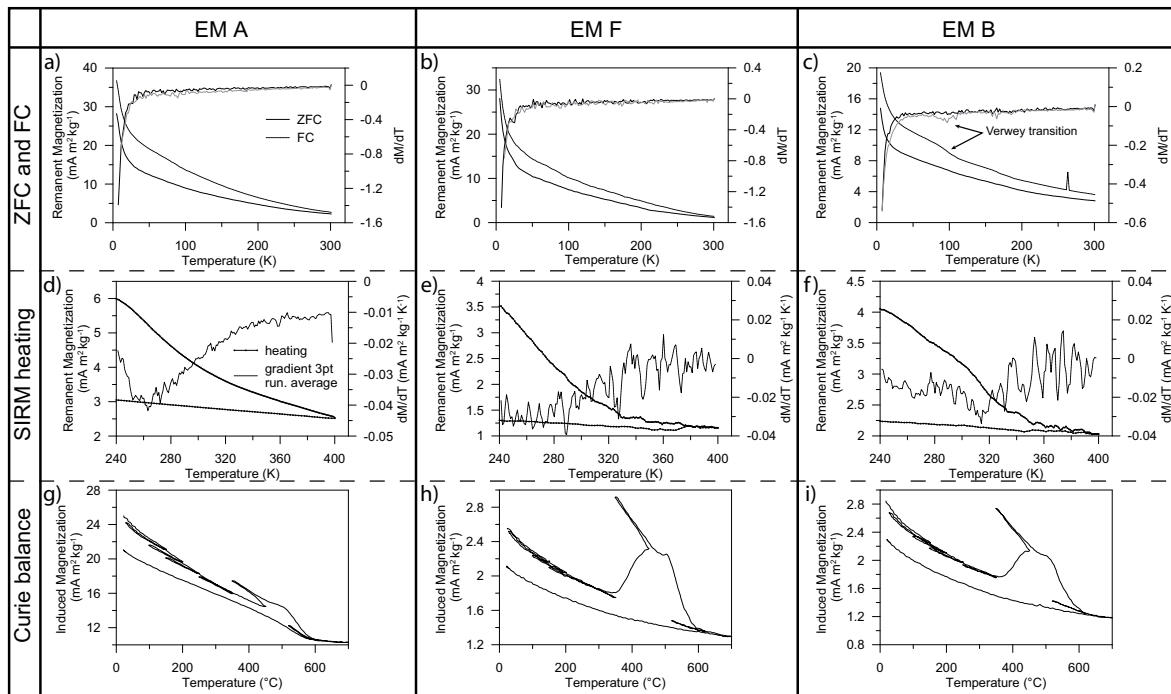


Fig. 2-6: Low- and high-temperature measurements of samples from intervals with strong contributions of EM A (a, d, g), EM F (b, e, h), and EM B (c, f, i). The notable convergence of ZFC and FC warming curves (a-c) and the marked loss of magnetization while heating to ~350 K (d-f) points to the presence of goethite. The Verwey transition is evident in the data from EM B sample (c). Curie balance measurements (g-i) indicate the thermal alteration of pyrite to magnetite. The pyrite content appears to be lowest in the EM A sample (g).

(Fig. 2-6a, b). This effect is less pronounced in the EM B sample (Fig. 2-6c). The acquisition of remanence during FC and convergence of FC and ZFC curves was previously observed for goethite samples (Liu et al. 2006) and has also been attributed to the presence of goethite in pelagic (Franke et al. 2007) sediments. Smirnov and Tarduno (2000) recognized a similar convergence in samples from the equatorial Pacific Ocean but did not find any evidence for the presence of goethite. Our SIRM heating experiments indicate a dramatic loss in magnetization while heating up to ~ 330 K (Fig. 2-6d-f). Notably, this temperature is lower than blocking temperatures for pure goethite, however, due to isomorphous Al-substitution which is typical for pedogenically formed goethites (Fitzpatrick and Schwertmann 1982) and excess water in the structure, the blocking temperature lowers (Lowrie and Heller 1982; Dekkers 1989; Liu et al. 2006). We thus attribute both the convergence of ZFC and FC curves and the SIRM loss to the presence of goethite which is also detected by the IRM component analyses. In contrast with the two other samples, the FC curve of the EM B sample (Fig. 2-6c) has a Verwey transition that is indicative of stoichiometric SD magnetite as produced by magnetotactic bacteria (Moskowitz et al. 1993). The absence of this transition in the EM F and EM A samples hints at oxidation (e.g., Özdemir et al. 1993) or Ti-substituted magnetites (e.g., Kakol et al. 1992). The Curie balance cycles (Fig. 2-6g-i) indicate a strong increase in induced magnetization during heat-

ing within a temperature interval of 350-450°C which has been attributed to oxidation of framboidal pyrite (Passier et al. 2001). This effect and thus the concentration of pyrite are lowest in the EM A sample.

Electron Microscopy

In the heavy liquid separates, magnetic particles appear to be sparse in comparison with the high amounts of paramagnetic Ti oxides. On the other hand, pyrite is found frequently in all heavy liquid extracts. Framboidal pyrite is abundant in microenvironments like foraminifera tests (Fig. 2-7a, e.g., Roberts and Turner 1993; Rowan et al. 2009). In the magnetic extracts, the size of Fe-Ti oxides can reach diameters of up to 40 μm (Fig. 2-7c, d). The physical grain-size mode of present-day dust collected offshore Africa is mostly 8-42 μm but can reach grain sizes of 200 μm (Stuut et al. 2005). Therefore, these coarse grained Fe-Ti oxides are most likely transported by wind. Most of those grains have sub-regular morphologies, which might be attributed to mechanical abrasion and/or fragmentation during transport (Fig. 2-7b, d, e). However, some idiomorphic grains can be found (Fig. 2-7f). The EDS analyses reveal varying Fe:Ti ratios between 1:2 and 3:1. Nearly pure magnetite grains also occur. In Fig. 2-7d, Ti-Fe oxides have shrinkage cracks, which indicate low-temperature oxidation (Petersen and Vali 1987). Ilmenite exsolution lamellae, which are typical for Ti-rich titanomagnetite, are preserved as skeletons in some grains while the more unsta-

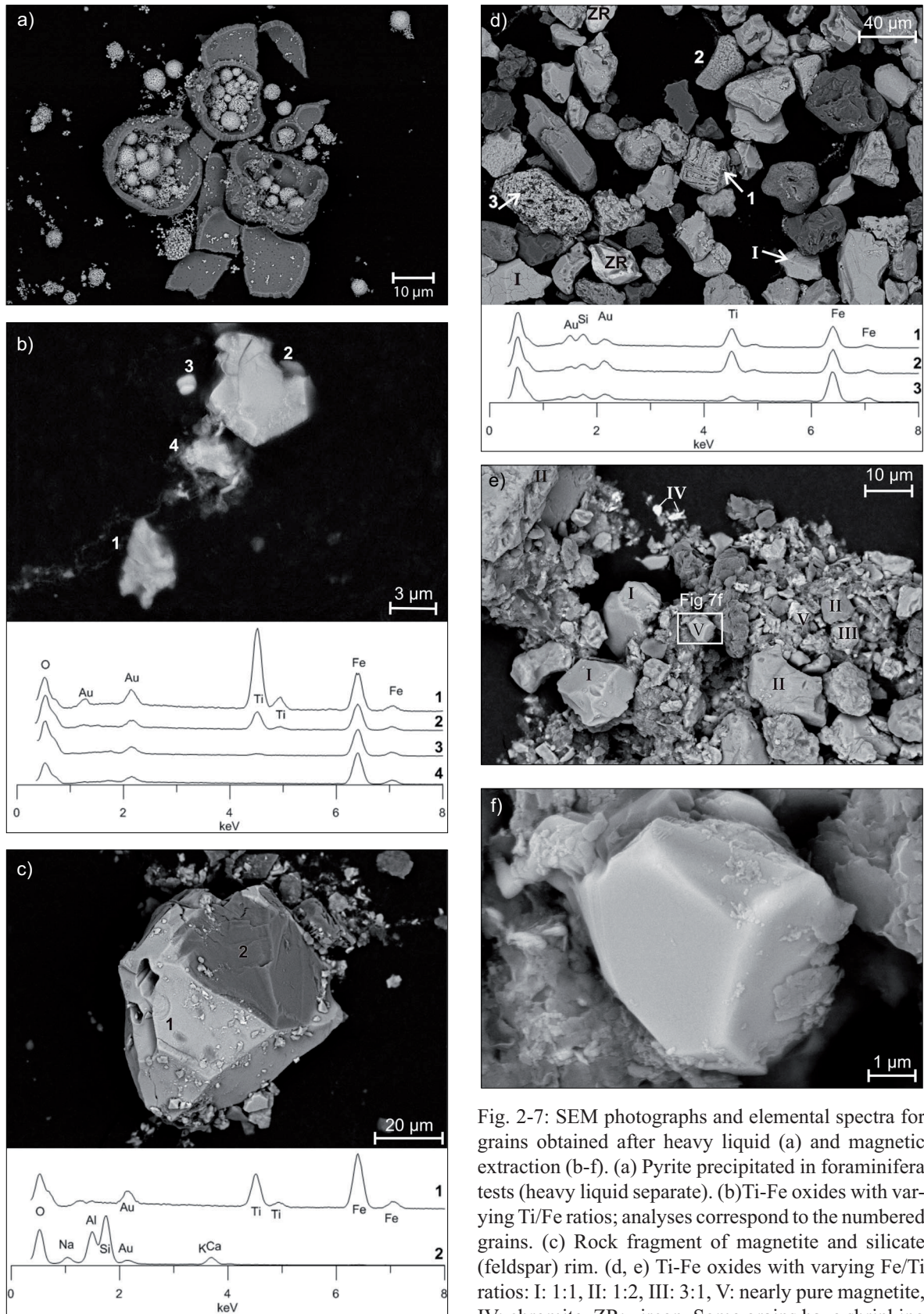


Fig. 2-7: SEM photographs and elemental spectra for grains obtained after heavy liquid (a) and magnetic extraction (b-f). (a) Pyrite precipitated in foraminifera tests (heavy liquid separate). (b) Ti-Fe oxides with varying Ti/Fe ratios; analyses correspond to the numbered grains. (c) Rock fragment of magnetite and silicate (feldspar) rim. (d, e) Ti-Fe oxides with varying Fe/Ti ratios: I: 1:1, II: 1:2, III: 3:1, V: nearly pure magnetite, IV: chromite, ZR: zircon. Some grains have shrinking cracks (d, lower left and right of the picture) and skeletal ilmenite lamellae (1). (f) Close-up of idiomorphic magnetite grain.

ble magnetite has been dissolved under reducing conditions (Canfield et al. 1992; Nowaczyk 2011). Gehring et al. (1995; 2007) and Fischer et al. (2008) inferred from magnetite dissolution in soil samples from Mali that the prevailing strong seasonality induces fluctuating redox conditions in the soils. Since in the respective EM A sample pyrite is very sparse (cf., Fig. 2-6g) we suggest that dissolution already occurred in the soil in the source area.

TEM analyses reveal that the sub-micron magnetic fraction has a high abundance of fossil magnetosomes (Fig. 2-8a, b, c, g) with cubo-octahedral or bullet shaped morphologies organized in long chains or clusters (Fig. 2-8b, c). Electron diffraction patterns reveal that the magnetosomes consist of magnetite (Fig. 2-8d, e). To estimate and compare their concentration in the three studied samples is difficult. However, the EM A sample (Fig. 2-8f) has by far the lowest amount of magnetosomes with respect to detrital particles which consists mainly of titanomagnetites and silicates. The presence of silicates in magnetic extracts points to magnetite inclusions within the host grains (Fig. 2-8f). In the sub-micron fraction of the EM B sample only magnetosomes were identified.

2.6 Discussion

Our approach reveals the magnetic mineralogy of aeolian and fluvial sediments at our study site. The magnetic inventory of the aeolian and fluvial EM can be used to assess the paleoenvironmental conditions in their source area. For our

study area, terrigenous sediments are exported from at least two source areas, while being transported by different mechanisms.

The pedogenic signature of magnetic iron oxides in terrestrial soils (Kämpf and Schwertmann 1983; Schwertmann and Taylor 1989; France and Oldfield 2000) and loess sequences (Maher 1986; Maher and Thompson 1992; Spassov et al. 2003) has been widely studied. Parent rock petrology, Eh/pH conditions and water content control the speciation of pedogenic iron minerals (Kämpf and Schwertmann 1983). As the ratio of pedogenically formed hematite/goethite lowers with decreasing soil temperature and excess water within the soil (Maher 1986; Schwertmann and Taylor 1989), the ratio of those minerals can be related to climatic variations. Accordingly, in the South China Sea (Zhang et al. 2007), and off the Amazon (Harris and Mix 1999), the goethite/hematite ratio has been used to reconstruct past precipitation. However, the use of this ratio has to be handled carefully. In a geological setting where reductive diagenesis occurs, an increase of this ratio could simply result from the dissolution of goethite with respect to the more stable hematite (Abrajevitch et al. 2009; Abrajevitch and Kodama 2011).

2.6.1 Aeolian signature

The high hematite over goethite content of EM A suggests that relatively dry conditions prevailed during terrestrial pedogenesis. *Sarnthein et al.* (1981) and *Bloemendal et al.* (1988; 1992) found that dust derived from the southern Sa-

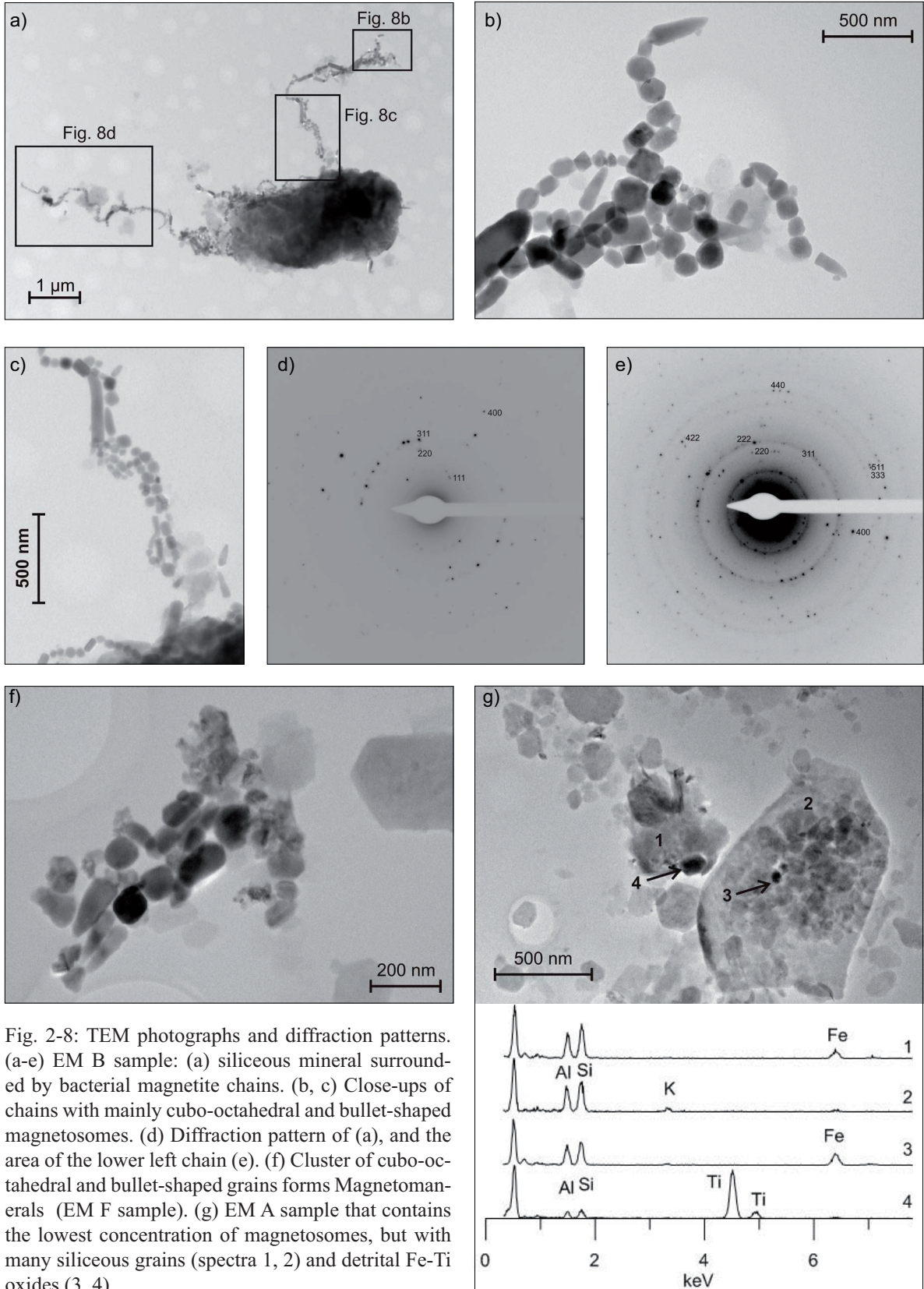


Fig. 2-8: TEM photographs and diffraction patterns. (a-e) EM B sample: (a) siliceous mineral surrounded by bacterial magnetite chains. (b, c) Close-ups of chains with mainly cubo-octahedral and bullet-shaped magnetosomes. (d) Diffraction pattern of (a), and the area of the lower left chain (e). (f) Cluster of cubo-octahedral and bullet-shaped grains forms Magnetominerals (EM F sample). (g) EM A sample that contains the lowest concentration of magnetosomes, but with many siliceous grains (spectra 1, 2) and detrital Fe-Ti oxides (3, 4).

hara and northern Sahel contains a high hematite content, mainly as coatings on quartz grains. Similar results have recently been found for terrestrial sand samples from those regions (Lyons et al. 2010). It is inferred that these high-coercivity hematite coatings are secondary minerals formed within soils. The content of SP grains within the coarse sediment fraction of the soils (Lyons et al. 2010) is consistent with the high frequency dependence of susceptibility in the interval of HS 1 in GeoB 13602-1 (cf. Fig. 2-3a), where EM A is highly dominant.

2.6.2 Fluvial signature

The magnetic inventory of soil and desert sand samples from the Sahara and Sahel contains abundant high-coercivity magnetic minerals (goethite and/or hematite) in areas with higher precipitation (Lyons et al. 2010). Under more humid conditions in the catchment area of the Gambia River, pedogenic goethite should be more abundant than hematite (Maher 1986; Schwertmann and Taylor 1989). Lush savanna vegetation must have prevented soil mobilization by wind while sheet and stream erosion in rainy seasons were favored.

Gac and Kane (1986) reported that bulk fluvial sediments from the Senegal River, which drains a larger, but climatically similar basin as the Gambia River, also contain goethite.

Our interpretation of EM F, which is only dominant in the proximal core GeoB 13602-1, as fluvial sediment is further supported by satellite images that show a modern deflection of the

Gambia fresh water fan to the north. Likewise this indicates that also during MIS 1-3 northward directed surface currents prevailed so that the fluvial material was deposited at the northern site. Coercivity analysis of EM F and thermomagnetic results from peak concentration samples suggest a relatively low concentration of magnetite and hematite and a particular high concentration of goethite. Particularly high EM F levels are observed at least during the early AHP.

2.6.3 Bacterial signature

EM B contains a magnetic mineralogy with a narrow coercivity spectrum. Coercivity spectra with such low dispersions have only been observed for magnetite or greigite formed within the cells of magnetotactic bacteria (Kruiver and Passier 2001; Egli 2004b; Vasiliev et al. 2007). However, from magnetization vs. temperature measurements above room temperature, we can rule out the presence of greigite because the typical irreversible oxidation of greigite between 200 and 400°C (Reynolds et al. 1994; Vasiliev et al. 2007) is not detectable. TEM analysis unequivocally reveals that magnetosomes are present and extremely abundant in the interval where EM B dominates. Previously, a hard magnetite phase was linked to fluvial sediments (Itambi et al. 2010). Magnetosomes were considered unlikely to be a significant contributor to the sediment magnetic properties in the environment as offshore of NW Africa for two main reasons. First, in areas with high terrig-

enous input with high concentration of magnetic minerals, the magnetic signature of the magnetosomes would be insignificant compared to that of the terrigenous signal. Second, magnetotactic bacteria occur above the iron-redox boundary, (Karlin et al. 1987; Petermann and Bleil 1993) and at least magnetite magnetosomes should rapidly dissolve during burial with upward redox boundary migration (e.g. Hilgenfeldt 2000). However, our results indicate that magnetosomes contribute up to 60% of the SIRM and are preserved even below the present iron-redox boundary (cf. section 2.6.4). The presence of EM B in the strongly depleted lower intervals of the cores is unlikely to be linked to fossil magnetosomes that survive reductive dissolution. However, note that SIRM in those intervals is lower (<10%) with respect to the remainder of the record leading to a small contribution of EM B when expressed in absolute values (cf. 2.5.2). We infer that the contribution in the respective sections is attributed to inaccuracies of unmixing of the lower record, because instrumental noise is higher with respect to signal of the magnetic minerals. The reduction of EM B for the pooled data set in the respective intervals, supports this suggestion.

2.6.4 Diagenetic signature

The prominent change in magnetic properties in the lower sections and the near-surface layer of the cores reflects a near-complete loss of fine grained Fe oxide mineral particles. Reductive dissolution of iron oxides is a function of surface

area (Canfield and Berner 1987), therefore fine grained magnetite is more rapidly and pervasively dissolved (Karlin and Levi 1983). Both zones have high contributions of EM D. The relict magnetic mineral inventory consists of intermediate- and high-coercivity minerals and probably correspond to Ti^{4+} rich and therefore Fe^{3+} poor Fe-Ti oxide phases as well as some apparently more resistive antiferromagnetic mineral phases (Robinson et al. 2000; Emiroglu et al. 2004; Garming et al. 2005; Dillon and Bleil 2006; Nowaczyk 2011).

We suggest that the lower depleted zone marks the modern sulfate-methane transition (SMT). Above, iron oxides are reduced to pyrite in organic rich micro-environments like foraminifera tests (Mohamed et al. 2011). The magnetite loss in the narrow subsurface horizon results from (most likely microbially mediated) redox reactions at the present iron-redox boundary (Riedinger et al. 2005). Under steady-state redox conditions, the iron-redox boundary would have migrated successively upward in equilibrium with sedimentation and led to a general reduction of fine grained iron (oxyhydr)oxides. However, high bacterial magnetite contents in between the modern iron-redox boundary and the present SMTZ rule out such a migration.

Karlin (1990) reports the preservation of ultra fine grained magnetite in certain intervals in a core below the present iron-redox boundary. From this finding he inferred non-steady-state redox conditions, which was attributed to varying sedimentation rates. Compared to the

Holocene, sedimentation rates in GeoB 13602-1 were doubled during MIS2 and MIS3 and even up to seven times higher during HS 1 and the Younger Dryas. We therefore infer that the enhanced sedimentation rates during the MIS 3 and MIS 2, led to a rapid burial of the detrital and the authigenic iron-oxides (magnetosomes) and a fast-upward migration of the iron redox boundary, and accordingly, the preservation of the magnetic minerals.

The near-surface depleted layer is located just below an organic carbon peak (and associated carbonate minimum) in the uppermost 10 cm of GeoB 13602-1 (Fig. 2-2), which dates to the termination of the African Humid period at 5.5 ka (deMenocal et al. 2000). Variations in the organic carbon supply could also influence the more pervasive dissolution of magneto minerals in this near-surface zone (e.g., Tarduno and Wilkison 1996). Over the rest of the Holocene and LGM organic carbon is much lower, especially during HS 1, probably because of lower productivity and higher dilution of organic matter by siliciclastics.

Magnetite depletion in deep as well as in sub-surface sediment layers are also evident in nearby cores (cf. Fig. 2-1a) GeoB 9527-5 (close to GeoB 13601-4) and GeoB 9506-1 from the continental margin in the Sahel but is absent in core GeoB 9516-5 which is close to GeoB 13602-1 (Itambi et al. 2009). The ages attributed to the reductive layers are different for the cores investigated by Itambi et al. (2009) and these from our study. However, the sedimenta-

tion rates in those cores are half as high as in ours which as outlined above also have a significant impact on the organic carbon content, pore-water geochemistry, and geochemical zonation and respectively reductive diagenesis (e.g., Tarduno and Wilkison 1996).

2.6.5 Paleoclimatic implications

The unmixing of the terrigenous fraction enables the estimation of the dust/river variations in our record. A distinction of dust emitted from different source areas is not evident from our data. Thus, we cannot infer whether dust is transported by the Trades or AEJ. This outcome suggests that dust either originates from only one source area, or that the EM unmixing of IRM acquisition curves is not capable of differentiating between potential dust sources. The latter could be due to a similar magnetic mineralogy of soils in the source areas, or arise by a co-variation of the AEJ input and the Trades or river supply.

Changing proportions of fluvial and aeolian EMs reflect environmental and paleoclimatic changes in the study area. In Fig. 2-9 the contribution of EM A and EM F normalized to 1 is shown to correct for the varying contributions of EM B. The intervals of reductive diagenesis are not considered as well. EM F is virtually absent in GeoB 13601-4, therefore we only show the plot for GeoB 13602-1. Peaks are evident in EM A during HS 5, HS 4, and increase during the LGM and the successive major peak during HS1 indicates (much) drier conditions during

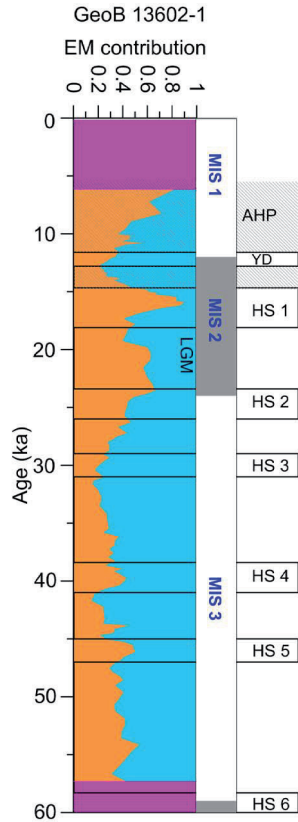


Fig. 2-9: Down-core record (0-60 ka) of EM A (orange) and EM F (blue) for core GeoB 13602-1 normalized to 1 (derived from the merged data set, cf. Fig. 4f). During HS 5, 4, the LGM and HS1 dust input is enhanced. During the AHP, conditions are comparable to MIS 3. The interval within which the SIRM is strongly reduced, and where reductive diagenesis has affected the record (also expressed by a strong contribution of EM D), is colored pink.

those periods. Likewise, the rock magnetic parameters have minima during HS 5, HS 4, HS 2 and HS 1 (cf. Fig. 2-3). In contrast, during HS 3, our data do not indicate dry conditions.

Contemporaneously to the deposition of Heinrich Layers (HL) in the North Atlantic, ‘dusty events’ (Jullien et al. 2007) in low latitudes were associated with a reduction of the meridional overturning circulation and a southward shift of the ITCZ and the associated rain belt (Mulitza et al. 2008). While the geochemical signature of the detritus of HL 1, HL 2, HL 4, and HL5 suggests Canadian sources (e.g., Hemming et al. 1998), HL 3 grains are probably derived from Greenland and Scandinavia (Gwiazda et al. 1996). Numerical modeling by Seidov & Maslin (1999) of the influence of meltwater input into the North Atlantic indicates that for disturb-

ing the NADW production not the total amount of meltwater but its transport to the convection site is mostly important. It was suggested that the deep water formation resumed more rapidly at the end of Heinrich event 3 with respect to the stronger Heinrich events (Elliot et al. 2002). Since the lowest expression of all observed HSS in our record is HS 3, it may be hypothesized that less dry conditions are a low-latitude expression of a rather weak disturbance of the meridional overturning circulation.

By far the highest contribution of dust occurs during HS 1. Similar results have been suggested from rock magnetic records of Itambi et al. (2009) and from geochemical proxies (Mulitza et al. 2008). This indicates that the ITCZ (and rain-belt) retreated further to the south during HS 1 with respect to the remaining HSS. The ITCZ shift also induces a longer season of prevailing NE Trades. We additionally infer that the longer term arid conditions during the LGM and associated reduced vegetation cover in the hinterland (e.g., Mahowald et al. 1999) exposed larger areas for aeolian deflation. The combination of aridity and stronger/longer trade winds season are probably responsible for the high dust content during HS 1. Studies about past dust accumulation off NW Africa have been integrated in the DIRTMAP Project (Kohfeld and Harrison 2001), of which the sites carried out in the proximity of our study region report 2 to 6 times higher dust accumulation during the LGM compared to the present.

EM F is literally absent during HS 1, therefore

the sedimentation of the terrigenous fraction corresponds exclusively to dust. Since terrigenous sedimentation rate during HS 1 is much higher with respect to the other HSs and the LGM (see Fig. 2-2), we infer that the dust export from the NW African continent was at least twofold with respect to the remaining HSs and even four times higher with respect to the LGM.

Recently, Roberts et al. (2011) found that dust export from the Arabian-Chinese dust belt was much stronger during glacial terminations and, accordingly, accompanying HSs than during glacials. These periods have been linked to less precipitation in the Eurasian desert due to a weaker monsoon (Roberts et al. 2011). Their findings in conjunction with similarly arid conditions in NW Africa underline the teleconnection between the North Atlantic and general northern hemispheric atmospheric features.

After HS 1, EM F gains more influence indicating more humid conditions. This period corresponds to the early AHP (Ritchie et al. 1985; deMenocal et al. 2000), while during the late AHP the fluvial influence decreases. A return to more arid conditions during the Younger Dryas, which has been reported from gravity cores off the Senegal River (Mulitza et al. 2008) is not evident in our core. However, their study site lies about 400 km north of our study area and it may be hypothesized that during the Younger Dryas desertification and associated dust export did not retreat as far south. Similar conclusions have been drawn from geochemical proxies (Collins et al. 2011), with a contrast of arid conditions

during HS 1 and the LGM and humid conditions during the Holocene diminishing from arid toward subtropical Africa.

Like other studies using geochemical and grain-size data, the rock magnetic approach is capable of detecting changes in fluvial and aeolian content in marine sediments. From a technical viewpoint magnetic analyses are less time consuming because no sample preparation is needed and measurements can be highly automated. Magnetic minerals are also more resistant to chemical weathering than feldspars, and are only subject to mechanical abrasion. In contrast, geochemical data from Saharan dust indicate that sediments from the same source area may have differing elemental ratios due to fractionation during transport (e.g., Caquineau et al. 1998), which is attributed to fall out of coarser components (e.g., quartz and feldspars) with respect to fine (clay) minerals. Accordingly, elemental ratios as well as grain-size distributions of aeolian and fluvial material may be influenced by differing transport energies (e.g., higher wind speeds or energetically higher river discharge). Similar to approaches using clay minerals (Caquineau et al. 1998; 2002), even in combination with grain-size data and elemental ratios (Stuut et al. 2005), magnetic mineralogy is helpful for explicitly identifying sediments from different source areas. Moreover, since the formation of pedogenic iron-oxides is highly dependent on environmental settings, information about climatic conditions in the source areas may be inferred.

However, our study shows that when using magnetic properties for paleoclimatic reconstruction, special attention must be paid to the potential occurrence of magnetotactic bacteria and their contribution to the magnetic signal (Roberts et al. 2011) even in settings with high organic carbon accumulation and terrigenous input.

2.7 Conclusions

EM and IRM component analyses of rock magnetic properties from two contrasting sites enabled us to differentiate magnetic signatures and to quantify contributions of primary terrigenous source materials and of secondary post-depositional bacterial biomineralization and diagenetic relict phases to the IRM. Decomposition of the record into EMs provides a more robust understanding of the record within its paleoenvironment. The main contributors of the terrigenous sediment fraction at the studied sites are dust exported by the African wind systems (NE Trades, African Easterly Jet) and fluvial sediment discharge mainly by the Gambia River. Both terrigenous EMs have marked differences in terms of magnetic mineralogy. Dust contains a higher proportion of magnetite and a lower proportion of goethite with respect to the fluvial material. This feature mirrors the environmental conditions on land, since in more humid areas goethite is formed over hematite and vice versa. The contributions of EMs not only imply drier conditions during the LGM and especially HS 1 and humidification during the AHP, but also en-

able an estimation of dust fluxes. It is suggested the dust supply during HS1 is at least five times higher with respect to the LGM.

Reductive magnetic mineral diagenesis was observed in distinct layers from both cores (partial depletion in a shallow horizon at a depth of 0.1 to 0.2 m depth and pervasive depletion below ~7.50 m). These alteration zones are interpreted to mark the modern iron-redox boundary and sulfate-methane transition zone respectively. The signature of the magnetic relict fraction suggests a relative enrichment of reduction resistant Ti-rich titanomagnetites and hemoilmenites.

Unexpectedly for settings with high terrigenous inputs, we found high proportions of submicron bacterial magnetite that accounts for up to 60% of the total SIRM. This demonstrates the potential contribution of bacterial biomineralization complicating the interpretation of magnetic mineral data in terms of sediment provenance. One possibility is to identify such a bacterial EM and subtract its influence to enable a more meaningful analysis of the terrigenous magnetic fraction.

Acknowledgments

We thank the crew and scientific party of *Maria S. Merian* cruise MSM 11/2 for helping to collect the studied cores, Thomas Frederichs for help with MPMS measurements and interpretation, Tom Mullender for helping with Curie balance measurements, Monika Segl for providing oxygen isotope measurements, Hella Buschhoff

for carbon content analyses and Petra Witte for driving the SEM. We acknowledge the constructive suggestions of Andrew Roberts and one anonymous reviewer. This study was enabled by funding of the Deutsche Forschungsgemeinschaft (DFG) through the international graduate college EUROPROX- Proxies in Earth History.

References

- Abrajevitch A, der Voo RV, Rea DK (2009) Variations in relative abundances of goethite and hematite in Bengal Fan sediments: Climatic vs. diagenetic signals. *Mar. Geol.* 267:191-206
- Abrajevitch A, Kodama K (2011) Diagenetic sensitivity of paleoenvironmental proxies: A rock magnetic study of Australian continental margin sediments. *Geochem. Geophys. Geosyst.* 12:Q05Z24
- Bloemendal J, Lamb B, King J (1988) Paleoenvironmental implications of rock-magnetic properties of late Quaternary sediment cores from the eastern equatorial Atlantic. *Paleoceanography* 3:61-87
- Bloemendal J, King JW, Hall FR, Doh SJ (1992) Rock Magnetism of Late Neogene and Pleistocene deep-sea sediments: Relationship to sediment source, diagenetic processes, and sediment lithology. *J. Geophys. Res.* 97:4361-4375
- Bloemendal J, King JW, Hunt A, Demenocal PB, Hayashida A (1993) Origin of the sedimentary magnetic record at Ocean Drilling Program sites on the Owen Ridge, western Arabian Sea. *J. Geophys. Res.* 98:4199-4219
- Broecker WS (1998) Paleocirculation during the last deglaciation: A bipolar seesaw? *Paleoceanography* 13:119-121
- Canfield DE, Berner RA (1987) Dissolution and pyritization of magnetite in anoxic marine sediments. *Geochim. Cosmochim. Acta* 51:645-659
- Canfield DE, Raiswell R, Bottrell SH (1992) The reactivity of sedimentary iron minerals toward sulfide. *Am. J. Sci.* 292:659-683
- Caquineau S, Gaudichet A, Gomes L, Magonthier M-C, Chatenet B (1998) Saharan dust: Clay ratio as a relevant tracer to assess the origin of soil derived aerosols. *Geophys. Res. Lett.* 25:983-986
- Caquineau S, Gaudichet A, Gomes L, Legrand M (2002) Mineralogy of Saharan dust transported over northwestern tropical Atlantic Ocean in relation to source regions. *J. Geophys. Res.* 107:4251
- Chiapello I, Bergametti G, Gomes L, Chatenet B, Dulac F, Pimenta J, Soares ES (1995) An additional low layer transport of Sahelian and Saharan dust over the northeastern Tropical Atlantic. *Geophys. Res. Lett.* 22:3191-3194
- Collins JA, Schefusz E, Heslop D, Mulitza S, Prange M, Zabel M, Tjallingii R, Dokken TM, Huang E, Mackensen A, Schulz M, Tian J, Zarriess M, Wefer G (2011) Interhemispheric symmetry of the tropical African rainbelt over the past 23,000 years. *Nature Geosci.* 4:42-45
- Dearing JA, Dann R, Hay K, Lees JA, Loveland PJ, Maher BA, O'Grady K (1996) Frequency-dependent susceptibility measurements of environmental materials. *Geophys. J. Int.* 124:228-240
- Dekkers MJ (1989) Magnetic properties of natural Goethite II. TRM behaviour during thermal and alternating field demagnetization and low-temperature treatment. *Geophys. J. Int.* 97:341-355
- deMenocal P, Ortiz J, Guilderson T, Adkins J, Sarnthein M, Baker L, Yarusinsky M (2000) Abrupt onset and termination of the African Humid Period: Rapid climate responses to gradual insolation forcing. *Quat. Sci. Rev.* 19:347-361
- Dillon M, Bleil U (2006) Rock magnetic signatures in diagenetically altered sediments from the Niger deep-sea fan. *J. Geophys. Res.* 111:B03105
- Egli R, Lowrie W (2002) An hysteretic remanent magnetization of fine magnetic particles. *J. Geophys. Res.* 107:2209
- Egli R (2003) Analysis of the field dependence of remanent magnetization curves. *J. Geophys. Res.* 108:2081
- Egli R (2004a) Characterization of individual rock magnetic components by analysis of remanence curves, 1. Unmixing natural sediments. *Stud. Geophys. Geodaet.* 48:391-446
- Egli R (2004b) Characterization of individual rock magnetic components by analysis of remanence curves, 3. Bacterial magnetite and natural processes in lakes. *Phys. Chem. Earth, Parts A/B/C* 29:869-884
- Elliot M, Labeyrie L, Duplessy J-C (2002) Changes in North Atlantic deep-water formation associated with the Dansgaard-Oeschger temperature oscillations (60–10 ka). *Quat. Sci. Rev.* 21:1153-1165
- Emiroglu S, Rey D, Petersen N (2004) Magnetic properties of sediment in the Ría de Arousa (Spain): Dissolution of iron oxides and formation of iron sulphides. *Phys. and Chem. of the Earth, Parts A/B/C* 29:947-959
- Eyre J (1996) The application of high resolution IRM acquisition to the discrimination of remanence carriers in Chinese loess. *Stud. Geophys. Geodaet.*

- 40:234-242
- Fischer H, Luster J, Gehring AU (2008) Magnetite weathering in a Vertisol with seasonal redox-dynamics. *Geoderma* 143:41-48
- Fitzpatrick RW, Schwertmann U (1982) Al-substituted goethite--An indicator of pedogenic and other weathering environments in South Africa. *Geoderma* 27:335-347
- France DE, Oldfield F (2000) Identifying goethite and hematite from rock magnetic measurements of soils and sediments. *J. Geophys. Res.* 105:2781-2795
- Frank U, Nowaczyk NR (2008) Mineral magnetic properties of artificial samples systematically mixed from haematite and magnetite. *Geophys. J. Int.* 175:449-461
- Franke C, Frederichs T, Dekkers MJ (2007) Efficiency of heavy liquid separation to concentrate magnetic particles. *Geophys. J. Int.* 170:1053-1066
- Frederichs T, Bleil U, Däumler K, von Dobeneck T, Schmidt A (eds) (1999) *The magnetic view on the marine paleoenvironment: Parameters, techniques and potentials of rock magnetic studies as a key to paleoclimatic and paleoceanographic changes.* Springer, Berlin, Heidelberg.
- Gac JY, Kane A (1986) Le fleuve Sénégal: I Bilan hydrologique et flux continentaux der matières particulaires a l'embouchure. *Sci. Geol. Bull* 39:99-130
- Garming JFL, Bleil U, Riedinger N (2005) Alteration of magnetic mineralogy at the sulfate-methane transition: Analysis of sediments from the Argentine continental slope. *Phys. Earth Planet. Inter.* 151:290-308
- Gehring AU, Guggenberger G, Zech W, Luster J (1995) Combined magnetic, spectroscopic, and analytical-chemical approach to infer genetic information for a vertisol. *Soil Sci. Soc. Am. J.* 61:78-85
- Gehring AU, Fischer H, Schill E, Granwehr J, Luster J (2007) The dynamics of magnetic ordering in a natural hemo-ilmenite solid solution. *Geophys. J. Int.* 169:917-925
- Gwiazda RH, Hemming SR, Broecker WS (1996) Provenance of icebergs during heinrich event 3 and the contrast to their sources during other heinrich episodes. *Paleoceanography* 11:371-378
- Harris SE, Mix AC (1999) Pleistocene precipitation balance in the Amazon basin recorded in deep sea sediments. *Quat. Res.* 51:14-26
- Hemming SR, Broecker WS, Sharp WD, Bond GC, Gwiazda RH, McManus JF, Klas M, Hajdas I (1998) Provenance of Heinrich layers in core V28-82, northeastern Atlantic: $^{40}\text{Ar}/^{39}\text{Ar}$ ages of ice-rafted hornblende, Pb isotopes in feldspar grains, and Nd-Sr-Pb isotopes in the fine sediment fraction. *Earth Planet. Sci. Lett.* 164:317-333
- Heslop D, McIntosh G, Dekkers MJ (2004) Using time- and temperature-dependent Preisach models to investigate the limitations of modelling isothermal remanent magnetization acquisition curves with cumulative log Gaussian functions. *Geophys. J. Int.* 157:55-63
- Heslop D, Dillon M (2007) Unmixing magnetic remanence curves without *a priori* knowledge. *Geophys. J. Int.* 170:556-566
- Heslop D, von Dobeneck T, Höcker M (2007) Using non-negative matrix factorization in the "unmixing" of diffuse reflectance spectra. *Mar. Geol.* 241:63-78
- Heslop D (2009) On the statistical analysis of the rock magnetic S-ratio. *Geophys. J. Int.* 178:159-161
- Hilgenfeldt K (2000) Diagenetic dissolution of biogenic magnetite in surface sediments of the Benguela upwelling system. *Int. J. Earth Sci.* 88:630-640
- Hounslow MW, Maher BA (1996) Quantitative extraction and analysis of carriers of magnetization in sediments. *Geophys. J. Int.* 124:57-74
- Hounslow MW, Morton AC (2004) Evaluation of sediment provenance using magnetic mineral inclusions in clastic silicates: comparison with heavy mineral analysis. *Sed. Geol.* 171:13-36
- Itambi AC, von Dobeneck T, Mulitza S, Bickert T, Heslop D (2009) Millennial-scale northwest African droughts related to Heinrich events and Dansgaard-Oeschger cycles: Evidence in marine sediments from offshore Senegal. *Paleoceanography* 24:PA1205
- Itambi AC, von Dobeneck T, Dekkers MJ, Frederichs T (2010) Magnetic mineral inventory of equatorial Atlantic Ocean marine sediments off Senegal-glacial and interglacial contrast. *Geophys. J. Int.* 183:163-177
- Jullien E, Grousset F, Malaizé B, Duprat J, Sanchez-Goni MF, Eynaud F, Charlier K, Schneider R, Bory A, Bout V, Flores JA (2007) Low-latitude "dusty events" vs. high-latitude "icy Heinrich events". *Quat. Res.* 68:379-386
- Kakol Z, Sabol J, Stickler J, Honig JM (1992) Effect of low-level titanium(IV) doping on the resistivity of magnetite near the Verwey transition. *Phys. Rev. B* 46:1975-1978
- Kämpf N, Schwertmann U (1983) Goethite and hematite in a climosequence in southern Brazil and their application in classification of kaolinitic soils. *Geoderma* 29:27-39
- Karlin R, Levi S (1983) Diagenesis of magnetic minerals in recent haemipelagic sediments. *Nature* 303:327-330
- Karlin R, Lyle M, Heath GR (1987) Authigenic magnetite formation in suboxic marine sediments. *Nature* 326:490-493
- Karlin R (1990) Magnetic mineral diagenesis in subox-

- ic sediments at Bettis site W-N, NE Pacific ocean. *J. Geophys. Res.* 95:4421-4436
- King J, Banerjee SK, Marvin J, Özdemir Ö (1982) A comparison of different magnetic methods for determining the relative grain size of magnetite in natural materials: Some results from lake sediments. *Earth Planet. Sci. Lett.* 59:404-419
- Knoll M, Hernández-Guerra A, Lenz B, López Laatzén F, Machín F, Müller TJ, Siedler G (2002) The Eastern Boundary Current system between the Canary Islands and the African coast. *Deep Sea Res. Part II* 49:3427-3440
- Kohfeld KE, Harrison SP (2001) DIRTMAP: the geological record of dust. *Earth Sci. Rev.* 54:81-114
- Köhler CM, Heslop D, Dekkers MJ, Krijgsman W, van Hinsbergen DJJ, von Dobeneck T (2008) Tracking provenance change during the late Miocene in the eastern Mediterranean using geochemical and environmental magnetic parameters. *Geochem. Geophys. Geosys.* 9
- Kruiver PP, Dekkers MJ, Heslop D (2001) Quantification of magnetic coercivity components by the analysis of acquisition curves of isothermal remanent magnetisation. *Earth Planet. Sci. Lett.* 189:269-276
- Kruiver PP, Passier H (2001) Coercivity analysis of magnetic phases in sapropel S1 related to variations in redox conditions, including an investigation of the S ratio. *Geochem. Geophys. Geosyst.* 2
- Larrasoaña JC, Roberts AP, Rohling EJ, Winkhofer M, Wehausen R (2003) Three million years of monsoon variability over the northern Sahara. *Clim. Dyn.* 21:689-698
- Liu Q, Yu Y, Torrent J, Roberts AP, Pan Y, Zhu R (2006) Characteristic low-temperature magnetic properties of aluminous goethite [α -(Fe, Al)OOH] explained. *J. Geophys. Res.* 111:B12S34
- Lowrie W, Heller F (1982) Magnetic properties of marine limestones. *Rev. Geophys.* 20:171-192
- Lyons R, Oldfield F, Williams E (2010) Mineral magnetic properties of surface soils and sands across four North African transects and links to climatic gradients. *Geochem. Geophys. Geosys.* 11:Q08023
- Maher BA (1986) Characterisation of soils by mineral magnetic measurements. *Phys. Earth Planet. Inter.* 42:76-92
- Maher BA, Thompson R (1992) Paleoclimatic significance of the mineral magnetic record of the Chinese loess and paleosols. *Quat. Res.* 37:155-170
- Maher BA, Watkins SJ, Brunskill G, Alexander J, Fielding CR (2009) Sediment provenance in a tropical fluvial and marine context by magnetic 'fingerprinting' of transportable sand fractions. *Sedimentology* 56:841-861
- Mahowald N, Kohfeld K, Hansson M, Balkanski Y, Harrison SP, Prentice IC, Schulz M, Rodhe H (1999) Dust sources and deposition during the last glacial maximum and current climate: A comparison of model results with paleodata from ice cores and marine sediments. *J. Geophys. Res.* 104:15895-15916
- Mittelstaedt E (1991) The ocean boundary along the northwest African coast: Circulation and oceanographic properties at the sea surface. *Progress In Oceanography* 26:307-355
- Mohamed KJ, Rey D, Rubio B, Dekkers MJ, Roberts AP, Vilas F (2011) Onshore-offshore gradient in reductive early diagenesis in coastal marine sediments of the Ria de Vigo, Northwest Iberian Peninsula. *Cont. Shelf Res.* 31:433-447
- Moskowitz BM, Frankel RB, Bazylinski DA (1993) Rock magnetic criteria for the detection of biogenic magnetite. *Earth Planet. Sci. Lett.* 120:283-300
- Mulitza S, Prange M, Stuut JB, Zabel M, von Dobeneck T, Itambi AC, Nizou J, Schulz M, Wefer G (2008) Sahel megadroughts triggered by glacial slowdowns of Atlantic meridional overturning. *Paleoceanography* 23:PA4206
- Mullender TAT, van Velzen AJ, Dekkers MJ (1993) Continuous drift correction and separate identification of ferrimagnetic and paramagnetic contributions in thermomagnetic runs. *Geophys. J. Int.* 114:663-672
- Nowaczyk NR (2011) Dissolution of titanomagnetite and sulphidization in sediments from Lake Kinneret, Israel. *Geophys. J. Int.* 187:34-44
- Özdemir Ö, Dunlop DJ, Moskowitz BM (1993) The effect of oxidation on the Verwey transition in magnetite. *Geophys. Res. Lett.* 20:1671-1674
- Passier HF, De Lange GJ, Dekkers MJ (2001) Magnetic properties and geochemistry of the active oxidation front and the youngest sapropel in the eastern Mediterranean Sea. *Geophys. J. Int.* 145:604-614
- Petermann H, Bleil U (1993) Detection of live magnetotactic bacteria in South Atlantic deep-sea sediments. *Earth Planet. Sci. Lett.* 117:223-228
- Peters C, Dekkers MJ (2003) Selected room temperature magnetic parameters as a function of mineralogy, concentration and grain size. *Phys. Chem. Earth, Parts A/B/C* 28:659-667
- Petersen N, von Dobeneck T, Vali H (1986) Fossil bacterial magnetite in deep-sea sediments from the South Atlantic Ocean. *Nature* 320:611-615
- Petersen N, Vali H (1987) Observation of shrinkage cracks in ocean floor titanomagnetites. *Phys. Earth Planet. Inter.* 46:197-205
- Petrovský E, Hejda P, Zelinka T, Kropáček V, Subrt J (1993) Experimental determination of magnetic interactions within a system of synthetic haematite particles. *Phys. Earth Planet. Inter.* 76:123-130

- Prins M (1999) Pelagic, hemipelagic and turbidite deposition in the Arabian Sea during the late Quaternary. In: Aardwetenschappen. Universiteit Utrecht, Utrecht
- Pye K (1987) Aeolian dust and dust deposits. Academic press, London
- Reimer PJ, Baillie MGL, Bard E, Bayliss A, Beck JW, Blackwell PG, Ramsey CB, Buck CE, Burr GS, Edwards RL, Friedrich M, Grootes PM, Guilderson TP, Hajdas I, Heaton TJ, Hogg AG, Hughen KA, Kaiser KF, Kromer B, McCormac FG, Manning SW, Reimer RW, Richards DA, Southon JR, Talamo S, Turney CSM, van der Plicht J, Weyhenmeyer CE (2009) IntCal09 and Marine09 radiocarbon age calibration curves, 0–50,000 years cal BP. *Radiocarbon* 51:1111-1150
- Reynolds RL, Tuttle ML, Rice CA, Fishman NS, Karachewski JA, Sherman DM (1994) Magnetization and geochemistry of greigite-bearing Cretaceous strata, North Slope basin, Alaska. *Am. J. Sci.* 294:485-528
- Riedinger N, Pfeifer K, Kasten S, Garming JFL, Vogt C, Hensen C (2005) Diagenetic alteration of magnetic signals by anaerobic oxidation of methane related to a change in sedimentation rate. *Geochim. Cosmochim. Acta* 69:4117-4126
- Ritchie JC, Eyles CH, Haynes CV (1985) Sediment and pollen evidence for an early to mid-Holocene humid period in the eastern Sahara. *Nature* 314:352-355
- Roberts AP, Turner GM (1993) Diagenetic formation of ferrimagnetic iron sulphide minerals in rapidly deposited marine sediments, South Island, New Zealand. *Earth Planet. Sci. Lett.* 115:257-273
- Roberts AP, Florindo F, Villa G, Chang L, Jovane L, Bohaty SM, Larrasoana JC, Heslop D, Fitz Gerald JD (2011) Magnetotactic bacterial abundance in pelagic marine environments is limited by organic carbon flux and availability of dissolved iron. *Earth Planet. Sci. Lett.* 310:441-452
- Robertson DJ, France DE (1994) Discrimination of remanence-carrying minerals in mixtures, using isothermal remanent magnetisation acquisition curves. *Physics of The Earth and Planetary Interiors* 82:223-234
- Robinson SG, Sahota JTS, Oldfield F (2000) Early diagenesis in North Atlantic abyssal plain sediments characterized by rock-magnetic and geochemical indices. *Mar. Geol.* 163:77-107
- Rowan CJ, Roberts AP, Broadbent T (2009) Reductive diagenesis, magnetite dissolution, greigite growth and paleomagnetic smoothing in marine sediments: A new view. *Earth Planet. Sci. Lett.* 277:223-235
- Sarnthein M, Tetzlaff G, Koopmann B, Wolter K, Pflaumann U (1981) Glacial and interglacial wind regimes over the eastern subtropical Atlantic and North-West Africa. *Nature* 293:193-196
- Sarnthein, M., et al., Fundamental modes and abrupt changes in North Atlantic circulation and climate over the last 60 ky—Concepts, reconstructions and numerical modeling, in *The Northern North Atlantic: A Changing Environment*, edited by P. Schäfer et al., pp. 365–410, Springer-Verlag, New York, 2001.
- Schmidt AM, von Dobeneck T, Bleil U (1999) Magnetic characterization of Holocene sedimentation in the South Atlantic. *Paleoceanography* 14:465-481
- Schwertmann U, Taylor RM (1989) *Iron Oxides*. Soil Science Society of America Inc. (SSSA). Madison, USA
- Seidov D, Maslin M (1999) North Atlantic deep water circulation collapse during Heinrich events. *Geology* 27:23-26
- Shackleton NJ, Hall MA, Vincent E (2000) Phase relationships between millennial-scale events 64,000–24,000 years ago. *Paleoceanography* 15:565-569
- Smirnov AV, Tarduno JA (2000) Low-temperature magnetic properties of pelagic sediments (Ocean Drilling Program Site 805C): Tracers of maghemitization and magnetic mineral reduction. *J. Geophys. Res.* 105:16457-16471
- Spassov S, Heller F, Kretzschmar R, Evans ME, Yue LP, Nourgaliev DK (2003) Detrital and pedogenic magnetic mineral phases in the loess/palaeosol sequence at Lingtai (Central Chinese Loess Plateau). *Phys. Earth Planet. Inter.* 140:255-275
- Stocker TF, Wright DG (1991) Rapid transitions of the ocean's deep circulation induced by changes in surface water fluxes. *Nature* 351:729-732
- Stoner JS, Channell JET, Hillaire-Marcel C (1996) The magnetic signature of rapidly deposited detrital layers from the Deep Labrador Sea: Relationship to North Atlantic Heinrich layers. *Paleoceanography* 11:309-325
- Stuut J-B, Zabel M, Ratmeyer V, Helmke P, Schefuß E, Lavik G, Schneider R (2005) Provenance of present-day eolian dust collected off NW Africa. *J. Geophys. Res.* 110:D04202
- Tarduno JA, Wilkison SL (1996) Non-steady state magnetic mineral reduction, chemical lock-in, and delayed remanence acquisition in pelagic sediments. *Earth Planet. Sci. Lett.* 144:315-326
- Tomczak M (2003) *Regional oceanography: An introduction* Daya Publishing House
- Vali H, von Dobeneck T, Amarantidis G, Förster O, Morteani G, Bachmann L, Petersen N (1989) Biogenic and lithogenic magnetic minerals in Atlantic and Pacific deep sea sediments and their paleomagnetic significance. *Geologische Rundschau* 78:753-764
- Vasiliev I, Dekkers MJ, Krijgsman W, Franke C, Lang-

- ereis CG, Mullender TAT (2007) Early diagenetic greigite as a recorder of the palaeomagnetic signal in Miocene–Pliocene sedimentary rocks of the Carpathian foredeep (Romania). *Geophys. Journal Int.* 171:613-629
- von Dobeneck T, Petersen N, Vali H (1987) Bakterielle Magnetofossilien. *Geowissenschaften in unserer Zeit* 1:27-55
- Weltje G (1997) End-member modeling of compositional data: Numerical-statistical algorithms for solving the explicit mixing problem. *Mathemat. Geol.* 29:503-549
- Weltje GJ, Prins MA (2007) Genetically meaningful decomposition of grain-size distributions. *Sed. Geol.* 202:409-424
- White F (1983) A Descriptive Memoir to Accompany the UNESCO/AETFAT/UNSO Vegetation Map of Africa. In: United Nations Educational, Scientific, and Cultural Organization, Paris
- Zhang YG, Ji J, Balsam WL, Liu L, Chen J (2007) High resolution hematite and goethite records from ODP 1143, South China Sea: Co-evolution of monsoonal precipitation and El Niño over the past 600,000 years. *Earth Planet. Sci. Lett.* 264:136-150

Chapter 3

Multi-proxy characterization and budgeting of terrigenous end-members at the NW African continental margin

Janna Just^{1,2,3}, David Heslop⁴, Tilo von Dobeneck^{1,2,3}, Torsten Bickert^{1,2,3}, Mark J. Dekkers^{3,5}, Thomas Frederichs^{1,2}, Inka Meyer^{2,3}, Matthias Zabel^{2,3}

¹ Marine Geophysics, Depart. of Geosciences, Klagenfurter Strasse, University of Bremen, Germany.

² MARUM—Center for Marine Environmental Sciences, Leobener Strasse, University of Bremen, Germany.

³ International Graduate College EUROPROX.

⁴ Research School of Earth Sciences, The Australian National University, Canberra, Australia.

⁵ Paleomagnetic Laboratory 'Fort Hoofddijk', Depart. of Earth Sciences, Budapestlaan 17, Utrecht University, The Netherlands.

To submit to Geochemistry, Geophysics, Geosystem

Grain-size, terrigenous element and rock magnetic remanence data of Quaternary marine sediments retrieved at the NW African continental margin off Gambia (gravity core GeoB 13602-1, 13°32.71' N, 17°50.96' W, water depth 2,395 m, age 0-77 ka) were jointly analyzed by end-member (EM) un-mixing methods to distinguish and budget past terrigenous fluxes. We compare and cross-validate the identified single-parameter EM systems and develop a numerical strategy to calculate associated multi-parameter EM properties. Two fluvial and one aeolian EM could be identified by this joint analysis. The aeolian EM is much coarser than the two fluvial EMs and is associated with a lower goethite/hematite ratio, a higher relative concentration of magnetite and low Al/Si and Fe/K ratios. Accumulation rates and grain sizes of the fluvial sediment appear to be constrained by shore distance (i.e., sea-level fluctuations) and to a lesser extent by changes in hinterland precipitation. High dust fluxes occurred during the Last Glacial Maximum (LGM) and during Heinrich Stadials (HS) while the fluvial input remained unchanged. Our approach reveals that the LGM dust fluxes were ~7 times higher than today's. However, by far the highest dust accumulation occurred during HS 1 (~400 g m⁻² yr⁻¹): 80 to 100-fold higher fluxes than those of the Late Holocene. Such numbers have not yet been reported for NW Africa, and emphasize the strikingly different environmental conditions during HSs. This suggests that deflation rate and areal extent of HSs dust sources were much larger due to widely and rapidly retreating vegetation covers.

3.1 Introduction

Climate reconstructions of arid and humid conditions during the geological past can be obtained by investigation of sedimentary proxy records. Variations in Quaternary terrigenous element ratios and grain-size distributions of NW African margin sediments have been linked to changes in fluvial and aeolian inputs, which are in turn associated with fluctuations of continental humidity (Schneider et al. 1997; Zabel et al. 2001) and wind strength (Koopmann 1981; Sarnthein et al. 1981; Matthewson et al. 1995; Holz et al. 2007). Palynological analyzes of vegetation types (Bouimetarhan et al. 2009) and the isotopic composition of plant waxes in marine sediments (Schefuß et al. 2005; Castaneda et al. 2009; Niedermeyer et al. 2010; Collins et al. 2011) have been used to reconstruct past vegetation distributions.

On glacial-interglacial time scales, climatic conditions in NW Africa changed significantly. Reconstructions from marine sediment cores (Sarnthein et al. 1981; Balsam et al. 1995; Matthewson et al. 1995; Kohfeld and Harrison 2001; Larrasoaña et al. 2003) supported by numerical modeling (Mahowald et al. 1999; Mahowald et al. 2006) indicate that the dust input to the North Atlantic Ocean was substantially higher during the Last Glacial Maximum (LGM) compared to recent times. This finding was linked to higher wind speeds (Sarnthein et al. 1981; Matthewson et al. 1995; Ruddiman 1997) and enhanced deflation due to reduced vegetation cover (Ma-

howald et al. 1999). Marine pollen distribution patterns indicate that wind strength was intensified during late Quaternary cold stages. Especially during the LGM, trade winds were blowing in a more southerly direction than at present (Hooghiemstra et al. 2006 and references therein). Also, paleohydrological proxy data indicate arid conditions on the continent during the LGM (Gasse 2000; Gasse 2001; Gasse 2006 and references therein).

Large North Atlantic freshwater releases during Heinrich Stadials (HS) induced a slow-down of the meridional overturning circulation causing a short-term southward displacement of the Inter Tropical Convergence Zone (ITCZ) and an associated contraction of the African rain belt (Mulitza et al. 2008; Itambi et al. 2009; Collins et al. 2011). This resulted in more arid conditions in Northern Africa, in particular in the modern Sahel Belt, and intensified zonal winds at the level of the African Easterly Jet (AEJ) (Mulitza et al. 2008).

Episodic phases of humid conditions occurred in the Sahara during the Late Pleistocene and the early Holocene resulting in rich vegetation cover (Sarnthein 1978; Cohmap 1988; deMenocal et al. 2000a; deMenocal et al. 2000b; Castaneda et al. 2009). The latest of these so-called African Humid Periods (AHP) lasted from 14.8 ka to about 5.5 ka and was only interrupted by the Younger Dryas stadial at ~12 ka (deMenocal

et al. 2000a).

While the timing, scale, and causes of these massive climate changes in NW Africa are meanwhile well established, it is still difficult to estimate related changes in dust flux and river runoff during the highly contrasting climate periods of the past 80 kyrs. The transport pathways, fractionation processes, and post-depositional alterations must be understood as they all may significantly modify the fingerprint of the source. It is best practice to compare and cross-validate proxy-based terrigenous flux reconstructions from several, not intrinsically correlated parameters.

In this study we investigate core material retrieved from the W African continental margin in the corridor between the present ITCZ summer and winter positions (Fig. 3-1). Because of the location of the studied core, we expect that the terrigenous material is supplied predominantly by the Gambia River and the prevailing wind systems (NE Trades, AEJ). Grain-size, geochemical and rock-magnetic data have been combined because they reflect transport and source characteristics from different perspectives and can be obtained by rapid, automated measurements.

We introduce an innovative multivariate strategy combining single parameter end-member (EM) analysis and least-squares fitting to determine associated multi-proxy EM characteristics. This approach enables a cross-validation and joint interpretation of the EM systems. Based on the multi-proxy characteristics, we

assess the influence of transport, environmental change, and source area variability on the different EM properties. Our approach allows us to calculate mass accumulation rates of fluvial and aeolian sediments at our study site and therefore provides a high-resolution record of past terrigenous flux changes.

3.1.1 Materials

Gravity core GeoB 13602-1 (13°32.71' N; 17°50.96'W) was retrieved during RV *Maria S. Merian* Cruise MSM 11/2 in 2009 from the continental slope off Gambia in a water depth of 2,395 m (Fig. 3-1). In this area the westward deflected surface Canary Current converges with the North Equatorial Counter Current (NECC, Fig. 3-1). The northward flowing South Atlantic Central Water extends between 300-600 m water depth; at deeper levels southward flowing North Atlantic Deep Water is present (Tomczak 2003).

The 8.75 m long sediment core consists of hemipelagic dark olive clays and silts; a significant change to reddish brownish colors is observed in the depth interval 2.00-2.85 m. The sediment is undisturbed except for a small scale distal turbidite at 3.90-4.00 m depth. Gravity core GeoB 13602-1 was sampled at 5 cm intervals. All samples were freeze-dried before analysis. An age model for this core was developed by Just et al. (Chapt. 2) and is based on correlation of the oxygen isotope record of epibenthic *Cibicides wuellerstorfi* to that of MD 95-2042 (Shackleton et al. 2000) and five radiocarbon ages (c.f., Just

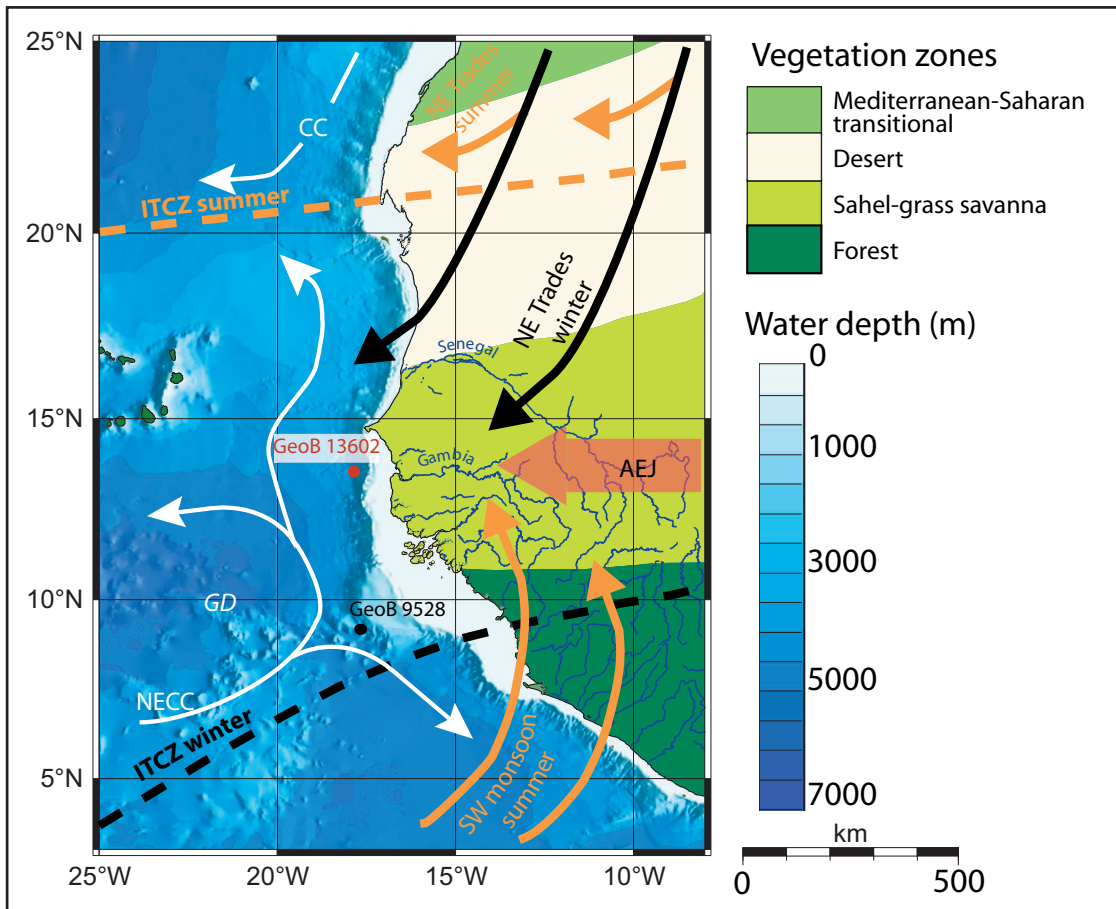


Fig. 3-1: Vegetation belts on the NW African continent (modified after White 1983). Oceanic surface circulation (white arrows) is controlled by the North Equator Counter Current (*NECC*) and associated anticyclonic circulation around the Guinea Dome (*GD*) and by the Canary Current (*CC*). Orange and black arrows indicate atmospheric features during summer and winter, respectively. Gravity core GeoB 13602-1 (studied here) is depicted in red and GeoB 9528-3 (Castaneda et al. 2009) in black.

et al. Chapt. 2, Fig. 2-2 and Table 2-1). For the age-model construction the depth interval of the turbidite was excluded. GeoB 13602-1 spans the last 77 ka and thus Marine Isotope Stages (MIS) 1 through 4 and the end of MIS 5. The averaged sedimentation rate is $\sim 11 \text{ cm kyr}^{-1}$ and, accordingly, sampling at 5 cm intervals corresponds to a mean resolution of 450 years and permits the resolution of millennial scale climatic variations such as HSs.

3.1.2 Source areas and transport of terrigenous material

Two main source areas for the mobilization of aeolian dust from N Africa have been identified: The Bodélé Depression in Chad, which represents at present the most productive dust source in the world (Prospero et al. 2002), and an area in northern Mali and Mauretania where the emission is less intense but the area is much larger than the Bodélé Depression (Engelstaedter et al. 2006).

Due to dry and deep atmospheric convection, which initiates near-surface turbulence, soil par-

ticles are suspended (Engelstaedter et al. 2006), uplifted by vertical convection and transported westwards within the Saharan Air Layer by the AEJ (e.g. Pye 1987). Further, coarse dust is transported to the Atlantic Ocean by NE trade winds mainly during winter (e.g. Sarnthein et al. 1981; Prospero 1996). The relative contributions of these two pathways are still a matter of debate.

The Gambia River originates in Eastern Senegal and has only a few small tributaries. It flows in a westerly direction through Senegal and Gambia to the Atlantic Ocean. The drainage basin comprises an area of 78,000 km² and is dominated by savanna vegetation types (Lesack et al. 1984, cf., Fig. 3-1). With respect to other rivers in NW Africa, e.g. the Senegal River, whose drainage basin is 3.5 times wider and covers different vegetation zones, the fluvial discharge of the Gambia reflects regional changes in precipitation and mirrors the geology of the drainage basin and most importantly their pedogenic products.

Outcrops of the West African Shield consist of metamorphic schists, basic volcanics, sedimentary rocks, and granites. In the SE of the drainage area these formations are overlain by Paleozoic metamorphic schists and quartzites, sandstones and dolomites. Locally, dolerites and rhyolites are present. In the western part of the drainage area, Mesozoic to Tertiary sediments occur (Lesack et al. 1984 and references therein). In the northern part of the catchment, ferruginous soils with typical assemblages of kaolinitic and mi-

nor illitic clays with low organic matter occur. Further to the south, ferralitic soils are dominated by kaolinite and iron and aluminium oxides, with a high organic matter content (Lesack et al. 1984 and references therein).

A further component, which may contribute to the fluvial load, is material advected from farther south (e.g. Geba River in Guinea-Bissau). However, since the current velocities are moderate (Just et al. Chap. 2, Fig. 2-1 b), it is reasonable to assume that such advected material makes only a minor contribution to the sediment reaching the study site.

3.2 Methods

3.2.1 Geochemistry

For geochemical analyses, 4-5 g of freeze dried sediment samples was homogenized. The elemental composition was measured by energy dispersive polarization X-ray fluorescence spectroscopy using a SPECTRO XEPOS instrument (Wien et al. 2005). Quality control was assessed by repeated measurements of standard reference material MAG-1 (Govindaraju 1994). For a complete description see Mulitza et al. (2008).

3.2.2 Grain-size analysis

To analyze the grain-size distribution of the lithic fraction, the biogenic compounds were removed from the sediment. Organic matter was removed by boiling 0.5 g of bulk sediment with H₂O₂ (35%). Afterwards, the sample was boiled with HCl (10%) and demineralized water to re-

move CaCO_3 . The amount of opal is relatively low (1-5 weight %, data not shown) and was not dissolved. After the above procedure, the approximate terrigenous fraction is obtained. The grain-size distribution was measured using a Beckman Coulter laser particle sizer LS200 in 92 logarithmically-spaced size classes ranging from 0.39 to 2000 μm . Grains coarser than 133 μm were not detected. For the later end-member unmixing and visualization the 64 fractions from 0.39 to 133 μm were pooled into 32 size classes to smooth the data.

3.2.3 Dry bulk density and mass accumulation rates

To determine the dry bulk density and estimate the mass fraction of terrigenous sediments, 10 cm^3 of sediment were freeze-dried and weighed. Mass accumulation rates (ARs) are calculated by multiplication of dry bulk density and sedimentation rate. The terrigenous ARs were calculated by subtracting the biogenic (carbonate) contents (c_{BIO} , data from Just et al. Chap. 2).

$$m_{\text{TER}} = m_{\text{TOT}} * (1 - c_{\text{BIO}}) \quad (3-1)$$

3.2.4 End-member analysis

Downcore measurements of element concentrations, grain-size distributions, and IRM acquisition curves (adopted from Just et al. Chap. 2) which reflect mixtures of different source materials were unraveled using EM unmixing. The employed algorithm was developed by Heslop and Dillon (2007) based on an approach similar

to that of Weltje (1997). Under the assumption of linear mixing, such an EM mixing system can be written in matrix notation as:

$$X = AS + E \quad (3-2)$$

where X represents the n -by- m data matrix of n samples (one per row) and m variables (e.g., grain-size classes, relative element abundances) in the columns. Matrix A (n by l) denotes the abundance of l EMs (one per column) for each sample (one per in row). Matrix S represents the m properties of the l EMs, and E is the error matrix of residuals. Because the contributions of each EM have to be positive and the variables (e.g., grain-size classes, elemental abundances) of each EM must add up to ones, non-negativity constraints ($A \geq 0$; $S \geq 0$) and a sum-to-one constraint for the rows in S are included in the unmixing algorithm.

Residuals may include instrumental noise, compositional variations of the individual sources and non-identified additional sources that were not detected due to low or only brief activity. Before performing the unmixing, low-rank representations and their coefficients of determination (R^2) with the input data are calculated by principal component analysis (PCA). The decision on the number of EMs to include in the final mixing model is a compromise between keeping the number of components low whilst maintaining a reasonably good approximation of the input data. Additionally, the number of EMs should also be reasonable in the geological context of the study (Weltje 1997; Weltje

and Prins 2007). For a more detailed description about the mathematical approach of the algorithm we refer the reader to Weltje (1997) and Heslop and Dillon (2007).

For performing the EM unmixing of the geochemical data set, the mass concentrations of the most abundant ‘terrigenous’ elements Mg, Al, Si, K, Ti, Fe were normalized to a sum of 1.

Since we are only interested in the terrigenous fraction, Ca is excluded in the analysis as it is highly correlated with the biogenic fraction.

3.3 Results

3.3.1 Geochemistry

Three different element ratios (Al/Si, Ti/Fe, Fe/K) are used to characterize the downcore variations in chemical composition (Fig. 3-2) since they are typically different for aeolian fluvial material off NW Africa (Table 3-1). Generally, the glacial stages MIS 2 and MIS 4 have lower Al/Si and Fe/K and slightly elevated Ti/Fe ratios, with respect to MIS 1 and 3. The MIS 4/3 and MIS 2/1 transitions are sharp, while the MIS 3/2 transition lacks a significant shift. Al/Si and Fe/K rather gradually decrease from the beginning of MIS 3 until MIS 2.

Remarkably low values mark HS 5, 4 and 2 in the Fe/K and Al/Si records. Ti/Fe shows significant peaks only during HS 2 and 4. HS 1 is characterized by the most extreme values in all reported element ratios. Notably, Al/Si and Fe/K show a more gradual decrease than Ti/Fe, which in contrast is marked by a sharp increase at the beginning of HS 1. Furthermore, all ele-

ment ratios show a characteristic double peak and trough, respectively. The YD is expressed by lower Al/Si and Fe/K and slightly elevated Ti/Fe ratios. A drop in Fe/K occurs at the end of the AHP around 6 ka.

3.3.2 Grain-size distribution

Since off NW Africa the grain-sizes of fluvial material are finer compared to aeolian dust (Koopmann 1981), coarsening and fining grain sizes correspond to increasing proportions of aeolian and fluvial material, respectively.

Generally, a bimodal grain-size distribution prevails throughout the record (Fig. 3-3). One fraction spans grain-size classes from 2 to 20 μm , the other one comprises coarser grain sizes between 25 and 90 μm . During late MIS 5 sediments are relatively uniform and fine, while from MIS 4 to MIS 1 two modes are distinct. During MIS 3 and MIS 1 the distribution is dominated by the finer grain-size classes while MIS 2 has coarser fractions. In the Holocene, the coarse fraction is entirely missing, and sediments are mostly finer than 9 μm . Intervals of significant coarse modes correspond to HS 5, HS 4, HS 2, the LGM and HS 1.

3.3.3 Differences and similarities in proxy records

The general patterns in all proxy records correspond to environmental changes of dry and humid conditions, i.e., high contribution of aeolian and fluvial material (c.f., Table 3-1), which have also been reported from tropical Africa (e.g., Matthewson et al. 1995). The most strik-

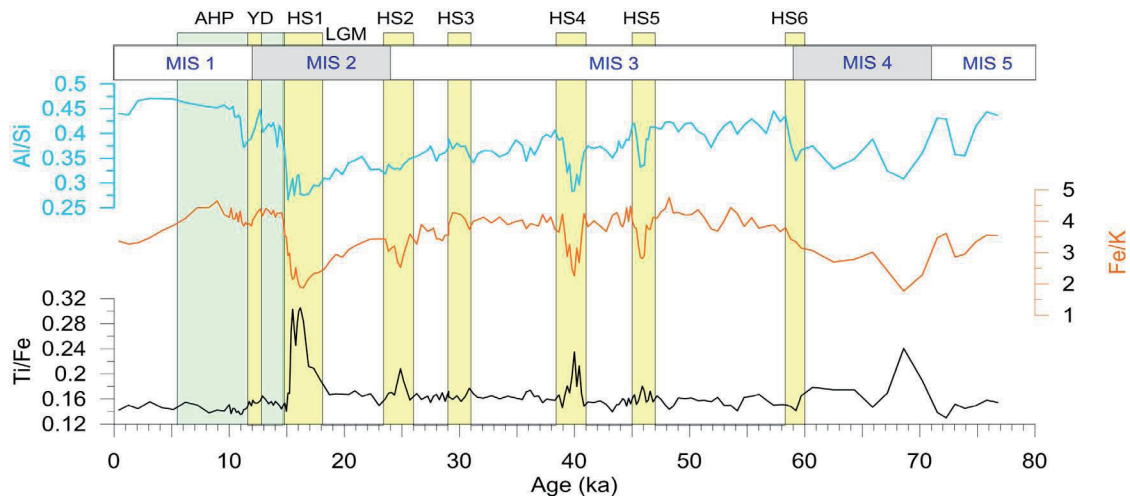


Fig. 3-2: Elemental ratios of GeoB 13602-1. Minima in Al/Si and Fe/K ratios and maxima in Ti/Fe ratios correspond to dry conditions on the African continent. MIS: Marine Isotope Stage, HS: Heinrich Stadial (after Sarnthein et al., 2001), YD: Younger Dryas, AHP: African Humid Period.

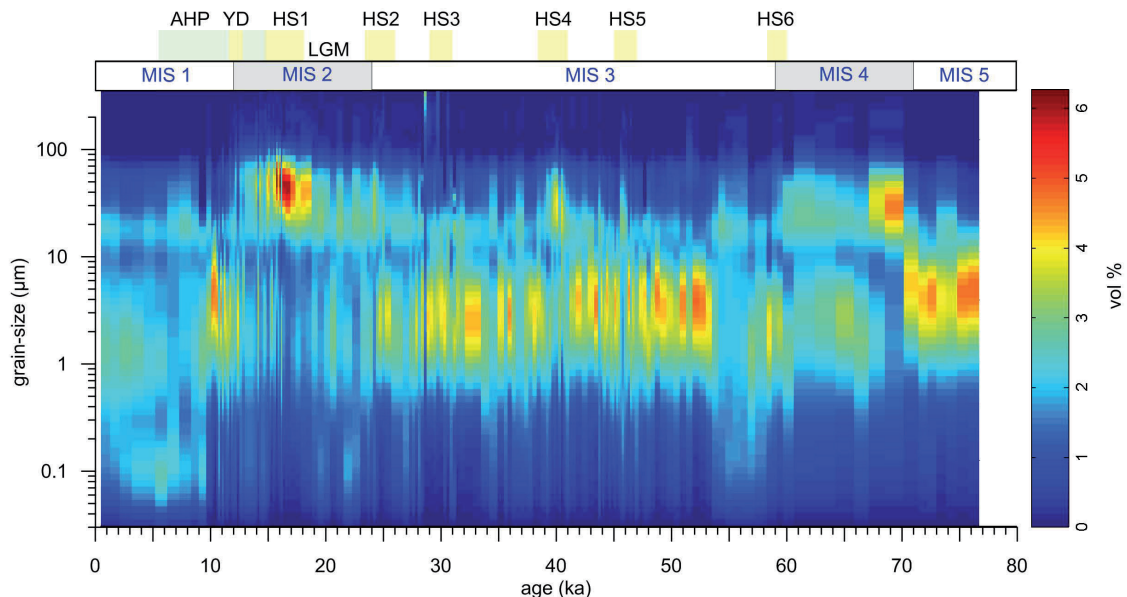


Fig. 3-3: Grain-size data of GeoB 13602-1. Two modes of grain sizes are apparent. The fine mode corresponds to grains of $<10 \mu\text{m}$; the coarser mode is composed of grains in the range of $20\text{--}70 \mu\text{m}$. During dry periods, in MIS 2 and the HSs, the sediments are coarser. For abbreviations see Fig. 3-2.

ing features in all parameter sets are the peaks that occur during HSs. These features support the hypothesis that these cold periods in the N Atlantic correspond to dry conditions and stronger winds over NW Africa (Jullien et al. 2007; Mulitza et al. 2008; Itambi et al. 2009). These climatic changes are inferred from decreasing Al/Si and Fe/K ratios and a coarsening of the physical grain size. Additionally, in GeoB

13602-1 the Ti/Fe ratio appears to be a significant indicator of higher aeolian input since Ti is enriched in coarse sediments (Boyle 1983; Zabel et al. 1999). However, the drying trend deduced from decreasing Al/Si during MIS 3 and especially during the LGM is not expressed in the grain-size data. On the other hand, drier conditions during HS 1 are indicated by extremes in Fe/K, Ti/Fe, and a coarser physical grain size.

The double-peak of the element ratios is not clearly expressed in the grain-size data. During MIS 1, the decrease in Fe/K corresponds to a fining in the physical grain sizes.

3.4 End-member unmixing

Contrasting patterns in the proxy records emphasize that factors influencing sediment elemental composition and grain size are diverse. By joint analyzes more information about these factors can be gained. We suggest that both source area variability and changes in transport processes are reflected in these contrasting patterns. To evaluate the relationships further we apply an EM unmixing approach to the different parameter sets. The EM unmixing results of the grain-size and elemental data will be presented in this study, while the EM analysis of IRM acquisition curves (see Fig. 3-5) is reported on by Just et al. (Chap. 2, Fig. 2-4), see also Fig. 3-5e).

In this study, the magnetic EM contributions are rescaled to the intensity of remanent magnetization and thus roughly indicate differing the magnetic mineral concentrations within each EM.

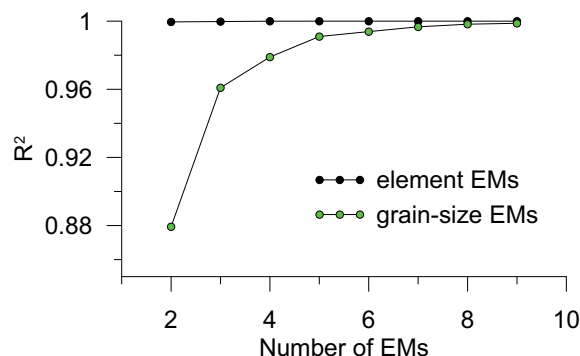


Fig. 3-4: Coefficients of determination (R^2) obtained by principal component analyses as a decision criterion for the number of end-members used for the unmixing approach of the element and grain-size data.

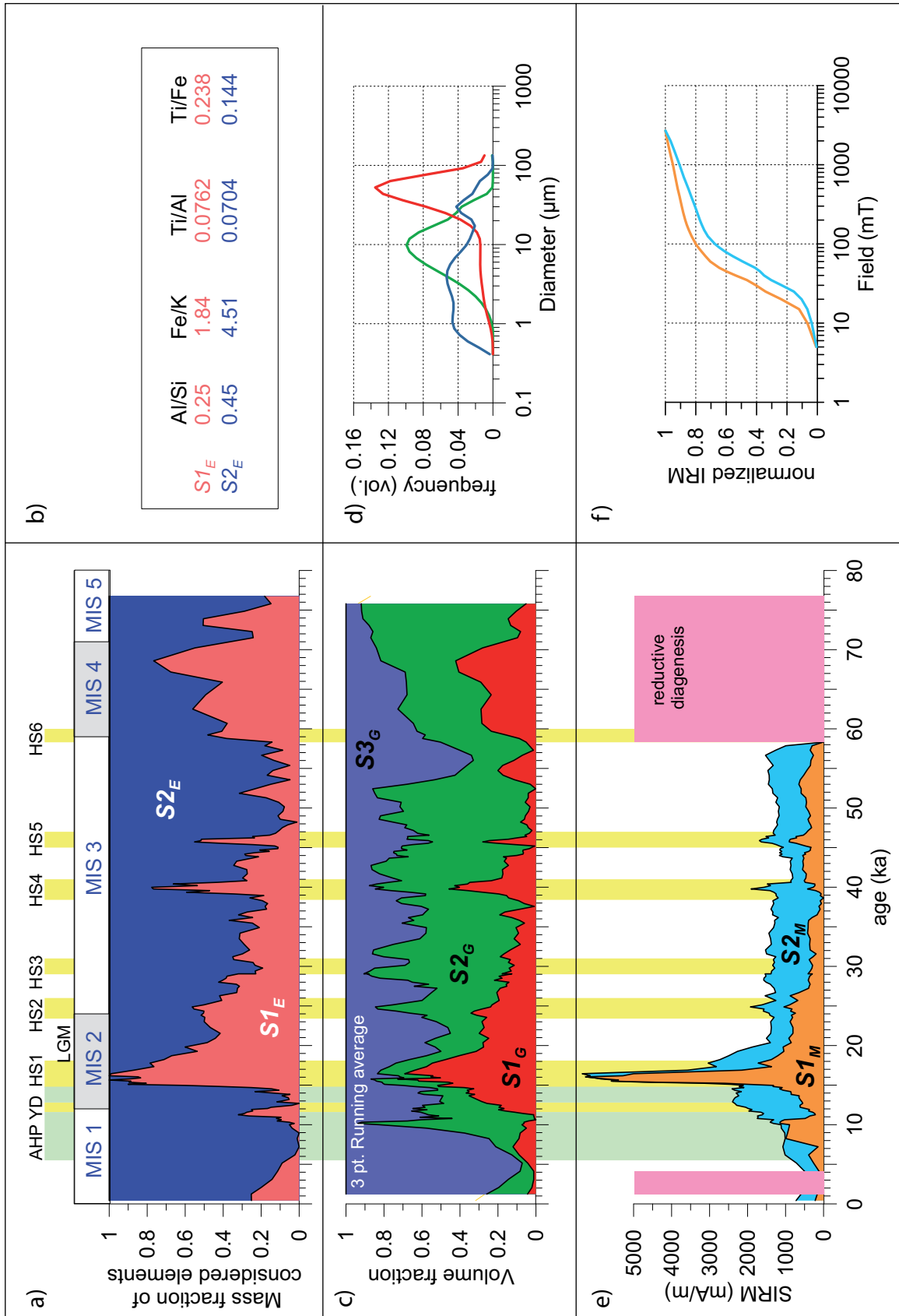
3.4.1 Element end-members

The element EM analysis shows an excellent fit ($R^2 = 0.99$ from the PCA, Fig. 3-4) with only two EMs ($S1_E$ and $S2_E$). Their relative element contents were transformed into elemental ratios (Table 3-2a and Fig. 3-5b). The elemental ratios of $S1_E$ and $S2_E$ resemble present-day dust and suspension load samples of the Senegal River (Table 3-1).

The end of MIS 5, and MIS 3 and 1 are dominated by $S2_E$ (Fig. 3-5a), while MIS 4 and 2 are dominated by $S1_E$. A gradual increase of $S1_E$ contribution is apparent throughout MIS 3 until MIS 2.

Sample	Al/Si	Fe/K	Ti/Fe	Reference
Dust Cap Verdes (Sal Island)	0.49	2.82		Chiapello et al. 1997
	0.45	2.31		
	0.43	2.09		
HAR (aeolian deposit)	0.21	2.71	0.17	Moreno et al. 2006
MON (aeolian deposit)	0.19	3.10	0.27	
Senegal	0.54	4.77	0.08	Gac & Kane 1986

Table 3-1: Elemental ratios of dust and fluvial material off NW Africa. The abbreviations correspond to aeolian deposits in SW Niger by north easterly winter Harmattan (HAR) and south westerly summer monsoon (MON) winds.



Occasional increases in SI_E coincide to HSs and the Younger Dryas, of which HS 1 is the most pronounced. The double-peak formerly observed in the downcore element ratios, is present, but less well expressed in the EM contributions.

3.4.2 Grain-size end-members

For the EM analysis of the grain-size data, a three EM solution appears to be optimal ($r^2 = 0.96$, Fig. 3-4). End-members are referred to as SI_G , $S2_G$, and $S3_G$ (Fig. 3-5c, d). SI_G and $S2_G$ have clear unimodal distributions, with modes of 10 and 40 μm , respectively, while $S2_G$ has a broad distribution (1-4 μm) and small peak around 20 μm .

The inclusion of an additional EM would split the medium grained $S2_G$ (10 μm), into two EMs with higher (14 μm) and lower (6 μm) modes with co-varying contributions (data not shown). Typically, aeolian material is coarser than fluvial material off NW Africa (Koopmann 1981). This hints to aeolian and fluvial transport for the coarse SI_G and fine $S3_G$, respectively. The transport pathway of $S2_G$, however, cannot be inferred at this point.

Generally, $S2_G$ and $S3_G$ are anticorrelated, with a higher contribution of $S2_G$ except during the LGM and the late Holocene. The contribution of SI_G is generally low; however an increasing abundance from 50 ka until HS 1 is observed. Peaks in SI_G occur during HS 5, 4, 2 and 1. HS 1 is associated with a very high contributions of SI_G , forming a double-peak.

3.4.3 Comparison of the end-member models

The comparison of the abundances of the individual EM unmixing reveals that SI_G , SI_E , and SI_M peak during HSs. This pattern is most clearly expressed for the element and grain-size EM mixing systems, while SI_M only peaks during HS 4, the LGM and HS 1. This co-variation is in line with the inferred aeolian nature of SI_G and SI_E suggested by the grain-size distribution and elemental ratios, respectively, and the interpretation for SI_M of Just et al (Chap. 2).

3.5 Multi-proxy approach

The modeled abundances of the EMs estimate the mixing proportions with respect to the input data: Grain-size EMs correspond to volume fractions, element EMs relate to mass fractions

Fig. 3-5: End-member models of the element, grain-size and rock-magnetic data. (a) Cumulative downcore contribution of element EMs (S_E). (b) Elemental ratios calculated based on the elemental composition of the EMs (cf., Table 3-2). SI_E resembles dust samples and aeolian deposits, while the $S2_E$ is similar to fluvial suspension from the Senegal River (cf., Table 3-1), which flows north of our study area. (c) Cumulative downcore contribution of grain-size EMs S_G . (d) SI_G corresponds to a coarse sediment fraction, which is indicative for dust exported to the Atlantic Ocean, while the fluvial $S2_G$ and $S3_G$ are much finer. (e) Cumulative downcore contributions of the aeolian and fluvial magnetic S_M s (Just et al. Chap. 2). Their EM B and EM D are not plotted. The pink areas indicate intervals of reductive diagenesis. We show here the contributions with respect to the IRM intensities which reveals that the intensity of SI_M (EM A of Just et al., Chap. 2) is much higher than $S2_M$ (their EM F). (f) The IRM acquisition curves are indicative of the magnetic mineralogy of the fluvial and aeolian rock-magnetic EMs. Aeolian SI_M has a higher magnetite concentration and a higher hematite/goethite ratio (Just et al. Chap. 2).

with regard to the total mass of the elements considered and rock magnetic EMs relate to proportion of saturation isothermal remanent magnetization (SIRM, Just et al. Chap. 2, Fig. 2-4). The relation of rock-magnetic EM abundances is proportional to volume or mass concentrations of the bulk terrigenous fraction they represent. However, recalibrations are needed to transfer the IRM intensity into volume and mass percentages of the respective terrigenous fractions they are associated with. Calibration factors depend on the concentration of magnetic minerals within a certain volume of bulk material and on the magnetic inventory, since magnetic minerals have different SIRMs (Peters and Dekkers 2003).

The grain-size EM analysis indicates that three energetic regimes exist for the transport of terrigenous sediments. Based on the hypothesis that the properties of different kinds of proxies are associated to each other, i.e. a grain-size class, which is transported by a certain mechanism, mirrors the geochemistry and the magnetic mineralogy of the soils in the source area or experiences similar gravitational sorting processes, we developed a new approach for a multi-proxy validation of the EMs. We use grain-size EM abundances A_G to predict geochemical, P_E , and rock magnetic properties, P_M that are associated to the grain-size EM properties S_G . The assumption underlying this approach is that

$$X_E = A_G P_E + R = \hat{X}_E + R \quad (3-3)$$

and

$$X_M = A_G P_M + R = \hat{X}_E + R \quad (3-4)$$

are equivalent EM mixing formulations of equation (3-2).

Since there is only one unknown, this linear problem can be solved using non-negative least-squares fitting (NNLSQ, Löfberg 2004), which respects the constraint ($P \geq 0$). Since the element abundances are scaled to a sum of 1, the element abundances of P_E must also add up to 1 and a respective constraint is included.

In order to apply this approach to the IRM data, some pre-processing had to be performed. Since it was previously shown that one of the magnetic EMs corresponds to biogenic magnetite (Just et al. Chap. 2) which is formed *in situ*, and hence, is not representing any terrigenous fraction, we subtracted the contribution of this EM from the initial data (Fig. 3-6). We also excluded the top interval and the lower part of the core where substantial reductive diagenesis has modified the magnetic mineralogy (Just et al. Chap. 2). After the pre-processing the residual IRM acquisition curves should only represent the terrigenous magnetic inventory. IRM was measured on the bulk sediment, which consists of terrigenous and biogenic material (mainly carbonate), which does not have an IRM. In contrast, grain-size data were analyzed on a carbonate-free basis by dissolving the carbonate in advance of the grain-size analyzes. To predict IRM acquisition curves from the volumetric mixing proportions of the grain-size EMs, their proportions must be corrected for the volume of carbonate A_C (Fig. 3-6). This is equivalent to a recalculation of IRM on a carbonate-free basis

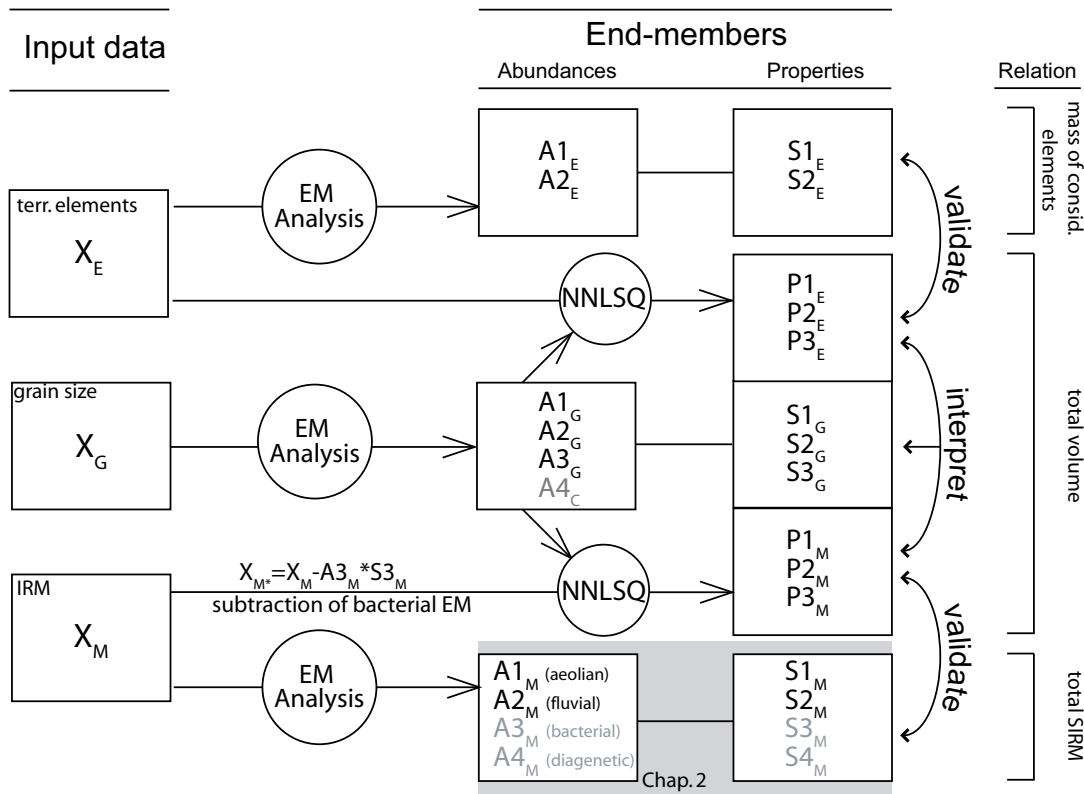


Fig. 3-6: Schematic overview of the multi-proxy EM approach. Each individual data set was unmixed using the approach developed by Heslop and Dillon (2008). The algorithm outputs the downcore contributions A of the computed EMs and their properties S . The grain-size EM contributions A_G were successively used to calculate associated geochemical P_E and rock-magnetic properties P_M for the grain-size EMs. The so obtained P_E and P_M have the same contributions as the S_G . The comparison of S_M and P_M and S_E and P_E may be used to verify, whether changes in grain-size EM contributions A_G correspond to changes of the magnetic mineralogy and elemental composition (see Fig. 3-7 and Table 3-2). The volume fraction of the terrigenous material was reduced by the volume of biogenic material A_C . To apply the approach to the magnetic data, the contribution of the bacterial magnetite identified by Just et al. (Chapt. 2) was subtracted from the total IRM. The joint examination of the multi-proxy properties (P) enables the interpretation of the EMs. NNLSQ: non-negative least square fitting.

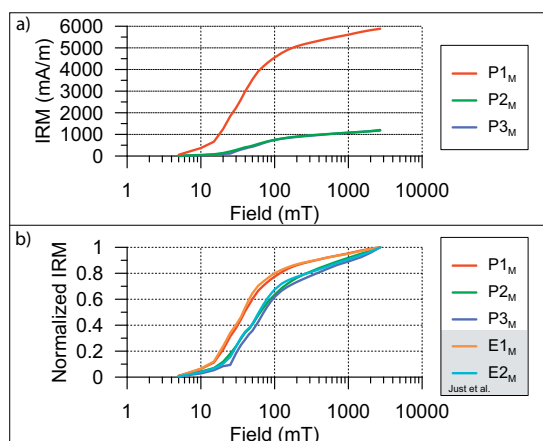


Fig. 3-7: (a) IRM acquisition curves of P_M obtained by the least-square fitting approach. $P1_M$ has a much higher amplitude than $P2_M$ and $P3_M$, pointing to a higher content of magnetic minerals within this terrigenous EM. (b) normalized IRM curves P_M in comparison to S_M obtained by unmixing the IRM data (Just et al. Chap. 2). The strong similarity indicates a good correlation between $P1_M$ and $S1_M$ (their EM A) and $P2_M$ and $P3_M$ and $S2_M$ (their EM F).

Table 3-2: (a) Calculated element composition and element ratios of EMs S_E and (b) predicted associated properties P_E of the grain-size end-members.

		Al	Si	K	Ti	Fe	Mg	Al/Si	Fe/K	Ti/Al	Ti/Fe
a)	$S1_E$	0.174	0.700	0.030	0.013	0.056	0.027	0.249	1.843	0.076	0.238
	$S2_E$	0.249	0.554	0.027	0.018	0.122	0.030	0.450	4.506	0.070	0.144
b)	$P1_E$	0.170	0.728	0.027	0.013	0.041	0.021	0.233	1.542	0.074	0.306
	$P2_E$	0.230	0.586	0.028	0.017	0.110	0.029	0.392	3.935	0.074	0.154
	$P3_E$	0.250	0.552	0.028	0.017	0.119	0.033	0.453	4.229	0.068	0.143

for each of the EMs.

To assess the quality of the multi-proxy model, the correlation between the input data, \mathbf{X} , and the estimates, $\hat{\mathbf{X}}$, derived by NNLSQ was calculated. In the case of the IRM data set, which is un-normalized and thus free of a sum-to-one constraint, the Pearson product-moment correlation coefficient was calculated. For the compositional data set of element relative abundances we performed the centered-log-ratio transformation (Aitchison 1982) to bring the data \mathbf{X}_E and estimates $\hat{\mathbf{X}}_E$ into real space. Afterwards a correlation coefficient analogous to the Pearson product-moment correlation coefficient for compositional data was calculated. In both cases the significance of the correlation was assessed using a *Monte Carlo* randomization test with 10^4 iterations.

3.5.1 Multi-proxy properties

The elemental ratios \mathbf{P}_E associated to the grain-size EMs can be found in Table 3-2 b. A striking feature is that the associated elemental composition of the coarse grain-size EM $\mathbf{P1}_E$ is distinctly different from $\mathbf{P2}_E$ and $\mathbf{P3}_E$. $\mathbf{P1}_E$ has low Al/Si and Fe/K ratios and high Ti/Fe ratio. On the other hand, both fine-grained EMs are associated to high Al/Si and Fe/K and low Ti/Fe ratios.

Likewise, the IRM acquisition curve of $\mathbf{P1}_M$ is distinctively different from $\mathbf{P2}_M$ and $\mathbf{P3}_M$ (Fig. 3-7), while the latter curves are very similar. To compare the shape of the curves, which is indicative of the magnetic mineralogy, we normalized them to one (Fig. 3-7b). Again, the shape

of $\mathbf{P1}_M$ is distinctively different; the slope starts to rise at lower fields and is flatter at high fields compared to $\mathbf{P1}_M$ and $\mathbf{P2}_M$.

The comparison of the associated properties with the EMs obtained by unmixing of the magnetic and geochemical data reveals large similarities (Fig. 3-7b, Table 3-2). For $\hat{\mathbf{X}}_M$ and \mathbf{X}_M the coefficient of determination is 0.51 (corresponding to a significance level of <0.0001). When comparing \mathbf{X}_E and $\hat{\mathbf{X}}_E$ the calculated squared correlation is 0.63 (significant at a level of <0.0001).

3.6 Discussion

3.6.1 Multi-proxy characteristics of terrigenous end-members

Since the multi-proxy properties of the grain-size EMs appear to provide a good representation of the EMs of the individual analysis, we can elucidate the nature of the grain-size EMs by considering their associated multi-parameter properties. The coarse mode of $\mathbf{S1}_G$ is in the range of typical grain sizes (8-42 μm) for dust collected off NW Africa (Stuut et al. 2005). The associated geochemical properties $\mathbf{P1}_E$ are similar to present-day dust samples (Table 3-1) collected at Sal Island (Chiapello et al. 1997) and aeolian deposits in SW Niger (Moreno et al. 2006). Therefore, we interpret that $\mathbf{S1}_G$ corresponds to aeolian material. Further, the normalized IRM acquisition curve $\mathbf{P1}_M$ resembles the IRM acquisition curve of $\mathbf{S1}_M$ which has been identified as an aeolian EM (Just et al. Chap. 2) with a magnetic inventory containing a high

concentration of magnetite and a high hematite/goethite ratio.

The medium and fine grained EMs have similar elemental compositions and magnetic mineralogies. The present-day suspension load at the mouth of the Gambia river consists of grains finer than 10 μm (Gac and Kane 1986 and references therein). Also the elemental ratios $P2_E$ and $P3_E$ resemble fluvial samples of the suspension load of the Senegal river (Gac and Kane 1986, Table 3-1). Additionally, the IRM acquisition curves $P2_M$ and $P3_M$ are similar to $E2_M$ which was interpreted as a fluvial EM with a lower hematite/goethite ratio and a lower relative concentration of magnetite (Just et al. Chap. 2).

The similar elemental composition and magnetic mineralogy might indicate that both EMs correspond to sediments that originate from the same source area (i.e. Gambia River catchment), but are transported under different energetic conditions. Since the Gambia River drainage basin is relatively well vegetated, its potential for aeolian deflation of material is low. We therefore conclude that both the fine and medium grained EM correspond to a fluvial EM.

Only the joint characterization of the multiproxy properties enables the interpretation of the medium grained grain-size EM. The multiproxy approach reveals that one grain-size EM corresponds to aeolian material with coarse grain sizes and a distinct geochemical composition and magnetic mineralogy and two EMs having the same geochemical and magnetic properties but different grain-size distributions.

It appears that magnetic and geochemical data are more indicative for the source area of the sediments, while grain size is primarily controlled by transport conditions. The differences in the grain-size distribution of the fluvial EMs will be discussed in section 3.6.3.

3.6.2 Budgeting the accumulation of terrigenous end-members

We used the volumetric grain-size EM contributions to quantify the fluxes of terrigenous sediments to the continental margin off Gambia. Generally, MARs vary between 30 $\text{g m}^{-2} \text{yr}^{-1}$ and 700 $\text{g m}^{-2} \text{yr}^{-1}$ (Fig. 3-8). Note that in the lower part of the core (MIS 5 and 4) the mass accumulation rates are not reliable because most likely compression of the sediments may have occurred during gravity coring (Just et al. Chap. 2), leading to erroneous sedimentation rates. The accumulation of the fluvial EMs appears to be higher than that of the aeolian EM (with a few exceptions during HSs and the LGM). This is in accordance with the calculations of Collins et al. (2011) who investigated the dust/river ratio in sediment cores of a transect from 21° N to 23° S off W Africa. At 12° N, they found a dust/river proportion of ~ 0.3 in the Holocene and a ratio of ~ 1.2 and ~ 2.5 during the LGM and HS 1, respectively. Our analysis reveals that the increase of this ratio at our site is controlled by high dust fluxes, while the input of fluvial material remains relatively stable (within the accuracy of our age model). Thus, the reported dry conditions seem only to affect the source

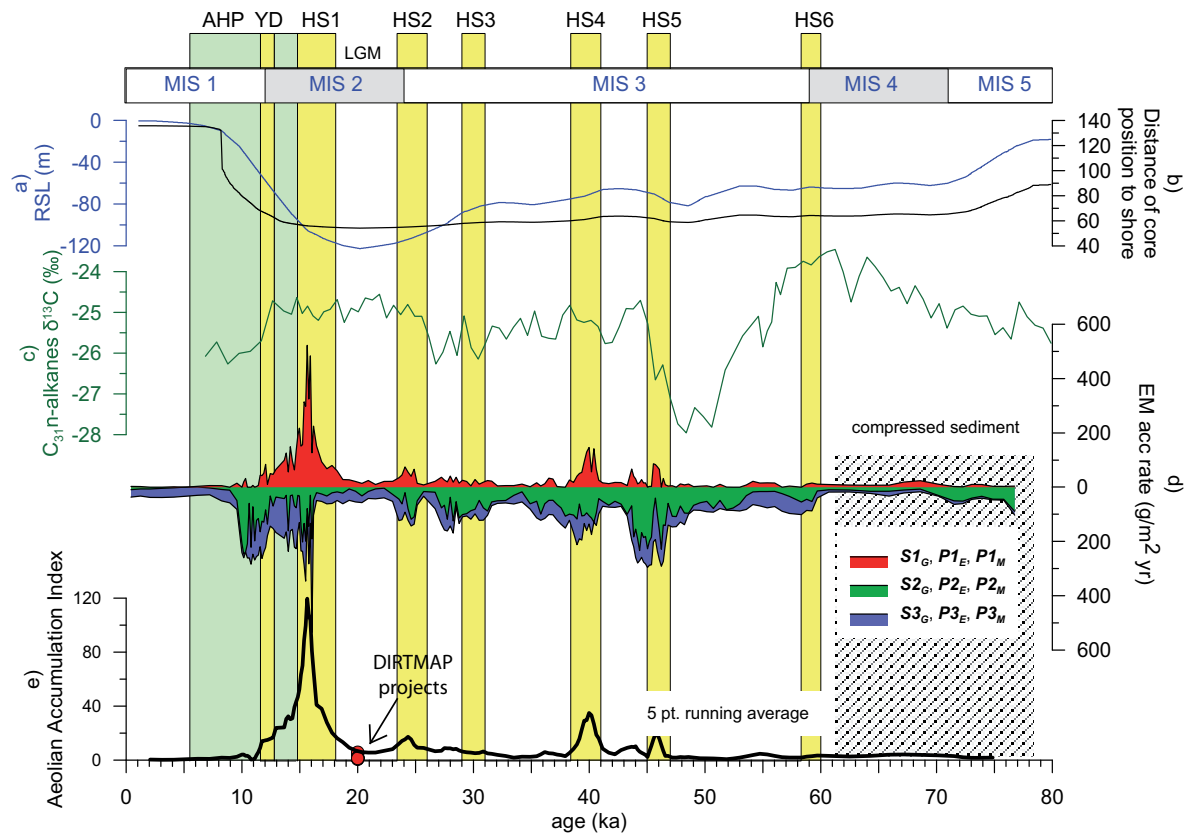


Fig. 3-8: (a) Relative sea-level (RSL) curve adopted from Waelbroeck et al. (2002) and (b) corresponding distance of the study site to the shoreline calculated based on the bathymetry of the shelf (extracted from GEBCO data). Once sea level fell below a threshold of 60 m, the site-to-shore distance remained relatively constant. (c) $\delta^{13}\text{C}$ of long chained *n*-alkanes of GeoB 9528-3 (Castaneda et al. 2009). Lower values correspond to phases with a higher proportion of C3 plants (trees) with respect to C4 plants (grasses). (d) Mass accumulation rates derived from the grain-size EM analysis. (e) The aeolian accumulation index (AAI) corresponds to the past dust accumulation in GeoB 13602-1 normalized to the Late Holocene dust accumulation at the respective site. Red points correspond to AAIs of the DIRTMAP project compilation (Kohfeld and Harrison 2001), see also Fig. 3-9.

areas of aeolian material (i.e., the areal extent) and have little influence on rainfall the Gambia River catchment and respectively the discharge of suspended material. However, this pattern could be an artifact of the age model because the short-term character of HSs and coinciding extremely high accumulation rates would require additional age determinations around the HSs.

Exceptionally high MARs during HS 1 show massive levels of aeolian input, The deglaciation until ~ 10 ka is marked by high accumulation rates of fluvial material in the range 100 to $300 \text{ g m}^{-2} \text{ yr}^{-1}$. Subsequently, MARs of the

fluvial EMs are reduced to $40 \text{ g m}^{-2} \text{ yr}^{-1}$ while the accumulation of aeolian material diminishes to less than $10 \text{ g m}^{-2} \text{ yr}^{-1}$. The accumulation of aeolian material during the Holocene is in good accordance with other studies in the region (Kohfeld and Harrison 2001) and estimates obtained by numerical modeling (Mahowald et al. 2006).

Difficulties arise when comparing absolute dust accumulation rates from different sites, since the deposition is influenced by regional conditions i.e., the presence of potential dust sources in the hinterland and the source-to-sink distance. To

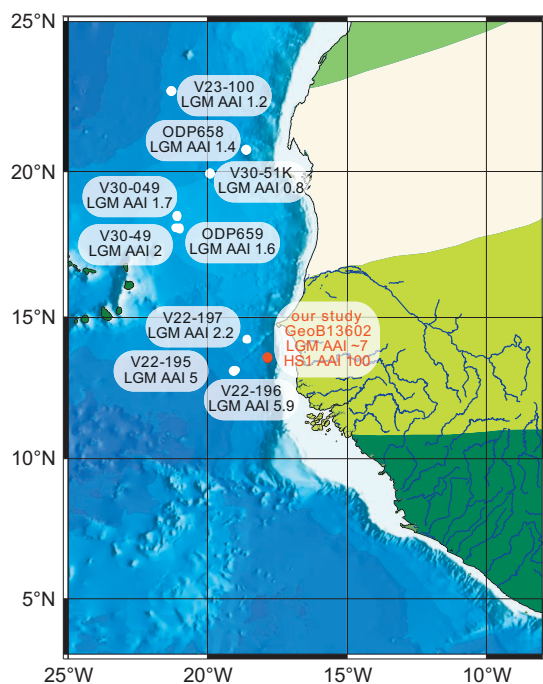


Fig. 3-9: Aeolian accumulation index (AAI) from different sites off NW Africa (Kohfeld and Harrison 2001). Data are only available for the LGM (Last Glacial Maximum). Note that AAI at our study site is in the same order as AAIs reported in the literature but is at least 10 times lower than the AAI for HS 1.

compare flux changes at different sites, it is useful to normalize the dust input to a site specific reference. The data compilation in the DIRTMAP project (Kohfeld and Harrison 2001) uses the modern dust accumulation at each site as a reference. Accordingly, we use the calculated dust accumulation of GeoB 13602-1 during the Late Holocene as a reference, and refer to the proportion of dust throughout our record and the Holocene as the aeolian accumulation index (AAI, Fig. 3-8e, Fig. 3-9). The averaged accumulation rates of aeolian material in GeoB 13602-1 during MIS 3 and the LGM correspond to AAIs of 3 and 7, respectively. The value for the LGM is in the order of the dust deposition in proximity of our study area during the LGM

obtained from numerical modeling (Mahowald et al. 2006). Studies in the DIRTMAP project (Kohfeld and Harrison 2001) report AAIs of 1.5-6 during the LGM (Fig. 3-8f, Fig. 3-9).

According to the GeoB 13602-1 record far higher dust fluxes (AAI 8-35) occur during HS 5, HS 4 and HS 2. The highest accumulation of aeolian materials occurs during HS 1 and is in the order of $400 \text{ g m}^{-2} \text{ yr}^{-1}$ (mean AAI 100). Note that this AAI is at least 10 times higher than during the LGM. This finding emphasizes that short-term disturbances of the meridional overturning circulation have a major impact also on low latitudes climate.

3.6.3 Source areas and transport processes

Fluvial material

Generally, two factors control the accumulation and the grain-size distribution of fluvial material: (1) the transport distance (i.e., the distance from the river mouth to the core location and thus the available accommodation space) and (2) the extent of the suspension fan. The latter is influenced by the transport energy and the water discharge, i.e., precipitation in the hinterland (Zabel et al. 2001). Additionally, varying current velocities in the ocean may lead to a displacement of the deposition zone of a certain grain-size class. Without detailed paleocurrent reconstructions, this latter effect is hard to quantify. Numerical modeling approaches indicate that the net NS horizontal volume transport in the

eastern Atlantic Ocean did not differ substantially during the LGM (Schäfer-Neth and Paul 2004). However, the stratification and depth of oceanographic boundary layers were different: a shallowing of northern sourced waters and ingression of SACW is evident (Sarnthein et al. 1994; Bickert and Mackensen 2004; Lynch-Stieglitz et al. 2007). To the best of our knowledge there are no regional paleocurrent reconstructions which integrate over the entire water column and could be indicative for a change in the deposition centre of suspended or advected material in our study area. Therefore we must assume that also on a regional scale, the integrated net transport of suspended material did not vary significantly during the last glacial and is essentially the same as today. In the following we focus on the effects of transport distance (i.e. distance from the core location to the study site) and transport energy.

Sea level during MIS 4 and MIS 3 was 60-80 m lower than today (Waelbroeck et al. 2002) and reached its lowest position and thus the shortest distance from the core location to the river mouth during MIS 2 (LGM, Fig. 3-8 a, b). However, due to the morphology of the flat-topped shelf, the core-to-shore distance remained relatively stable (55 km) once sea-level fall reached a threshold of ~60 m. A major transgression occurred during the deglaciation which ended at 8 ka, resulting in the present-day core-to-shore distance of ~140 km.

The sea-level curve and the related distance-to-shore curve, coincide roughly with the ac-

cumulation of fluvial material (Fig.3-8d), indicating that the distance from the river mouth to the study site plays an important role. However, the proportion of fine and coarse grained fluvial sediments especially during MIS 4, 3 and 2 cannot be explained by sea-level variations alone.

To consider the transport energy of the river, i.e. the water discharge, we investigate published studies focusing on proxies for precipitation on the continent. Castaneda et al. (2009) measured the $\delta^{13}\text{C}$ of long-chained *n*-alkanes on sediment core GeoB 9528-3 (09°09.96 N, 17°39.81 W, see Fig. 3-1). These plant waxes are contained in aeolian material whose source area is assumed to be at the Sahara-Sahel boundary (Castaneda et al. 2009). The variations in $\delta^{13}\text{C}$ can be regarded as a proxy for the relative proportions of C4 (grasses) and C3 plants (trees, shrubs), whose occurrence in NW Africa is dependent on humidity (Castaneda et al. 2009 and references therein). A relative increase in C4 vegetation during the end of MIS 5 and MIS 4 (Fig. 3-8c) indicates drying conditions while increasing humidity (relative increase of C3 plants) occurs at the beginning of MIS 3 (50-45) ka. Subsequently, the record indicates a higher proportion of C4 plants, which had the largest abundance during MIS 2. During the deglaciation until the Mid-Holocene, conditions were comparable to the early MIS 3. Similar patterns were observed in $\delta^{13}\text{C}$ of *n*-alkanes at a site to the north of our study area (Niedermeyer et al. 2010).

It can be hypothesized that during humid periods, and thus times of higher water discharge,

the fan of suspended material was more extensive and thus coarser particles were potentially transported out at sea, leading to a coarsening of the fluvial deposits and to lowering dust/river proportion.

The drying trend during MIS 5 and MIS 4 is expressed by a relative decrease in fluvial input with respect to the aeolian fraction. During MIS 3, the strong relative increase in C3 vegetation is roughly correlated to an increase of the coarse fluvial EM ($S2_c$). However, the prominent peak in C3 vegetation (around 50 ka) has no counterpart in the coarse fluvial EM. In the beginning of MIS 2, the fine fluvial EM ($S3_c$) re-established, which might point to lower water discharge of the Gambia River in line with drier conditions (increased C4 proportion, Castaneda et al. 2009) and modeling approaches (Van Meerbeeck et al. 2008). However, the total accumulation of fluvial material was reduced compared with MIS 3.

During the more humid last deglacial conditions the fraction of the coarse fluvial EM ($S2_c$) is again enhanced. During the AHP (deMenocal et al. 2000a) in the Mid-Holocene - which has also been ascribed the most humid period during the entire Holocene in sub-tropical and arid NW (deMenocal et al. 2000a; Collins et al. 2011; Meyer et al. 2011) - the fine fluvial EM is re-established, which seems to be contrary to the relationship outlined above. However, this period corresponds to a time of major sea-level rise, and thus the distance between core location and river mouth was increasing. This effect of sea-level rise is apparently more important than

the higher precipitation for suspended fluvial load.

We therefore interpret that the sea level has primary influence on the accumulation of fluvial material by controlling the distance from the shore to the site. However, once sea level fell below a threshold of approximately -60 m (dependent on the shelf morphology), the accumulation and the grain-size ranges of fluvial material are mainly influenced by precipitation in the hinterland.

Aeolian material

The accumulation of aeolian material is controlled by wind strength, frequency of the dust outbreaks, source-to-sink distance, and areal extent of dust sources. The latter is dependent on changes in vegetation cover in the hinterland, and thus precipitation. Widely exposed shelf areas may be subject to deflation and dry conditions and thus may act as additional sources, especially during times of low sea level. The high dust content during MIS 3, MIS 2 and particularly during HS 1 (Fig. 3-8d, e) indicates that environmental conditions at those times were different from present-day. Again, there is a rough correlation between vegetation in the hinterland and the proportion of aeolian material, especially at the MIS 3/2 transition, indicating that the expansion and contraction of the desert is the main driving mechanism for dust export from the continent. The rising sea level during the last deglaciation coincides with the decrease in dust contribution. This may point to the influence of exposed

shelves and regional dust sources during MIS 4 to MIS 2. For the LGM, further southward advancing dune fields (Maley 2000) could also represent additional dust sources. However, our approach reveals that the magnetic mineralogy and geochemical composition of the dust did not vary. It may therefore be inferred that regional remobilized sediments correspond to formerly aeolian deposits originating from the Sahara. Since the most extensive exposed shelves existed during the LGM, the exceptionally high dust accumulation during HS 1 cannot solely be attributed to this phenomenon and rather results from southerly expanded desert.

It has been suggested that during the LGM the Trades were much stronger compared to present day (Hooghiemstra et al. 2006 and references therein) and that also the zonal wind field (AEJ) was enhanced during Heinrich Stadials (Mulitza et al. 2008). This should have an effect on the accumulation of the aeolian fraction and on grain size. Since only one EM is resolved in our study, this inferred coarsening is not apparent in our EM unmixing. This rather suggests that dust events were more frequent (i.e. a longer 'dusty' season during HS 1) and point to a larger extent of dust sources. Likewise, Collins et al. (2011) inferred from vegetation proxies a shorter wet season for the LGM and HS 1. Because the grain-size distribution of the aeolian EM integrates over a certain grain-size range, it remains questionable, whether EM modeling is capable for detecting changes in wind strength, at least with the present input parameters. The

double peak observed in the proxy data and EM models indicate that during HS 1 environmental conditions may have changed rapidly. However, higher resolution records are needed to understand if such changes during HS 1 are associated to North Atlantic features, i.e. precursors of iceberg discharge in advance of Heinrich Events (e.g. Grousset et al. 2001; Jullien et al. 2007).

3.7 Conclusion

Our multi-proxy approach enabled us to find multi-parameter properties for fluvial and aeolian material exported to the continental margin off Gambia. While only two magnetic and element EMs are required to unmix the terrigenous sediment fraction, three grain-size EMs were required. NNLSQ techniques reveal that the fine (<4 μm) and medium (10 μm) grain-size EMs have very similar magnetic and geochemical signatures, which are indicative of fluvial sediments in sub-tropical Africa. On the other hand, the coarse grain-size aeolian EM has a different composition, marked by a lower Al/Si and Fe/K and a higher Ti/Fe ratio and a higher hematite/goethite ratio.

Generally, the accumulation rates of fluvial sediments are higher than dust deposition, although, during HSs and the LGM the ratio of aeolian/fluvial material is high. The variation in MARs of fluvial material is primarily controlled by the distance between river mouth and core location and secondarily by precipitation in the hinterland. Accordingly, the variations in grain-size distributions of the fluvial material are re-

lated to the same mechanisms.

This study shows that the flux of aeolian material during the LGM is comparable to MIS 3–4, and that the most extensive dust input ($400 \text{ g m}^{-2} \text{ yr}^{-1}$) occurred during HS 1, with 100 times higher fluxes compared to modern times. The main driving factor for dust accumulation is controlled by the availability of source areas for deflation, which most likely relates to less dense vegetation in the hinterland during dry periods and exposed shelves that served as an additional dust sources. The input of fluvial material does not appear significantly reduced during HSs. It may thus be hypothesized, that observed dry conditions on millennial time-scales only affected the source areas of aeolian material, rather than the catchment of the Gambia River.

We suggest that for a characterization of EMs of terrigenous sediments, multi-proxy properties have to be determined and the data sets should ideally contain information about transport processes (e.g. grain-size analysis) and source area fingerprints (e.g. geochemistry, magnetic mineralogy).

Acknowledgments

We thank the crew and scientific party of Maria S. Merian cruise MSM 11/2 for helping to collect the studied cores. This study was funded by the Deutsche Forschungsgemeinschaft (DFG) through the international graduate college EUROPROX- Proxies in Earth History and MARUM Center for Marine Environmental Science.

References

- Aitchison, J., 1982. The Statistical Analysis of Compositional Data. *J. of the Roy. Stat. Soc. Series B*, 44(2): 139-177.
- Balsam, W.L., Otto-Bliesner, B.L. and Deaton, B.C., 1995. Modern and Last Glacial Maximum Eolian Sedimentation Patterns in the Atlantic Ocean Interpreted from Sediment Iron Oxide Content. *Paleoceanography*, 10.
- Bickert, T. and Mackensen, A., 2004. Last Glacial to Holocene changes in South Atlantic deep water circulation. In: G. Wefer, S. Mulitza and V. Ratmeyer (Eds.), *The South Atlantic in the Late Quaternary - Reconstruction of Material Budget and Current Systems*. Springer-Verlag, Berlin, pp. 671-693.
- Bouimetarhan, I. et al., 2009. Palynological evidence for climatic and oceanic variability off NW Africa during the late Holocene. *Quat. Res.*, 72(2): 188-197.
- Boyle, E.A., 1983. Chemical Accumulation Variations Under the Peru Current During the Past 130,000 Years. *J. Geophys. Res.*, 88(C12): 7667-7680.
- Castaneda, I. et al., 2009. Wet phases in the Sahara/Sahel region and human migration patterns in North Africa. *Proc. Nat. Acad. Sci.*, 106(48): 20159-20163.
- Chiappello, I. et al., 1997. Origins of African dust transported over the northeastern tropical Atlantic. *J. Geophys. Res.*, 102(D12): 13701-13709.
- Cohmap, M., 1988. Climatic changes of the last 18,000 years: observations and model simulations. *Science*, 241(4869): 1043-52.
- Collins, J.A. et al., 2011. Interhemispheric symmetry of the tropical African rainbelt over the past 23,000 years. *Nature Geosci.*, 4(1): 42-45.
- deMenocal, P. et al., 2000a. Abrupt onset and termination of the African Humid Period: Rapid climate responses to gradual insolation forcing. *Quat. Sci. Rev.*, 19(1-5): 347-361.
- deMenocal, P., Ortiz, J., Guilderson, T. and Sarnthein, M., 2000b. Coherent High- and Low-Latitude Climate Variability During the Holocene Warm Period. *Science*, 288(5474): 2198-2202.
- Engelstaedter, S., Tegen, I. and Washington, R., 2006. North African dust emissions and transport. *Earth Sci. Rev.*, 79(1-2): 73-100.
- Gac, J.Y. and Kane, A., 1986. Le fleuve Sénégal: I Bilan hydrologique et flux continentaux der matières particulaires a l'embouchure. *Sci. Geol. Bull.*, 39(1): 99-130.
- Gasse, F., 2000. Hydrological changes in the African tropics since the Last Glacial Maximum. *Quat. Sci. Rev.*, 19(1-5): 189-211.

- Gasse, F., 2001. PALEOCLIMATE: Hydrological Changes in Africa. *Science*, 292(5525): 2259-2260.
- Gasse, F., 2006. Climate and hydrological changes in tropical Africa during the past million years. *Compt. Rend. Palevol*, 5(1-2): 35-43.
- Govindaraju, K., 1994. 1994 Compilation of working values and samples description for 383 geostandards. *Geostandards Newsletter*, 18: 1-158.
- Grousset, F.E. et al., 2001. Zooming in on Heinrich Layers. *Paleoceanography*, 16(3): 240-259.
- Heslop, D., 2008. IRM Unmixer.
- Heslop, D. and Dillon, M., 2007. Unmixing magnetic remanence curves without a priori knowledge. *Geophys. J. Int.*, 170(2): 556-566.
- Holz, C., Stuut, J.-B.W., Henrich, R. and Meggers, H., 2007. Variability in terrigenous sedimentation processes off northwest Africa and its relation to climate changes: Inferences from grain-size distributions of a Holocene marine sediment record. *Sed. Geol.*, 202(3): 499-508.
- Hooghiemstra, H., Lézine, A.-M., Leroy, S.A.G., Dupont, L. and Marret, F., 2006. Late Quaternary palynology in marine sediments: A synthesis of the understanding of pollen distribution patterns in the NW African setting. *Quat. Int.*, 148(1): 29-44.
- Itambi, A.C., von Dobeneck, T., Mulitza, S., Bickert, T. and Heslop, D., 2009. Millennial-scale northwest African droughts related to Heinrich events and Dansgaard-Oeschger cycles: Evidence in marine sediments from offshore Senegal. *Paleoceanography*, 24: PA1205.
- Jullien, E. et al., 2007. Low-latitude "dusty events" vs. high-latitude "icy Heinrich events". *Quat. Res.*, 68(3): 379-386.
- Just, J., Dekkers, M.J., von Dobeneck, T., van Hoesel, A. and Bickert, T., Chap. 2. Unmixing signatures of eolian, fluvial, bacterial and diagenetic magnetic mineral fractions in Late Quaternary marine sediments off Gambia, NW Africa.
- Kohfeld, K.E. and Harrison, S.P., 2001. DIRTMAP: the geological record of dust. *Earth Sci. Rev.*, 54(1-3): 81-114.
- Koopmann, B., 1981. Sedimentation von Saharastaub im subtropischen Nordatlantik während der letzten 25.000 Jahre. *Meteor Forschungs-Ergebnisse*, 35: 23-59.
- Larrasoaña, J.C., Roberts, A.P., Rohling, E.J., Winkhofer, M. and Wehausen, R., 2003. Three million years of monsoon variability over the northern Sahara. *Clim. Dyn.*, 21(7-8): 689-698.
- Lesack, L.F.W., Hecky, R.E. and Melack, J.M., 1984. Transport of Carbon, Nitrogen, Phosphorus, and Major Solutes in the Gambia River, West Africa. *Limnol. Oceanogr.*, 29(4): 816-830.
- Löfberg, J., 2004. YALMIP: A toolbox for modeling and optimization in MATLAB, CACSD Conference, Taipei, Taiwan.
- Lynch-Stieglitz, J. et al., 2007. Atlantic Meridional Overturning Circulation During the Last Glacial Maximum. *Science*, 316(5821): 66-69.
- Mahowald, N. et al., 1999. Dust sources and deposition during the last glacial maximum and current climate: A comparison of model results with paleodata from ice cores and marine sediments. *J. Geophys. Res.*, 104(D13): 15895-15916.
- Mahowald, N.M. et al., 2006. Change in atmospheric mineral aerosols in response to climate: Last glacial period, preindustrial, modern, and doubled carbon dioxide climates. *J. Geophys. Res.*, 111(D10): D10202.
- Maley, J., 2000. Last Glacial Maximum lacustrine and fluvial Formations in the Tibesti and other Saharan mountains, and large-scale climatic teleconnections linked to the activity of the Subtropical Jet Stream. *Glob. Planet. Change*, 26(1-3): 121-136.
- Matthewson, A.P., Shimmield, G.B., Kroon, D. and Fallick, A.E., 1995. A 300 kyr High-Resolution Aridity Record of the North African Continent. *Paleoceanography*, 10(3): 677-692.
- Meyer, I., Davies, G.R. and Stuut, J.-B.W., 2011. Grain size control on Sr-Nd isotope provenance studies and impact on paleoclimate reconstructions: An example from deep-sea sediments offshore NW Africa. *Geochem. Geophys. Geosyst.*, 12(3): Q03005.
- Moreno, T. et al., 2006. Geochemical variations in aeolian mineral particles from the Sahara-Sahel Dust Corridor. *Chemosphere*, 65(2): 261-270.
- Mulitza, S. et al., 2008. Sahel megadroughts triggered by glacial slowdowns of Atlantic meridional overturning. *Paleoceanography*, 23(4): PA4206.
- Niedermeyer, E.M. et al., 2010. Orbital- and millennial-scale changes in the hydrologic cycle and vegetation in the western African Sahel: insights from individual plant wax [δ D] and [δ 13C]. *Quat. Sci. Rev.*, 29(23-24): 2996-3005.
- Peters, C. and Dekkers, M.J., 2003. Selected room temperature magnetic parameters as a function of mineralogy, concentration and grain size. *Phys. Chem. Earth, Parts A/B/C*, 28(16-19): 659-667.
- Prospero, J.M., 1996. The atmospheric transport of particles to the ocean. In: V. Ittekkott, S. Honjo and P.J. Depetris (Eds.), *Particle Flux in the Ocean*. John Wiley, New York, pp. 19-52.
- Prospero, J.M., Ginoux, P., Torres, O., Nicholson, S.E. and Gill, T.E., 2002. Environmental characterization of global sources of atmospheric soil dust identified with the NIMBUS 7 Total Ozone Mapping Spectrometer (TOMS) absorbing aerosol product. *Rev. Geophys.*, 40(1): 1002.
- Pye, K., 1987. Aeolian dust and dust deposits. *Acad.*

- demic press, London, 334 pp.
- Ruddiman, W.F., 1997. Tropical Atlantic terrigenous fluxes since 25,000 yrs B.P. *Mar. Geol.*, 136(3-4): 189-207.
- Sarnthein, M., 1978. Sand deserts during glacial maximum and climatic optimum. *Nature*, 272(5648): 43-46.
- Sarnthein, M., Tetzlaff, G., Koopmann, B., Wolter, K. and Pflaumann, U., 1981. Glacial and interglacial wind regimes over the eastern subtropical Atlantic and North-West Africa. *Nature*, 293(5829): 193-196.
- Sarnthein, M. et al., 1994. Changes in East Atlantic Deepwater Circulation Over the Last 30,000 years: Eight Time Slice Reconstructions. *Paleoceanography*, 9(2): 209-267.
- Sarnthein, M., et al., Fundamental modes and abrupt changes in North Atlantic circulation and climate over the last 60 ky—Concepts, reconstructions and numerical modeling, in *The Northern North Atlantic: A Changing Environment*, edited by P. Schäfer et al., pp. 365–410, Springer-Verlag, New York, 2001.
- Schäfer-Neth, C. and Paul, A., 2004. The Atlantic Ocean at the Last Glacial Maximum: 2. Reconstructing the current systems with a global ocean model. In: G. Wefer, S. Mulitza and V. Ratmeyer (Eds.), *The South Atlantic in the Late Quaternary - Reconstruction of Material Budget and Current Systems*. Springer-Verlag, Berlin, pp. 549-583.
- Schefuß, E., Schouten, S. and Schneider, R.R., 2005. Climatic controls on central African hydrology during the past 20,000 years. *Nature*, 437(7061): 1003-1006.
- Schneider, R.R., Price, B., Müller, P.J., Kroon, D. and Alexander, I., 1997. Monsoon Related Variations in Zaire (Congo) Sediment Load and Influence of Fluvial Silicate Supply on Marine Productivity in the East Equatorial Atlantic During the Last 200,000 Years. *Paleoceanography*, 12(3): 463-481.
- Shackleton, N.J., Hall, M.A. and Vincent, E., 2000. Phase relationships between millennial-scale events 64,000-24,000 years ago. *Paleoceanography*, 15(6): 565-569.
- Stuut, J.-B. et al., 2005. Provenance of present-day eolian dust collected off NW Africa. *J. Geophys. Res.*, 110: D04202.
- Tomczak, M., 2003. *Regional oceanography: An introduction* Daya Publishing House.
- Van Meerbeeck, C.J., Renssen, H. and Roche, D.M., 2008. How did Marine Isotope Stage 3 and Last Glacial Maximum climates differ? Perspectives from equilibrium simulations. *Clim. Past Discuss.*, 4(5): 1115-1158.
- Waelbroeck, C. et al., 2002. Sea-level and deep water temperature changes derived from benthic foraminifera isotopic records. *Quat. Sci. Rev.*, 21(1-3): 295-305.
- Weltje, G., 1997. End-member modeling of compositional data: Numerical-statistical algorithms for solving the explicit mixing problem. *Math. Geol.*, 29(4): 503-549.
- Weltje, G.J. and Prins, M.A., 2007. Genetically meaningful decomposition of grain-size distributions. *Sed. Geol.*, 202(3): 409-424.
- White, F., 1983. *A Descriptive Memoir to Accompany the UNESCO/AETFAT/UNSO Vegetation Map of Africa*. United Nations Educational, Scientific, and Cultural Organization, Paris.
- Wien, K., Wissmann, D., Kölling, M. and Schulz, H.D., 2005. Fast application of X-ray fluorescence spectrometry aboard ship: how good is the new portable Spectro Xepos analyser? *Geo Mar. Lett.*, 25(4): 248-264.
- Zabel, M., Bickert, T., Dittert, L. and Haese, R.R., 1999. Significance of the Sedimentary Al/Ti Ratio as an Indicator for Variations in the Circulation Patterns of the Equatorial North Atlantic. *Paleoceanography*, 14(6): 789-799.
- Zabel, M. et al., 2001. Late Quaternary Climate Changes in Central Africa as Inferred from Terrigenous Input to the Niger Fan. *Quat. Res.*, 56(2): 207-217.

Chapter 4

Paleoenvironmental influence on the multi-proxy characteristics of terrigenous sediments off NW Africa

Janna Just^{1,2,3}, Mark J. Dekkers^{3,4}, Tilo von Dobeneck^{1,2,3}

¹ Marine Geophysics, Depart. of Geosciences, Klagenfurter Strasse, University of Bremen,

² MARUM—Center for Marine Environmental Sciences, Leobener Strasse, University of Bremen, Germany

³ International Graduate College EUROPROX

⁴ Paleomagnetic Laboratory 'Fort Hoofddijk', Depart. of Earth Sciences, Budapestlaan 17, Utrecht University, The Netherlands.

To submit to Sedimentary Geology

We investigated the multi-proxy characteristics of aeolian and fluvial End Members (EM) on NW African core material off the Senegal (GeoB 9508-5, 15°29.90'N; 17°56.88'W) and Gambia (GeoB 13602-1, 13°32.71'N, 17°50.96'W) Rivers. A non-negative least square fitting approach enabled us to reconstruct associated properties of grain-size EMs. While the elemental composition of dust at both study sites is similar, the magnetic mineralogy distinctively differs. This suggests that the material originates from different source areas. Proximal dust of coarse grain sizes and associated coarse-grained magnetite contributes to the terrigenous fraction mainly during Heinrich stadials and has a higher impact at the northern core location. Finer aeolian material is only present in the northern core and corresponds to sediments transported from a more distant source area. This fraction probably corresponds to material transported by the African Easterly Jet. The fluvial material of the Senegal and Gambia Rivers also shows distinct differences of their magnetic mineralogy, but similar elemental compositions. Off the Gambia, the material contains a higher amount of high-coercivity magnetic minerals (hematite and goethite) compared to the Senegal. This could be attributed to the different soil distributions in both river basins. The production of bacterial magnetites appears to be associated with higher marine productivity during humid phases and consequently also to enhanced accumulation of fluvial material. It may therefore bias the magnetic signature of fluvial sediments. The investigation of the multi-proxy characteristics enables a three-level interpretation of transport energy, transport mechanism, and weathering conditions in the source area of the sediments. The grain-size distribution of the terrigenous EMs reveals the energetic conditions during transport. The elemental composition is distinctively different for material derived from different climate zones, and thus enables a discrimination of river and wind transported material. The magnetic mineralogy can be used as a proxy for specific pedogenic processes in the two river basins and source areas of aeolian material.

4.1 Introduction

At the African continental margin geochemical and magnetic properties as well as grain-size distributions are powerful tools for reconstructing past environmental conditions (Koopmann 1981; Bloemendal et al. 1992; Matthewson et al. 1995). Elemental ratios of sediments are often indicative of the weathering conditions in the source area (Zabel et al. 2001) and grain-size data serve for reconstructing the transport mechanism (Koopmann 1981). Therefore both parameters can be used for the discrimination of fluvial and aeolian inputs. The use of these proxies is supported by the analyses of fluvial samples from the Senegal River and from dust samples (Gac and Kane 1986; Chiapello et al. 1997; Moreno et al. 2006). However, since it has been shown that especially elemental ratios are influenced by grain-size effects and thus gravitational sorting during transport (e.g., Caquineau et al. 1998), the use of specific elemental ratios as deterministic end-members of dust and fluvial material is challenging. On the other hand, rock-magnetic data, i.e. Isothermal Remanent Magnetization (IRM) curves, are indicators for the magnetic mineralogy. The magnetic mineralogy of sediments mirrors the magnetic inventory of the parent rock and on secondary formed minerals during soil pedogenesis (e.g., Maher 1986). Therefore, they can be indicative of weathering conditions in the source area (Kämpf and Schwertmann 1983; Schwertmann

and Taylor 1989). Another important contributor of magnetic minerals in marine sediments is bacterial magnetite (Kirschvink and Chang 1984; Petersen et al. 1986; Stolz et al. 1986). The identification of this magnetic phase is crucial, if variations in the magnetic mineralogy are used to reconstruct past terrigenous inputs (Just et al., Chap. 2). In anoxic sediment, the fine-grained magnetosomes get dissolved rapidly during burial (Hilgenfeldt 2000) and are dissolved below the iron-redox boundary (e.g., Housen and Moskowitz 2006). If preserved, their abundance varies on glacial interglacial timescales (Hesse 1994; Lean and McCave 1998; Dinarès-Turell et al. 2003; Housen and Moskowitz 2006; Roberts et al. 2011). The ecological control of magnetotactic bacteria, which produce these so-called magnetosomes, is however poorly constrained and limiting factors are dependent on the (micro-) environmental setting: In pelagic sediments the availability of nutrients, e.g., iron (Roberts et al. 2011) is an important factor for the occurrence of magnetotactic bacteria (Hesse 1994), while the input of organic matter and linked oxygenation states of the subsurface have to be balanced for a colonization and preservation in the geological record (Roberts et al. 2011). Lean and McCave (1998) suggested that a decrease in carbon flux and thus a thickening of the aerobic zone during interglacials, would have left a longer time for the colonization of

magnetotactic bacteria, while in other settings their abundance is positively linked to organic carbon input (Roberts et al. 2011). In proximal cores in the Mediterranean (Dinarès-Turell et al. 2003) the abundance and preservation of bacterial magnetite appears to be linked to interstadial periods. In those settings, the limiting factors are also poorly constrained, and are probably linked to the oxygenation of the sediments (Dinarès-Turell et al. 2003).

Our study aims to distinguish multi-proxy characteristics of aeolian and fluvial material, and compare regional compositional changes of those components. We wish to evaluate if we can distinguish between different source areas of the material. Secondly, we want to test if the occurrence of bacterial magnetite can be linked to climatic variations in our setting, and a possible association to higher bioproductivity or nutrient input (i.e. river runoff).

To obtain the multi-parameter properties of fluvial and aeolian material, we apply an approach developed by Just et al. (Chap. 3). They showed that there is a reasonable relationship between grain-size distribution, elemental composition, and magnetic mineralogy. The approach will be applied on two gravity cores retrieved at the continental margin off the Senegal (GeoB 9508-5) and Gambia Rivers (GeoB 13602-1) where the terrigenous fraction corresponds to a mixture of aeolian and fluvial sediments (Mulitza et al. 2008; Just et al. Chap. 2).

In a first step we unravel EMs from geochemical, rock-magnetic, and grain-size data sets,

respectively. Since the abundance of grain-size EMs correspond to volume fractions and can be used for calculating fluxes, we assess their associated geochemical and magnetic properties. Non-negative least square fitting (NNLSF) techniques have been applied on the volume fractions of the grain-size EMs and the geochemical and IRM data sets. This approach corresponds to a volume calibration of elemental and magnetic data. By including an additional EM for the volume contribution of carbonate we can test if potentially magnetite produced by magnetotactic bacteria can be linked to an enhanced marine bioproductivity or fluvial input, i.e. nutrients.

4.2 Setting

The studied gravity cores GeoB 9508-5 (15°29.90'N; 17°56.88'W, 2,384 m water depth) and GeoB 13602-1 (13°32.71' N, 17°50.96'W, 2,395 m water depth) were retrieved on the continental margin off NW Africa during *Meteor* cruise M65/1 and *Maria S. Merian* cruise MSM 11/2, respectively. The Senegal catchment is wide and extends over different vegetation zones (Fig. 4-1a). Thus, the input of fluvial material reflects the environmental conditions (e.g., precipitation, pedogenic minerals, Fig. 4-1b) of a wide area. The catchment of the Gambia River is comparatively small and mainly reflects more the regional signature of the material in the source area and possible imprint of weathering processes.

Additionally, aeolian material from the Sahara and Sahel is transported to both sites by NE

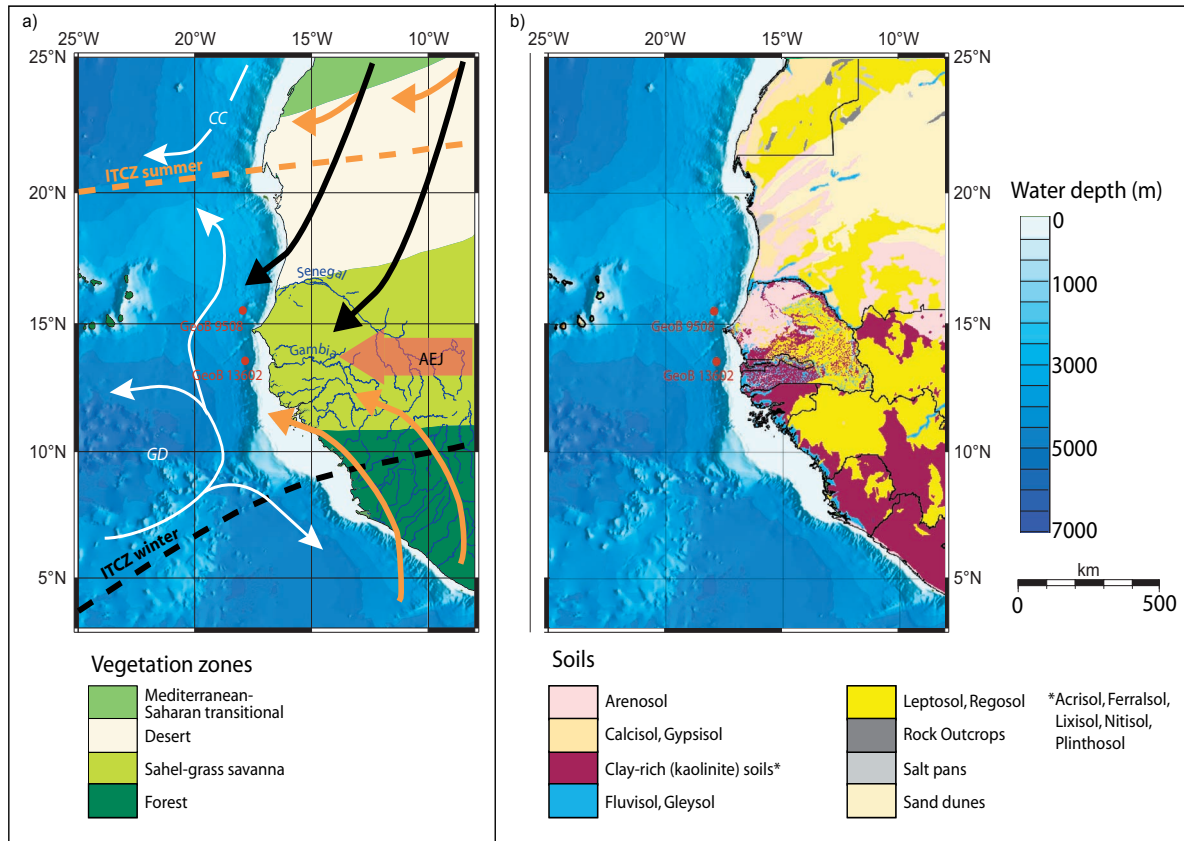


Fig. 4-1: (a) Vegetation belts on the NW African continent (modified after White 1983). Oceanic surface circulation (white arrows) is controlled by the North Equator Counter Current (*NEEC*) and associated anticyclonic circulation around the Guinea Dome (*GD*) and by the Canary Current (*CC*). Orange and black arrows indicate atmospheric features during summer and winter, respectively. (b) Distribution of soils in the Gambia and Senegal River catchments (data from *Harmonized Soils World Database 2009*, modified). Gravity core GeoB 13602-1 and GeoB 9508-5 are depicted in red.

trade winds at lower atmospheric altitude and by the higher African Easterly Jet (AEJ, Pye 1987). The trade winds are thought to transport proximal dust to the Atlantic (Pye 1987) while aeolian material transported by the AEJ, has a high potential to reach the Caribbean (Prospero and Carlson 1980).

4.3 Material and Methods

Previously published data of GeoB 9508-3 and GeoB 13602-1 reveal that elemental ratios and grain-size distributions (Mulitza et al. 2008; Just et al. Chap. 3) as well as rock magnetic

records and EM modeling (GeoB 13602-1) of the respective data sets can successfully be used for reconstructing past fluvial and aeolian dominated sedimentation over the past 80 ka. The age model for GeoB 13602-1 was developed by Just et al. (Chap. 2) by correlating the oxygen isotope record to that of MD95-2042 (Shackleton et al. 2000) and six radiocarbon ages while the age model of GeoB 9508-5 (Mulitza et al. 2008) was obtained by correlating the oxygen isotope record of MD95-2042 with the age model of Shackleton et al. (2004). For consistency between the cores used in this study, we tied the

oxygen isotope record of GeoB 9508-5 (Mulitza et al. 2008) to the record of Shackleton et al. (2000) and additionally used the radiocarbon datings of Mulitza et al. (2008). Geochemical analyses were carried out on dried samples by energy dispersive polarization X-ray fluorescence (EDP-XRF) spectroscopy using a SPECTRO XEPOS device and the grain-size distributions were measured on a Coulter laser particle sizer LS200 after removing organic carbon and CaCO_3 . For further details we refer the reader to the respective studies.

4.3.1 Rock magnetic measurements

Rock magnetic properties were measured on 6.2 cm³ samples taken at 5 cm spacing. The magnetic susceptibility (χ) was measured onboard with a Bartington MS2 susceptibility meter with a 140 mm loop sensor. Artificial remanence acquisition and measurements were performed on an automated 2 G Enterprise 755 R DC superconducting magnetometer. The device is equipped with in-line AF and DC coils for generating anhysteretic remanent magnetization (ARM, 100 mT peak AF and 40 μT DC) and an in-line pulse magnetizer to impart isothermal remanent magnetization (IRM). The $\text{ARM}_{100\text{ mT}}$ serves as an indicator for the presence of fine-grained single domain (SD) magnetite particles (King et al. 1982; Frederichs et al. 1999). IRM acquisition curves of magnetic minerals depend on the coercivity distributions for different magnetic minerals (e.g., Eyre 1996; Frank and Nowaczyk 2008) and can therefore be used to distinguish

the magnetic inventory of each sample. For IRM acquisition the peak field was increased in 24 increments from 5 to 700 mT. For the acquisition at higher fields up to 2,700 mT, we used an “external” pulse magnetizer (2G Enterprise). The IRM acquired after imparting a field of 100 mT ($\text{IRM}_{100\text{mT}}$) serves to estimate the multidomain (MD) magnetite content (Frederichs et al. 1999). Additionally, the S-Ratio

$$S = 0.5[(-\text{IRM}_{-300\text{mT}} / \text{SIRM}) + 1] \quad (4-1)$$

(Bloemendal et al. 1992), was calculated, which represents the ratio of low to high-coercivity magnetic minerals. The hard IRM (HIRM) acquired above 300 mT (Stoner et al. 1996),

$$\text{HIRM} = 0.5(\text{SIRM} + \text{IRM}_{-300\text{mT}}) \quad (4-2)$$

quantifies the high-coercivity magnetic minerals (Frederichs et al. 1999; Kruijver and Passier 2001; Heslop 2009).

4.3.2 End-member unmixing

The element, grain-size and IRM data sets were unraveled using the IRM Unmixer code by Heslop and Dillon (2007), which is similar to the approach developed by Weltje (1997).

In the fundamental equation of EM analysis,

$$\mathbf{X} = \mathbf{A}\mathbf{S} + \mathbf{E}, \quad (4-3)$$

\mathbf{X} corresponds to the measured data set where each of the n rows corresponds to a sample and

the m columns correspond to the variables for each sample. Matrix A represents the n mixing coefficients for each sample of a set of k EMs in columns. S represents the m properties of the k EMs and E corresponds to the error matrix. A non-negativity constraint and sum-to-one criteria are included in the algorithm. For further details of the approach we refer the reader to Weltje (1997) and Heslop and Dillon (2007).

The input of the element data correspond to mass concentrations and when assuming that the considered elements, i.e. their oxides correspond to the approximate samples total mass, the mixing coefficients correspond to mass concentrations of the EMs. We considered the ‘terrigenous elements’ Si, Al, K, Fe, Ti and normalized their mass concentrations to their cumulative abundance plus the concentration of Ca. Note however, that for the unmixing procedure Ca was excluded. The grain-size distributions are given in volume fraction, so do the mixing coefficients of grain-size EMs. The mixing coefficients of the IRM data however, correspond to the proportion of each EM to saturation isothermal remanent magnetization (SIRM). There are two reasons, why the SIRM proportion cannot directly be translated into mass or volume proportions. At first, the SIRM of magnetic minerals differs and is grain-size dependent, e.g. pure magnetite of increasing grain size has SIRMs of 0.5-30 Am²kg⁻¹, while hematite has SIRMs of 0.2 Am²kg⁻¹ (Peters and Dekkers 2003). Secondly, the concentration of magnetic minerals within a certain volume may vary. To account for both

factors and to calibrate the proportion of SIRM to volume, the concentration c and mineral specific magnetic parameters m , i.e., SIRM, of the magnetic inventory must be considered:

$$vol_{SIRM} = c * m * SIRM \quad (4-4)$$

4.3.3 Multi-proxy approach and volume calibration

As outlined in the previous section, only the contribution of the grain-size EMs relate to the total volume and can therefore be used for calculating fluxes of terrigenous material. For finding the properties, i.e. mass concentrations of elements and magnetic minerals, a volume calibration would be necessary.

We alternatively perform non-negative least square fitting (NNLSF) on the grain-size EM contributions and the original element data and IRM acquisition curves. By this approach the mass concentration of each element and the SIRM per volume of each EM can be quantified. The assumption underlying the approach is that sediments transported by a certain energetic transport mechanism mirror the distinct properties of the material in the respective source areas. Therefore, based on the volumetric mixing contributions of the grain-size EMs A_G associated geochemical (P_E) and magnetic properties (P_M) can be predicted:

$$X_E = A_G P_E + R \quad (4-5)$$

$$X_M = A_G P_M + R \quad (4-6)$$

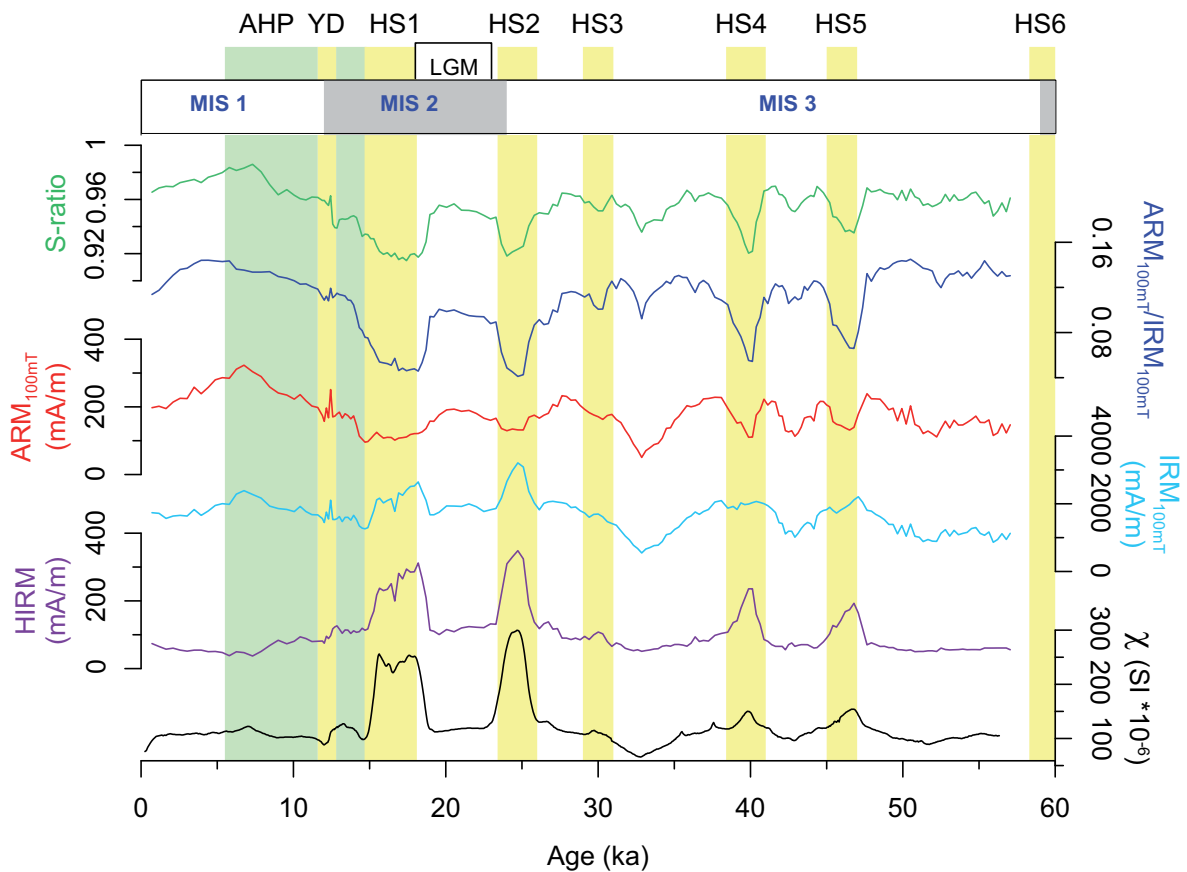


Fig. 4-2: Rock magnetic record for GeoB 9508-5. MIS: Marine Isotope Stage, AHP: African Humid Period, YD: Younger Dryas, HS: Heinrich Stadials (after Sarnthein et al., 2001), LGM: Last Glacial Maximum.

where X_E and X_M corresponds to the elemental concentrations and IRM data, respectively. To test if a preserved bacterial magnetite phase is associated to marine bioproductivity, we added an additional EM to the grain-size EMs whose volume fraction was calculated on the basis of the Ca concentration (Mulitza et al. 2008; Just et al. Chap. 3). Consequently, we included Ca also in the NNLSF approach. For details about this approach, we refer the reader to (Just et al. Chap. 3). Since we used un-normalized data, the predicted elemental concentrations and IRM acquisition curves correspond to the concentration of each element and the total IRM per volume of the respective EM.

4.4 Results

4.4.1 Rock-magnetic parameters

All magnetic parameters show significant maxima (S-Ratio, ARM/IRM, IRM_{100mT} , HIRM, susceptibility) and minima (ARM_{100mT}) during Heinrich Stadials (HS, Fig. 4-2). The strongest peaks correspond to HS 2 and 1. Note however, that in the S-ratio and ARM/IRM and ARM_{100mT} all HS have similar amplitudes, except HS 3. The Younger Dryas is marked by a minor, though sharp, excursion.

4.4.2 End-member Analyses

For unmixing the elemental data, two EMs suffice a coefficient of determination R^2 of 0.99 (Fig. 4-3). In the following they will be referred

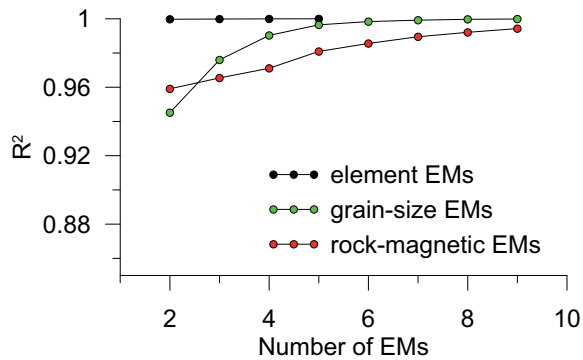


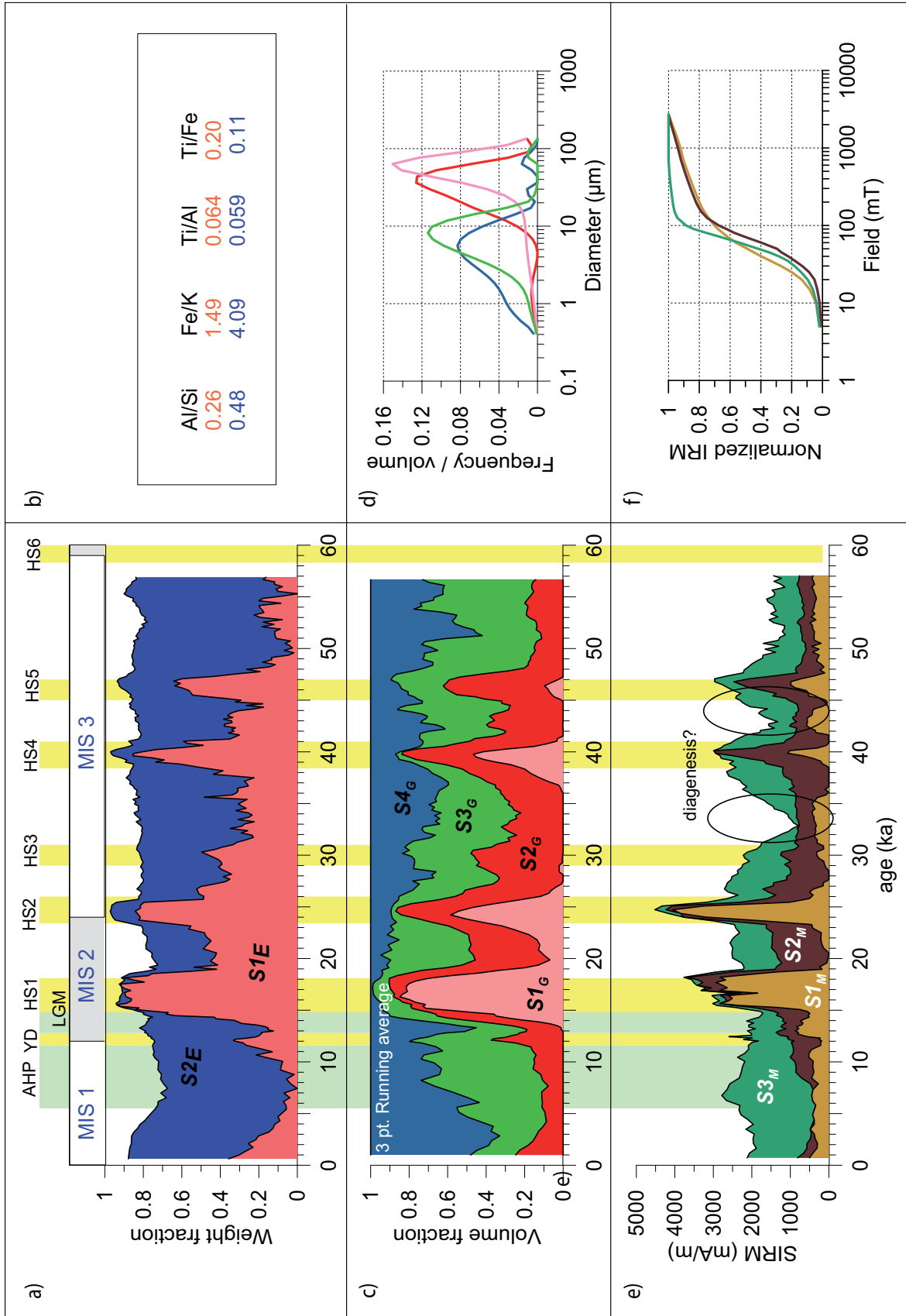
Fig. 4-3: Coefficient of determination (R^2) based on Principle Component analyses as a decision criterion for the number of EMs.

to as $S1_E$ and $S2_E$. The element concentrations and calculated element ratios are shown in Table 4-1a and Fig. 4-4b. The total mass concentration of the considered EM varies by less than 6%. Thus, it can be assumed that the considered elements correspond to a reasonable approximation of all terrigenous elements. The EMs reveal distinct differences in terms of geochemical composition; $S1_E$ has low Al/Si, Fe/K ratios and weathering index and slightly higher Ti/Fe ratio with respect to $S2_E$. The difference in the Ti/Al ratio appears insignificant. The downcore record (Fig. 4-4a) reveals that the $S1_E$ contribution is very high during HSs, especially during HS 5, 4, 2, 1 while the remainder of the record is dominated by $S2_E$. Additionally, during the Younger Dryas the $S1_E$ contribution has a minor peak. During the African Humid Period (AHP),

$S1_E$ has low contributions however, successively increases from the end of the AHP (~5 ka) towards the present.

Four EMs have been used to unravel the grain-size data set having an R^2 of 0.98 (Fig. 3). Each of the EMs (S_G) has a quasi-unimodal distribution (Fig. 4-4 d) with decreasing modes from $S1_G$ to $S4_G$ (60 μm , 40 μm , 8 μm , 6 μm). A secondary mode appears in the finest $S4_G$, which cannot be isolated by the algorithm, even when the number of EMs is increased. The downcore record (Fig. 4-4c) reveals that the volume contribution of $S1_G$ and $S2_G$ increases during MIS 3 and on average corresponds to no less than 30%. During HSs, the $S1_G$ proportion peaks significantly with highest abundance during HS 1, 2, 4 while the contribution of $S2_G$ remains relatively stable except for a peak during HS 5. During the Holocene, the contribution of $S2_G$ is below 20%, note that the coarsest $S1_G$ is absent during that time. The abundance of $S3_G$ is relatively constant during MIS 3, except during HSs, while the proportion of $S4_G$ successively decreases during MIS 4 and 3 and is largely unaffected during HSs. During the AHP $S3_G$ dominates, however, also the proportion of $S4_G$ is enhanced and fi-

Fig. 4-4: End-member Models of the element, grain-size and rock-magnetic data. (a) Cumulative downcore contribution of element EMs S_E normalized to the sum of concentration of considered elements plus Ca. (b) Elemental ratios calculated based on the elemental composition of the EMs (cf. Table 4-1a). (c) Cumulative downcore contribution of grain-size EMs S_G . (d) $S1_G$ and $S2_G$ correspond to a coarse sediment fraction, which is indicative for dust exported to the Atlantic Ocean, while the fluvial $S3_G$ and $S4_G$ are much finer. (e) Cumulative downcore contributions of SIRM of rock-magnetic EMs. (f) IRM acquisition curves of rock magnetic EMs. The curve of $S1_M$ represents a mixture of coarse magnetite and a high concentration of high-coercivity minerals (hematite and goethite). $S3_M$ reveals a lower concentration of coarse grained magnetite and equally high-coercivity magnetic minerals. The shape of $S2_M$ indicates that magnetite is the main contributor to the magnetic inventory. The gently rising slope at fields higher than 100 mT suggests an additional phase of high-coercivity magnetic minerals.



nally dominates during the Late Holocene.

For unmixing the IRM data, three EMs (S_M) were used (R^2 of 0.96). The acquisition curve of $S1_M$ rises at lower fields than those of $S2_M$ and $S3_M$ (Fig. 4-4f). Above 100 mT the curves rise linearly on a logarithmic scale. This suggests that low-coercivity magnetic minerals (e.g., coarse grained magnetite) and high-coercivity minerals (e.g., hematite and goethite) are present in the magnetic inventory. The slope of $S2_M$ starts to rise at higher fields, above ~150 mT the slope rises linearly on a logarithmic scale, but however, somewhat less steep than that of $S1_M$. This indicates that $S2_M$ contains ‘harder’ magnetite, i.e., finer magnetic grain sizes and a lower content of high-coercivity magnetic minerals. The acquisition curve of $S3_M$ rises at intermediate fields. Also here, at 100 mT a change in the slope occurs, suggesting that it contains a high proportion of a magnetic phase, which is saturated at this field step (i.e., magnetite). At higher fields the slope rises gently until an

approximate saturation at ~300 mT.

Since the IRM data relate to SIRM, rather than to volume or mass fractions (cf. 4.3.2), we show the downcore contribution scaled to SIRM (Fig. 4-4e). The contribution of $S1_M$ is relatively low throughout the section, except pronounced peaks during HS 5, 4, 2, 1 of which HS 2 and 1 are by far the strongest. The abundance of $S2_M$ is enhanced during HS 5 and 4, the LGM and the Younger Dryas. During the Late Holocene, $S1_M$ contributes but with low intensities and $S2_M$ is literally absent. The proportion of $S3_M$ remains relatively constant throughout the record and is only significantly reduced during HSs and in intervals between 43-45 ka and 33-35 ka. A strong reduction of SIRM in those intervals hints to reductive diagenesis.

4.4.3 Multi-proxy characteristics of grain-size end-members

Senegal site GeoB 9508-5

The calculated elemental ratios for the grain-size EMs are very similar to the ones obtained

		Al	Si	K	Ti	Fe	Ca	Mg	Al/Si	Fe/K	Ti/Al	Ti/Fe	(Fe+Al)/(Si+Ti+K)
<i>GeoB9508-5</i>													
a)	$S1_E$	0.182	0.711	0.038	0.012	0.057	na	na	0.256	1.487	0.064	0.205	0.314
	$S2_E$	0.261	0.543	0.036	0.015	0.145	na	na	0.481	4.095	0.059	0.106	0.684
b)	$P1_E$	71192	283921	12938	4221	17728	0	na	0.251	1.370	0.059	0.238	0.295
	$P2_E$	75490	297673	18158	5361	23112	0	na	0.254	1.273	0.071	0.232	0.307
	$P3_E$	98590	220692	12659	5820	53294	0	na	0.447	4.210	0.059	0.109	0.635
	$P4_E$	100699	199084	13050	5524	52229	0	na	0.506	4.002	0.055	0.106	0.703
	$P5_E$	0	0	533	0	8032	408604	na	na	15.071	na	0.000	15.071
<i>GeoB13602-1</i>													
c)	$S1_E$	0.174	0.700	0.030	0.013	0.056	na	0.027	0.249	1.843	0.076	0.238	0.310
	$S2_E$	0.249	0.554	0.027	0.018	0.122	na	0.030	0.450	4.506	0.070	0.144	0.620
d)	$P1_E$	70218	294993	10135	5130	14793	0	na	0.238	1.460	0.073	0.347	0.274
	$P2_E$	91178	232387	10482	6738	42333	0	na	0.392	4.039	0.074	0.159	0.535
	$P3_E$	98100	216186	10329	6732	45226	0	na	0.454	4.379	0.069	0.149	0.614
	$P4_E$	0	1470	4181	0	9981	400439	na	0.000	2.387	na	0.000	1.766

Table 4-1: Elemental composition and element ratios of element EMs S_E and predicted associated properties P_E of the grain-size End Members. (a, b) GeoB 9508-5, (c, d) GeoB13602-1.

by unmixing the element data set (Table 4-1a, b). $P1_E$ and $P2_E$ have low Al/Si and high Fe/K and weathering index with respect to $P3_E$ and $P4_E$. The biogenic $P5_E$ is mostly associated with Ca.

The IRM acquisition curves of $P1_M$ and $P2_M$ have slightly higher SIRMs with respect to the remaining P_M (Fig. 4-5a). The by far lowest SIRM has $P5_M$ which corresponds to the carbonate fraction. The IRM curves normalized to one reveal compositional differences in the magnetic mineralogy (Fig. 4-5b): $P1_M$ contains a mixture of magnetically ‘soft’ and ‘hard’ components. The curve of $P2_M$ rises at higher fields

with respect to $P1_M$ and is flatter above ~ 130 mT. The normalized acquisition curve of $P3_M$ and $P4_M$ are very similar and depart only above 100 mT, where $P3_M$ is flatter with respect to $P4_M$. In contrast, the IRM acquisition curve of the biogenic fraction $P5_M$ steeply rises above 40 mT and is fully saturated at ~ 120 mT.

Gambia site GeoB 13602-1

The calculated elemental ratios for the grain-size EMs $S1_G$ to $S3_G$ of GeoB 13602-1 resemble the ones obtained by unmixing the element data set (see Table 4-1c). Table 4-1d shows the associated properties P_E : $P1_E$ has low Al/Si and high Fe/K and weathering index, with respect

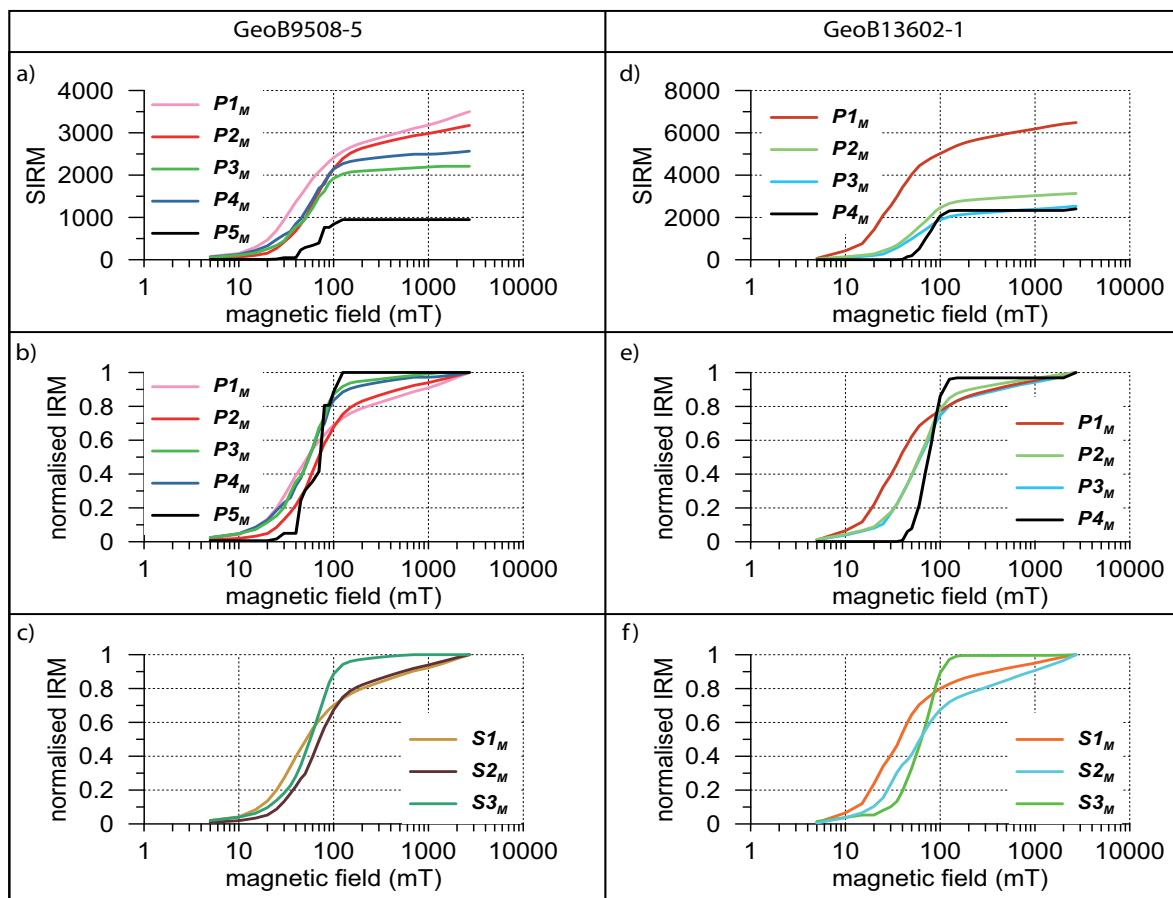


Fig. 4-5: Predicted IRM acquisition curves (P_M) from the least square fitting approach of GeoB 9508-5 (a, b) and GeoB 13602-1 (d, e) in comparison to the IRM acquisition curves from EM unmixing of the magnetic data sets (c, f).

to $P2_E$ and $P3_E$. The properties $P4_E$ associated to the biogenic fraction are dominated by a high concentration of Ca.

The acquisition curve $P1_M$ is much higher with respect to the other EMs (Fig. 4-5d). The shapes of the acquisition curves also show distinct differences (Fig. 4-5e). $P1_M$ starts to acquire IRM at low fields above 20 mT. A change in slope occurs at ~ 80 mT and above the curve rises linearly on a logarithmic scale. The IRM acquisition curves of $P2_M$ and $P3_M$ have similar shapes. The curves start to rise at higher fields (~ 30 mT), the break in slope occurs at ~ 130 mT and rises above linearly on the logarithmic scale, whereby the curve of $P2_M$ is less steep, while the gradient of $P3_M$ is comparable to $P1_M$. The IRM acquisition curve of the carbonate fraction $P4_M$ is very narrow and starts to rise at 50 mT and is completely saturated at 110 mT.

4.5. Discussion

4.5.1 Interpretation of end-members in GeoB 9508-5

Based on the geochemical composition of the element EMs S_E and the previously reported geochemical composition of aeolian dust samples (Chiapello et al. 1997; Moreno et al. 2006) and material from the Senegal River (Gac and Kane 1986, cf., Chap. 3, Table 3-1), we suggest that $S1_E$ corresponds to dust and $S2_E$ to river material. This interpretation is further supported by the downcore record, which shows extremely high $S1_E$ contributions during HSs.

$S1_G$ and $S2_G$ have modes coarser than 20 μm ,

while $S3_G$ and $S4_G$ are finer than 10 μm . The investigation of present-day dust samples collected off NW Africa indicate, that aeolian material is mostly coarser than 8 μm (Stuut et al. 2005), while 90% and 95% of suspended particles at the Senegal River mouth is finer than 5 μm and 10 μm , respectively. We therefore assume that the coarse EM $S1_G$ and $S2_G$ correspond to aeolian material, whose contribution is highly enhanced during HSs and the LGM, and the fine EMs $S3_G$ and $S4_G$ correspond to fluvial material. The observed strong reduction of the $S3_G$ (mode of 7 μm) during HSs might point to the fact that the water discharge and thus the potential for a transport of coarser particles into the ocean was strongly reduced during those dry intervals.

The main difference between the three S_M is the proportion of high-coercivity minerals in $S1_M$ and $S2_M$ with respect to $S3_M$. The formation of pedogenic iron-oxides is mainly influenced by Eh/pH conditions and the excess of water within the soils (Kämpf and Schwertmann 1983). For instance, decreasing soil temperature and a higher availability of water within the soil leads to a decrease in the pedogenic formation of hematite with respect to goethite (Maher 1986; Schwertmann and Taylor 1989). In former studies the ratio of hematite/goethite in a marine sedimentary record has been used to reconstruct paleomonsoonal precipitation over SE Asia (Zhang et al. 2007) and off the Amazon (Harris and Mix 1999). Furthermore, (Lyons et al. 2010) reported an association of increasing rainfall and the pedogenic formation of magnetite with respect

to high-coercivity phases (i.e., hematite). They, however, did not discriminate between hematite and goethite. Based on the downcore contributions i.e., the high abundance of $S1_M$ and $S2_M$ during HSs, these EMs most likely corresponds to aeolian sediments. Based on the strong reduction of the ‘magnetite rich’ $S3_M$ during HSs and the domination during the Holocene, we infer at this point that $S3_M$ corresponds to a background EM, which has to be further evaluated by multi-proxy characteristics.

4.5.2 Associated properties of grain-size end-members

Senegal site GeoB 9508-5

A striking feature of the predicted properties in terms of elemental composition P_E and IRM acquisition curves P_M is their similarity to the original EMs S_E and S_M (cf., Table 4-1a, b and Fig. 4-5b, c). The elemental compositions of $P1_E$ and $P2_E$ are similar to $S1_E$, while the elemental composition of $P3_E$ and $P4_E$ resemble $S2_E$. The elemental composition associated to the carbonate fraction $P5_E$ however reveals that Ca and traces of Fe and K are the only contributors.

For the normalized IRM acquisition curves similarities exist between $P1_M$ and $S1_M$, $P2_M$ and $S2_M$ (Fig. 4-5b, c) $P3_M$ and $P4_M$ resemble $S3_M$, whereas the latter has a gentler slope at fields higher than 130 mT. Although it appears noisy, the IRM acquisition curve of the carbonate fraction $P5_M$ is very steep in the interval of 40-110 mT, which is characteristic for a narrow magnetic grain-size range and might thus be at-

tributed to bacterial magnetite (Moskowitz et al. 1989; Kruiver and Passier 2001). We conclude that this component was not properly unmixed in the original EM unmixing of the IRM data, and hence, $S3_M$ corresponds to a mixture of bacterial magnetite and fluvial derived magnetic minerals. This phenomenon may be attributed to an association of marine bioproductivity and fluvial input, since during warm stages, both, the fluvial input and the bioproductivity is enhanced.

Gambia site GeoB 13602-1

Similarly as for the previously discussed core GeoB 9508-5, the elemental composition of $P1_E$ is similar to the $S1_E$ and $P2_E$ and $P3_E$ has elemental ratios similar to $S2_E$ (Table 4-1c, d). The carbonate fraction is mainly associated to Ca and to traces of Si, K and Fe.

When comparing the four P_M to the EMs obtained by Just et al. (Chap. 2), it appears that $P1_M$ is similar to $S1_M$ (Fig. 4-5e, f). The curve for the carbonate fraction $P4_M$ is similar to $S3_M$ pointing to an association of marine bioproductivity and the formation of bacterial magnetite. The shape of $P2_M$ and $P3_M$ are distinctively different from $S2_M$. The main difference exist at fields higher than 50 mT, where $P2_M$ and $P3_M$ are much steeper with respect to $S2_M$, indicating a higher content in ‘harder’ magnetite. At higher fields, this higher proportion of magnetite leads to a relative flattening of the $P2_M$ and $P3_M$ curves with respect to $S2_M$. We believe that this phenomenon is an expression of the non-

perfect correlation between carbonate fraction and bacterial magnetite and to an additional association of bacterial magnetite to fluvial input, as similarly hinted at for GeoB 9508-5. It remains however uncertain, if the contribution of bacterial magnetite is overestimated in the EM unmixing of the IRM acquisition curves, and a similar magnetite phase of fluvial material is unmixed into the ‘bacterial’ EM. Alternatively, this phenomenon may arise due to the fact that the production of bacterial magnetite is not solely controlled by the same processes as the production of carbonate. Furthermore, the preservation of bacterial magnetite in marine sediments is very sensitive for even slightly sulfidic conditions (e.g., Petersen et al. 1986). Thus, if dissolution of this magnetite phase occurred unequally over the record a possible primary association of carbonate and the correlation would be biased.

4.5.3 Differing signatures of terrigenous material off Gambia and Senegal

The geochemical composition of all dust EMs and respectively all fluvial EMs doesn’t vary significantly, no matter if obtained by the unmixing or the multi-proxy approach (Table 4-1). This indicates that specific environmental conditions in the source areas are not reflected in those data and that generic elemental ratios can be used as deterministic EMs for aeolian and fluvial material (Mulitza et al. 2010; Collins et al. 2011). In contrast, the magnetic mineralogy of identified EMs is much more variable. We

therefore focus in the following on the magnetic mineralogy.

Properties of aeolian material

The two dust EMs identified at the Senegal site (GeoB 9508-5) have differing magnetic mineralogies. $P1_M$ contains softer magnetite (coarser) with respect to $P2_M$ which might possibly be associated to gravitational sorting, since also the physical grain sizes $S1_G$ are coarser (Fig. 4-6). On the other hand, at higher fields this finer EM also contains a somewhat steeper IRM curve ($P2_M$), indicating a higher concentration of a high-coercivity magnetic phase. Lyons et al. (2010) found that high-coercivity minerals may be enriched within coarse sediments with respect to the fine fraction, i.e., hematite can appear as coatings on quartz grains. However, the grain sizes $S1_G$ (60 μm) and $S2_G$ (40 μm) are not that different and the elemental compositions do not indicate a higher concentration of quartz (similar Al/Si ratios). We therefore suggest that the higher concentration of high-coercivity minerals is not controlled by grain-size fractionation.

Also the comparison of the Gambia dust EM and the dust EMs at the Senegal site reveals differences. The dust deposited at the Gambia site ($P1_M$ of GeoB 13602-1, Fig. 4-6b) contains a higher concentration of coarse-grained magnetite with respect to the aeolian EMs $P1_M$ and $P2_M$ at the Senegal site. Likewise, the acquisition curves of the end-member unmixing of the IRM show the same pattern (Fig. 4-6c).

We conclude that all aeolian EMs originate

from different source regions. Due to the coarse grain sizes, Just et al. (Chap. 3) inferred that the aeolian EM in GeoB 13602-1 (Gambia) corresponds to a proximal dust source. Likewise, we suggest that the coarsest aeolian EM of GeoB 9508-5 (Senegal) with its coarse magnetite phase ($P1_M$) corresponds to a proximal dust source, which is dominant during extremely dry HSs. Most probably, the coarse dust phases in both cores are transported by strong trade winds during HSs (e.g., Hooghiemstra et al. 2006) from proximal sources, since at these times the arid conditions made additional areas available for

aeolian deflation. The finer dust most likely corresponds to a ‘background dust component’ as its contribution is relatively stable during HSs. It either represents dust exported by lower wind strength or corresponds to a more distal source. For the latter scenario it might be hypothesized that the finer aeolian EM corresponds to material transported by the AEJ.

When comparing the contribution of the proximal dust from Senegal (this study) and the Gambia sites (Just et al. Chap. 3), it appears that its proportion in the latter cores is only strongly enhanced during HS 1 and HS 4 while in the

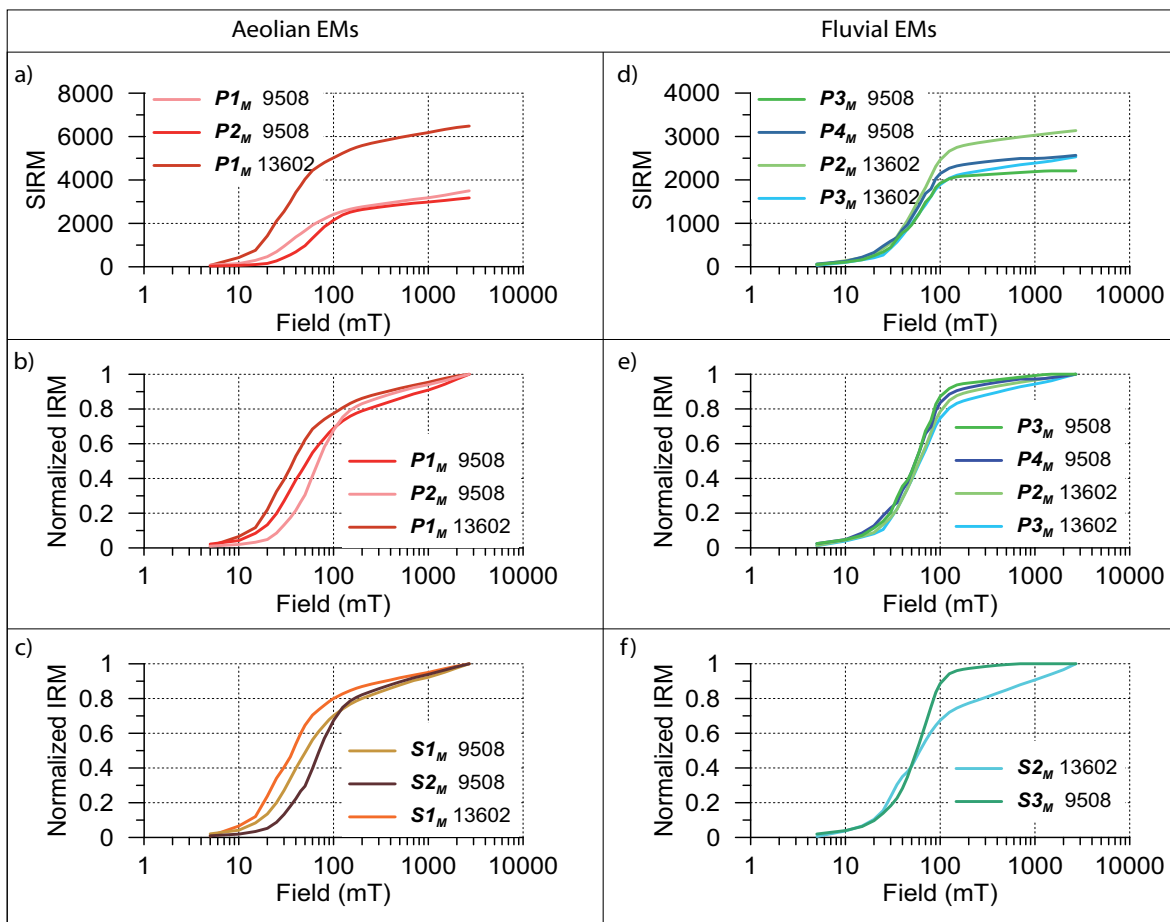


Fig. 4-6: (a, b) Comparison of the predicted IRM acquisition curves (P_M) of the aeolian EMs of both cores and (c) the IRM acquisition curves from EM unmixing (S_M). (d, e) Comparison of the predicted IRM acquisition curves (P_M) of the fluvial EMs of both cores and (f) the IRM acquisition curves from EM unmixing (S_M).

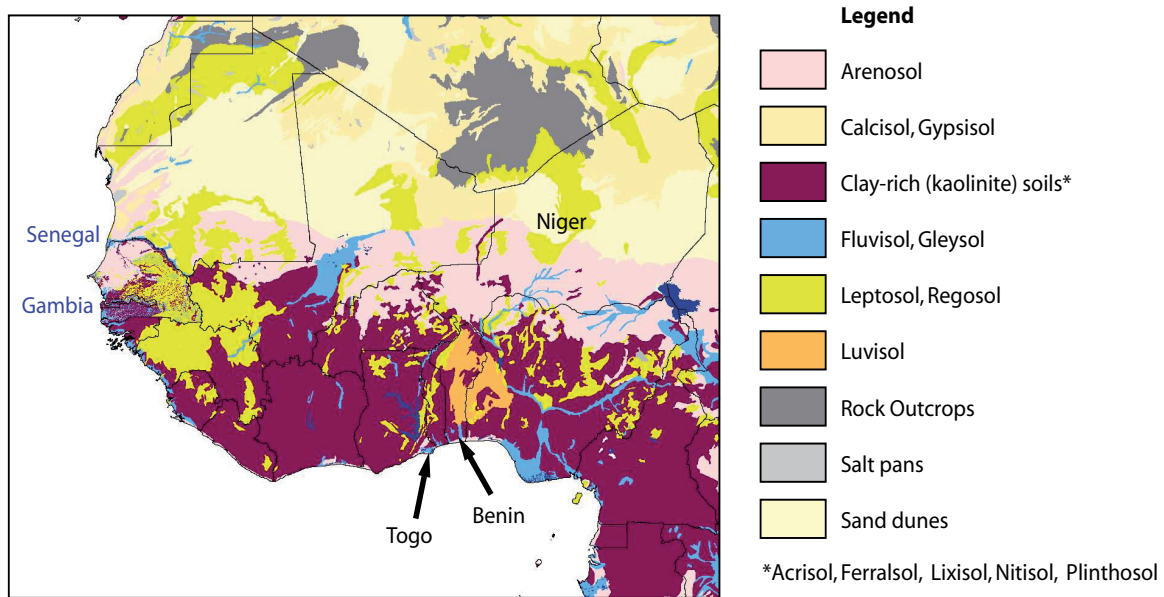


Fig. 4-7: Soil distribution in West Africa (data from *Harmonized Soils World Database* (2009), modified). The soils studied by Lyons et al. (2010) are similar to the soils in the Senegal (Arenosols) and Gambia (clay-rich soils) River basins. In Niger, mainly Arenosols are present, while Benin and Togo are characterized by clay-rich soils.

Senegal core, coarse dust has also a strong volume contribution during HS 2. This finding is in-line with observations of Itambi et al. (2009) and Collins et al. (in prep.), who observed that the ‘dusty’ signal diminishes when moving from subtropical to tropical Africa.

Properties of fluvial material

Besides the uncertainties concerning a possible contribution of bacterial magnetite mingled with the fluvial EM signature, we believe that a tendency between the magnetic inventory of the fluvial EMs at the Senegal and Gambia core locations is apparent. The properties reveal that at the Senegal core location the fluvial EM has a higher concentration of low-coercivity magnetic minerals (i.e., magnetite) with respect to the Gambia EM, which in turn contains a higher proportion of high-coercivity minerals (goethite,

hematite). In the proximity to the coast, the Senegal mainly drains sandy substrates (i.e., Arenosols) which mostly lack soil horizon formation. In contrast, the Gambia flows through clay rich soils (Fig. 4-1b). It is therefore reasonable that pedogenically formed high-coercivity minerals are enriched within these mature soils. This assumption is supported by a study carried out on soil and sand samples from the African continent (Lyons et al. 2010). Magnetic parameters measured on specific grain-size fractions of soil and sand samples show a dependency of pedogenically formed minerals on precipitation. The proportion of high-coercivity with respect to low-coercivity magnetic minerals is higher for areas of stronger precipitation. In soil samples from Togo and Benin HIRM accounts for 10 – 16.7 % of SIRM, while the respective proportion is 1.5 – 4.5 % for samples from Niger. The

substrates in Niger mainly correspond to Arenosols and sand dunes while Togo and Benin are dominated by Luvisols (mixed clay accumulation below a layer of humus and a leached horizon) and a group of clay-rich soils (Fig. 4-7). We therefore assume that observed differences in the Gambia and Senegal River EMs can be attributed to the same phenomenon. Since these differences are absent in the geochemical properties of the fluvial EMs, it may be hypothesized that magnetic minerals are more susceptible for reflecting soil forming processes than the geochemical composition.

4.6. Conclusion

The multi-proxy investigation revealed that grain-size EMs obey specific magnetic and geochemical signatures. The magnetic mineralogy enabled us to distinguish three different aeolian EMs of different provenance. The contribution of coarse proximal dust in each core is particularly high during HSs and is strongest in the northern core. The fine aeolian EM is only detected at the northern core site off the Senegal River and corresponds to a distant dust source. This fraction corresponds probably to material transported by the AEJ. To further evaluate the spatial distribution of dust with the same characteristics, and consequently derived from the same source areas, the prosperous approach used in this study should be applied on more cores off NW Africa.

We found that in our study area bacterial mag-

netite seems to be associated to the carbonate fraction and fluvial input, and thus marine productivity and humidity. This association biases the magnetic signal of the fluvial EMs. However, a trend of higher proportion of high-coercivity magnetic minerals in the Gambia River EM is apparent. It is reasonable that the occurrence of pedogenically high-coercivity minerals indicate the higher maturation of the soils in the Gambia catchment than the soils of the Senegal River basin.

In conclusion, we suggest that by the investigation of grain sizes, geochemical composition, and magnetic mineralogy a three level interpretation of sediments from different sources may be drawn. Grain sizes reflect the transport energy and, thus, the wind strength and fluvial runoff. Elemental ratios display generic characteristics of fluvial and aeolian sediments. Finally, magnetic properties are influenced by more regional environmental conditions such as weathering and soil formation.

Acknowledgments

We thank the crew and scientific party of *Maria S. Merian* cruise MSM 11/2 and *Meteor* cruise M65/1. This research was funded by the Deutsche Forschungsgemeinschaft (DFG) through the European Graduate College EUROPROX and MARUM Center for Marine Environmental Science.

References

- Bloemendal, J., King, J.W., Hall, F.R. and Doh, S.J., 1992. Rock Magnetism of Late Neogene and Pleistocene deep-sea sediments: Relationship to sediment source, diagenetic processes, and sediment lithology. *J. Geophys. Res.*, 97: 4361-4375.
- Caquineau, S., Gaudichet, A., Gomes, L., Magonthier, M.-C. and Chatenet, B., 1998. Saharan dust: Clay ratio as a relevant tracer to assess the origin of soil derived aerosols. *Geophys. Res. Lett.*, 25(7): 983-986.
- Chiapello, I. Bergametti, G., Chatenet, B., Bousquet, P., Dulac, F., Soares, E. S., 1997. Origins of African dust transported over the northeastern tropical Atlantic. *J. Geophys. Res.*, 102(D12): 13701-13709.
- Collins, J.A., Mulitza, S., Heslop, D., Zabel, M., Govin, A., Hartmann, J., Röhl, U., Wefer G., in prep. Southward shift of Saharan dune fields during Heinrich Stadials.
- Collins, J.A. Schefuß, E., Heslop, D., Mulitza, S., Prange, M., Zabel, M., Tjallingii, R., Dokken, T. M., Huang, E., Mackensen, A., Schulz, M., Tian, J., Zarriess, M., Wefer, G., 2011. Interhemispheric symmetry of the tropical African rainbelt over the past 23,000 years. *Nature Geosci.*, 4(1): 42-45.
- Dinarès-Turell, J., Hoogakker, B.A.A., Roberts, A.P., Rohling, E.J. and Sagnotti, L., 2003. Quaternary climatic control of biogenic magnetite production and eolian dust input in cores from the Mediterranean Sea. *Palaeogeogr., Palaeoclimat., Palaeoecol.*, 190: 195-209.
- Eyre, J., 1996. The application of high resolution IRM acquisition to the discrimination of remanence carriers in Chinese loess. *Stud. Geophys. Geodæt.*, 40(3): 234-242.
- FAO/IIASA/ISRIC/ISSCAS/JRC, 2009. Harmonized World Soil Database (version 1.1). In: FAO (Ed.), Rome, Italy and IIASA, Laxenburg, Austria.
- Frank, U. and Nowaczyk, N.R., 2008. Mineral magnetic properties of artificial samples systematically mixed from haematite and magnetite. *Geophysical Journal International*, 175(2): 449-461.
- Frederichs, T., Bleil, U., Däumler, K., von Dobeneck, T. and Schmidt, A. (Eds.), 1999. The magnetic view on the marine paleoenvironment: Parameters, techniques and potentials of rock magnetic studies as a key to paleoclimatic and paleoceanographic changes. Use of Proxies in Paleoceanography: Examples from the South Atlantic. Springer, Berlin, Heidelberg.
- Gac, J.Y. and Kane, A., 1986. Le fleuve Sénégal: I Bilan hydrologique et flux continentaux der matières particulaires a l'embouchure. *Sci. Geol. Bull.*, 39(1): 99-130.
- Harris, S.E. and Mix, A.C., 1999. Pleistocene precipitation balance in the Amazon basin recorded in deep sea sediments. *Quat. Res.*, 51(1): 14-26.
- Heslop, D., 2009. On the statistical analysis of the rock magnetic S-ratio. *Geophys. J. Int.*, 178(1): 159-161.
- Heslop, D. and Dillon, M., 2007. Unmixing magnetic remanence curves without a priori knowledge. *Geophys. J. Intl.*, 170(2): 556-566.
- Hesse, P.P., 1994. Evidence for bacterial palaeoecological origin of mineral magnetic cycles in oxic and sub-oxic Tasman Sea sediments. *Mar. Geol.*, 117(1-4): 1-17.
- Hilgenfeldt, K., 2000. Diagenetic dissolution of biogenic magnetite in surface sediments of the Benguela upwelling system. *Int. J. Earth Sci.*, 88(4): 630-640.
- Hooghiemstra, H., Lézine, A.-M., Leroy, S.A.G., Dupont, L. and Marret, F., 2006. Late Quaternary palynology in marine sediments: A synthesis of the understanding of pollen distribution patterns in the NW African setting. *Quat. Int.*, 148(1): 29-44.
- Housen, B.A. and Moskowitz, B.M., 2006. Depth distribution of magnetofossils in near-surface sediments from the Blake/Bahama Outer Ridge, western North Atlantic Ocean, determined by low-temperature magnetism. *J. Geophys. Res.*, 111(G1): G01005.
- Itambi, A.C., von Dobeneck, T., Mulitza, S., Bickert, T. and Heslop, D., 2009. Millennial-scale northwest African droughts related to Heinrich events and Dansgaard-Oeschger cycles: Evidence in marine sediments from offshore Senegal. *Paleoceanography*, 24: PA1205.
- Just, J., Dekkers, M.J., von Dobeneck, T., van Hoesel, A. and Bickert, T., Chap. 2. Unmixing signatures of eolian, fluvial, bacterial and diagenetic magnetic mineral fractions in Late Quaternary marine sediments off Gambia, NW Africa.
- Just, J., Heslop, D., von Dobeneck, T., Bickert, T., Dekkers, M., Frederichs, T., Meyer, I., Zabel, M., Chap. 3. Multi-proxy characterization of terrigenous end-members off NW Africa.
- Kämpf, N. and Schwertmann, U., 1983. Goethite and hematite in a climosequence in southern Brazil and their application in classification of kaolinitic soils. *Geoderma*, 29(1): 27-39.
- King, J., Banerjee, S.K., Marvin, J. and Özdemir, Ö., 1982. A comparison of different magnetic methods for determining the relative grain size of magnetite in natural materials: Some results from lake sediments. *Earth Planet. Sci. Lett.*, 59(2): 404-419.
- Kirschvink, J.L. and Chang, S.-B.R., 1984. Ultrafine-grained magnetite in deep-sea sediments: Possible bacterial magnetofossils. *Geology*, 12(9): 559-

- 562.
- Koopmann, B., 1981. Sedimentation von Saharastaub im subtropischen Nordatlantik während der letzten 25.000 Jahre. *Meteor Forschungs-Ergebnisse*, 35: 23-59.
- Kruiver, P.P. and Passier, H., 2001. Coercivity analysis of magnetic phases in sapropel S1 related to variations in redox conditions, including an investigation of the S ratio. *Geochem. Geophys. Geosyst.*, 2(12).
- Lean, C.M.B. and McCave, I.N., 1998. Glacial to interglacial mineral magnetic and palaeoceanographic changes at Chatham Rise, SW Pacific Ocean. *Earth Planet. Sci. Lett.*, 163(1-4): 247-260.
- Lyons, R., Oldfield, F. and Williams, E., 2010. Mineral magnetic properties of surface soils and sands across four North African transects and links to climatic gradients. *Geochem. Geophys. Geosyst.*, 11: Q08023.
- Maher, B.A., 1986. Characterisation of soils by mineral magnetic measurements. *Phys Earth Planet. Inter.*, 42(1-2): 76-92.
- Matthewson, A.P., Shimmield, G.B., Kroon, D. and Fallick, A.E., 1995. A 300 kyr High-Resolution Aridity Record of the North African Continent. *Paleoceanography*, 10(3): 677-692.
- Moreno, T., Querol, X., Castillo, S., Alastuey, A., Cuevas, E., Herrmann, L., Mounkaila, M., Elvira, J., Gibbons, W., 2006. Geochemical variations in aeolian mineral particles from the Sahara-Sahel Dust Corridor. *Chemosphere*, 65(2): 261-270.
- Moskowitz, B.M., Frankel, R.B., Bazylinski, D.A., Janasch, H.W. and Lovley, D.R., 1989. A comparison of magnetite particles produced anaerobically by magnetotactic and dissimilatory iron-reducing bacteria. *Geophys. Res. Lett.*, 16(7): 665-668.
- Mulitza, S. et al., 2010. Increase in African dust flux at the onset of commercial agriculture in the Sahel region. *Nature*, 466(7303): 226-228.
- Mulitza, S. et al., 2008. Sahel megadroughts triggered by glacial slowdowns of Atlantic meridional overturning. *Paleoceanography*, 23(4): PA4206.
- Peters, C. and Dekkers, M.J., 2003. Selected room temperature magnetic parameters as a function of mineralogy, concentration and grain size. *Phys. Chem. Earth*, 28(16-19): 659-667.
- Petersen, N., von Dobeneck, T. and Vali, H., 1986. Fossil bacterial magnetite in deep-sea sediments from the South Atlantic Ocean. *Nature*, 320(6063): 611-615.
- Prospero, J.M. and Carlson, T.N., 1980. Saharan air outbreaks over the tropical North Atlantic. *Pure Appl. Geophys.*, 119(3): 677-691.
- Pye, K., 1987. *Aeolian dust and dust deposits*. Academic press, London, 334 pp.
- Roberts, A.P., Florindo, F., Villa, G., Chang, L., Jovane, L., Bohaty, S. M. Larrasoana, J. C., Heslop, D., Fitz Gerald, J. D., 2011. Magnetotactic bacterial abundance in pelagic marine environments is limited by organic carbon flux and availability of dissolved iron. *Earth Planet. Sci. Lett.*, 310(3-4): 441-452.
- Sarnthein, M., et al., Fundamental modes and abrupt changes in North Atlantic circulation and climate over the last 60 ky—Concepts, reconstructions and numerical modeling, in *The Northern North Atlantic: A Changing Environment*, edited by P. Schäfer et al., pp. 365–410, Springer-Verlag, New York, 2001.
- Schwertmann, U. and Taylor, R.M., 1989. *Iron Oxides. Minerals in Soil Environments*. Soil Science Society of America Inc. (SSSA). Madison, USA.
- Shackleton, N.J., Fairbanks, R.G., Chiu, T.-c. and Parenin, F., 2004. Absolute calibration of the Greenland time scale: implications for Antarctic time scales and for $[\Delta]14C$. *Quat. Sci. Rev.*, 23(14-15): 1513-1522.
- Shackleton, N.J., Hall, M.A. and Vincent, E., 2000. Phase relationships between millennial-scale events 64,000-24,000 years ago. *Paleoceanography*, 15(6): 565-569.
- Stolz, J.F., Chang, S.-B.R. and Kirschvink, J.L., 1986. Magnetotactic bacteria and single-domain magnetite in hemipelagic sediments. *Nature*, 321(6073): 849-851.
- Stoner, J.S., Channell, J.E.T. and Hillaire-Marcel, C., 1996. The magnetic signature of rapidly deposited detrital layers from the Deep Labrador Sea: Relationship to North Atlantic Heinrich layers. *Paleoceanography*, 11(3): 309-325.
- Stuut, J.-B. Zabel, M., Ratmeyer, V., Helmke, P., Scheuß, E., Lavik, Gaute, 2005. Provenance of present-day aeolian dust collected off NW Africa. *J. Geophys. Res.*, 110: D04202.
- Weltje, G., 1997. End-member modeling of compositional data: Numerical-statistical algorithms for solving the explicit mixing problem. *Math. Geol.*, 29(4): 503-549.
- White, F., 1983. *A Descriptive Memoir to Accompany the UNESCO/AETFAT/UNSO Vegetation Map of Africa*. United Nations Educational, Scientific, and Cultural Organization, Paris.
- Zabel, M., Schneider, R. R., Wagner, T., Adegbe, A. T. de Vries, U., Kolonic, S., 2001. Late Quaternary Climate Changes in Central Africa as Inferred from Terrigenous Input to the Niger Fan. *Quat. Res.*, 56(2): 207-217.
- Zhang, Y.G., Ji, J., Balsam, W.L., Liu, L. and Chen, J., 2007. High resolution hematite and goethite records from ODP 1143, South China Sea: Co-evolution of monsoonal precipitation and El Niño over the past 600,000 years. *Earth Planet. Sci. Lett.*, 264(1-2): 136-150.

5. Synthesis

Principle aims of this thesis were to extend and to evaluate the applicability, reliability and interpretability of multi-proxy end-member (EM) methods for a quantitative analysis of NW African terrigenous sediments. The variability of the EM solutions was tested on a regional scale to identify fundamental properties of fluvial and aeolian sediments as well as source- and climate-specific variations. The parameters that were investigated are grain-size distributions, major element composition, grain-size distribution and the magnetic mineralogy of marine sediments retrieved off the Gambia and Senegal Rivers.

5.1 Grain-size distribution

As revealed by the multi-proxy studies (Chapter 3 and 4), grain-size EMs are valuable for reconstructing sediment fractions transported under differing energetic conditions. For budgeting of fluxes, the volumetric contributions of grain-size EMs are essential. However, the physical grain sizes do not permit a source characterization of the material, and thus are not capable for delivering information about the environmental conditions in the potential source areas. The distance between the source area and the sampling site has an impact on the grain-size distribution of the accumulated material, since the particles

are subject to gravitational sorting. For aeolian material, the grain-size distribution depends on the transport energy and the distance to the source area. The grain sizes of fluvial material are controlled primarily by the distance between the river mouth and the study site and therefore by sea-level fluctuations. Additionally, the water discharge and thus precipitation in the catchment basin also influences the grain sizes of the accumulated sediments since coarse grains are potentially transported farther out at sea during high water discharge.

5.2 Major element composition

Specific elemental ratios typical for fluvial and aeolian material resemble the geochemical composition of element EMs at the study sites (Chapter 3 and 4). Elemental ratios of fluvial and aeolian sediments are mainly controlled by two factors: (1) Because of chemical weathering, Al and Fe are enriched in tropical soils (Middelburg et al. 1988; Driessen et al. 2001) and, accordingly, in fluvial sediments of tropical climates. (2) Since the particles transported by rivers are finer than aeolian material off NW Africa, the concentration of clay aggregates is higher with respect to quartz grains. Consequently, based on the elemental composition it is possible to distinguish sediments of distinct provenance when

they are derived from source areas of contrasting environmental conditions. Furthermore, such a distinction is even amplified, when physical transport mechanisms differ.

5.3 Magnetic mineralogy

The inventory of pedogenically formed magnetic minerals is - similar to the geochemical composition - dependent on the environmental conditions. The formation of hematite is favored in relatively dry highly oxidized soils under elevated temperatures, while goethite is formed in moister usually well-drained soils (Kämpf and Schwertmann 1983; Maher 1986). The magnetic mineralogy of fluvial and aeolian EMs at our two study sites is distinctively different. At the Senegal sites two aeolian EMs were indentified (Chapter 4), which differ in the concentration of magnetite and in the proportion of high-coercivity (goethite and hematite) magnetic minerals. Off the Gambia River, only one aeolian EM was unraveled (Chapter 2). It contains a higher proportion of coarse-grained magnetite with respect to the aeolian EMs off the Senegal River. These differences suggest that the dust, accumulated at both sites, is derived from different source regions.

Similarly, the magnetic inventory of the fluvial EMs at both core positions shows distinct differences. Off the Gambia, the material has a higher concentration of goethite and hematite with respect to the material off the Senegal River. At present, the Senegal River drains Arenosols in

the proximity of the coast. These sandy highly leached soils are depleted in clay minerals. In contrast, in the Gambia basin mature clay-rich soils are present. Although the paleosoil distribution is not known, it is reasonable that the higher content of goethite (and hematite) in the fluvial material off Gambia most likely reflects the differences in the maturity of the soils in the catchments.

5.4 Multi-proxy characteristics

Since the investigated properties of terrigenous sediments are influenced by different factors, the multi-proxy characteristics of terrigenous EMs enable a three-level interpretation.

- (1) The grain-sizes of the terrigenous sediments reflect the transport energy.
- (2) The geochemical composition allows a general differentiation of fluvial and aeolian sediments.
- (3) The magnetic mineralogy mirrors the degree of weathering of the soils and thus environmental conditions in the source areas.

Differing weathering conditions in the Senegal and Gambia River basins suggested by the magnetic mineralogy do not emerge from the elemental composition of the fluvial EMs. However, present day suspension samples of both rivers, have likewise similar major element compositions, but can be distinguished by the content of smectite and interlayered clay minerals (Gac et al. 1987). It may be hypothesized, that differ-

ences in the magnetic mineralogy of the river material is more susceptible to soil conditions, since also pH and organic matter content influence the formation (Kämpf and Schwertmann 1983). Most likely, the clay mineralogy would also reveal differences of the fluvial EMs of both cores.

5.5 Paleoclimatic implications revealed by end-member analyses

At both study sites the volumetric fractions of fluvial and aeolian sediments varies significantly over the records. The accumulation of fluvial material delivered by the Gambia River is mainly controlled by the core-to-shore distance, i.e., by sea-level variations. During periods of sea-level stagnancy, the precipitation in the hinterland appears to have an impact on the accumulation and grain-size distribution of the fluvial sediments.

In both cores proximal dust EMs were identified, whose volume fractions are high during the Last Glacial Maximum (LGM) and Heinrich Stadials (HS), with respect to the fluvial EMs. At the Senegal site, all HSs have high contributions of the aeolian EM, while at the southern Gambia site HS 1 is by far the most pronounced. At the Senegal location an additional dust EM was identified, which has the same elemental composition as the coarse dust, but is finer in grain-size and has a different magnetic mineralogy. The volumetric proportion of this finer aeolian component remains relatively stable throughout the record, and it is assumed that it corresponds

to a background dust EM from a more distant source. This material was probably transported by the African Easterly Jet.

Budgeting fluxes of the terrigenous EMs over the past 70 ka was carried out on the Gambia site material (Chap. 3). During the LGM, dust fluxes were ~ 5 times higher with respect to the Late Holocene. These values are in accordance to modeling approaches (Mahowald et al. 2006) and studies of marine core material (Kohfeld and Harrison 2001). Even higher dust input accompanied HSs, when dust fluxes were ~ 8 -35 times higher compared to the present. Extremely high dust accumulation of $400 \text{ g m}^{-2} \text{ yr}^{-1}$ occurred during HS 1, which is 100 times higher than at present.

During the LGM and HS 1 low-latitude Africa experienced much drier conditions (Williams 1975; Street and Grove 1976; Collins et al. 2011). The dry conditions on the continent during the LGM and HSs appear to correspond to a southward displacement of the ITCZ due to cooler temperatures in the North Atlantic (Street-Perrott and Perrott 1990; Chiang and Bitz 2005; Dahl et al. 2005). For the African continent this resulted in contraction of the rainbelt, and thus a southward expansion of the desert (Collins et al. 2011). Collins et al. (2011) observed that the proportion of aeolian with respect to fluvial material during HS 1 and the LGM decreases when moving from North to tropical Africa. The fact that HSs are less pronounced at the southern Gambia than at the Senegal site supports such a scenario. Moreover, the comparable intensity of

HS 1 at both study sites suggests that the aridification reached farther south at this time, with respect to the previous HSs. Notably, HS 3 is the least pronounced in both records. Evidence from the ice rafted detritus (IRD) components in the North Atlantic revealed a different source of material for Heinrich Layer 3 (Gwiazda et al. 1996). The effect of fresh-water input on the deep water formation is mainly controlled by the transport of meltwater to the convection site than by the amount of meltwater (Seidov and Maslin 1999). It is suggested that the meridional overturning circulation recovered more rapidly after HS 3, compared to the other HSs (Elliot et al. 2002). The weak expression of HS 3 in our records is probably attributed to this phenomenon.

During the Holocene dust accumulation was strongly reduced. However, also the fluvial input was much lower which is attributed to the sea-level rise after the last deglaciation and consequently increasing core-to-shore distance. This latter finding strongly suggests that sea-level induced changes in fluvial sediment supply must be evaluated when using relative proportions of the aeolian and fluvial fractions for paleoclimatic reconstructions.

References

- Chiang, J. and Bitz, C., 2005. Influence of high latitude ice cover on the marine Intertropical Convergence Zone. *Clim. Dyn.*, 25(5): 477-496.
- Collins, J.A. et al., 2011. Interhemispheric symmetry of the tropical African rainbelt over the past 23,000 years. *Nature Geosci.*, 4(1): 42-45.
- Dahl, K.A., Broccoli, A.J. and Stouffer, R.J., 2005. Assessing the role of North Atlantic freshwater forcing in millennial scale climate variability: a tropical Atlantic perspective. *Clim. Dyn.*, 24(4): 325-346.
- Driessen, P.M. et al., 2001. Lecture notes on the major soils of the world. Food and Agriculture Organization of the United Nations, Rome.
- Elliot, M., Labeyrie, L. and Duplessy, J.-C., 2002. Changes in North Atlantic deep-water formation associated with the Dansgaard-Oeschger temperature oscillations (60–10 ka). *Quat. Sci. Rev.*, 21(10): 1153-1165.
- Gac, J.-Y. et al., 1987. *Géochimie des eaux du Fouta-Djalon : flux dissous et particulaires en Haute Gambie (Kédougou et Gouloumbou) : contribution à la monographie de la Gambie*, ORSTOM, Montpellier.
- Gwiazda, R.H., Hemming, S.R. and Broecker, W.S., 1996. Provenance of icebergs during heinrich event 3 and the contrast to their sources during other heinrich episodes. *Paleoceanography*, 11(4): 371-378.
- Kämpf, N. and Schwertmann, U., 1983. Goethite and hematite in a climosequence in southern Brazil and their application in classification of kaolinitic soils. *Geoderma*, 29(1): 27-39.
- Kohfeld, K.E. and Harrison, S.P., 2001. DIRTMAP: the geological record of dust. *Earth Sci. Rev.*, 54(1-3): 81-114.
- Maher, B.A., 1986. Characterisation of soils by mineral magnetic measurements. *Phys. Earth Planet. Inter.*, 42(1-2): 76-92.
- Mahowald, N.M. et al., 2006. Change in atmospheric mineral aerosols in response to climate: Last glacial period, preindustrial, modern, and doubled carbon dioxide climates. *J. Geophys. Res.*, 111(D10): D10202.
- Middelburg, J.J., van der Weijden, C.H. and Woitiez, J.R.W., 1988. Chemical processes affecting the mobility of major, minor and trace elements during weathering of granitic rocks. *Chem. Geol.*, 68(3-4): 253-273.
- Seidov, D. and Maslin, M., 1999. North Atlantic deep water circulation collapse during Heinrich events. *Geology*, 27(1): 23-26.
- Street-Perrott, F.A. and Perrott, R.A., 1990. Abrupt climate fluctuations in the tropics: the influence of Atlantic Ocean circulation. *Nature*, 343(6259): 607-612.
- Street, F.A. and Grove, A.T., 1976. Environmental and climatic implications of late Quaternary lake-level fluctuations in Africa. *Nature*, 261(5559): 385-390.
- Williams, M.A.J., 1975. Late Pleistocene tropical aridity synchronous in both hemispheres? *Nature*, 253(5493): 617-618.

Geo-Mar Lett
DOI 10.1007/s00367-010-0213-z

ORIGINAL

Erosion of continental margins in the Western Mediterranean due to sea-level stagnancy during the Messinian Salinity Crisis

Janna Just · Christian Hübscher · Christian Betzler ·
Thomas Lüdmann · Klaus Reicherter

Received: 13 October 2009 / Accepted: 23 June 2010
© Springer-Verlag 2010

Abstract High-resolution multi-channel seismic data from continental slopes with minor sediment input off southwest Mallorca Island, the Bay of Oran (Algeria) and the Alboran Ridge reveal evidence that the Messinian erosional surface is terraced at an almost constant depth interval between 320 and 380 m below present-day sea level. It is proposed that these several hundred- to 2,000-m-wide terraces were eroded contemporaneously and essentially at the same depth. Present-day differences in these depths result from subsidence or uplift in the individual realms. The terraces are thought to have evolved during one or multiple periods of sea-level stagnancy in the Western Mediterranean Basin. According to several published scenarios, a single or multiple periods of relative sea-level stillstand occurred during the Messinian desiccation event, generally known as

the Messinian Salinity Crisis. Some authors suggest that the stagnancy started during the refilling phase of the Mediterranean basins. When the rising sea level reached the height of the Sicily Sill, the water spilled over this swell into the eastern basin. The stagnancy persisted until sea level in the eastern basin caught up with the western Mediterranean water level. Other authors assigned periods of sea-level stagnancy to drawdown phases, when inflowing waters from the Atlantic kept the western sea level constant at the depth of the Sicily Sill. Our findings corroborate all those Messinian sea-level reconstructions, forwarding that a single or multiple sea-level stagnancies at the depth of the Sicily Sill lasted long enough to significantly erode the upper slope. Our data also have implications for the ongoing debate of the palaeo-depth of the Sicily Sill. Since the Mallorcan plateau experienced the least vertical movement, the observed terrace depth of 380 m there is inferred to be close to the Messinian depth of this swell.

J. Just (✉) · C. Hübscher
Institute of Geophysics, University of Hamburg,
20146 Hamburg, Germany
e-mail: janna.just@uni-bremen.de

C. Betzler
Institute for Geology and Paleontology, University of Hamburg,
20146 Hamburg, Germany

T. Lüdmann
Institute of Biogeochemistry and Marine Chemistry,
University of Hamburg,
20146 Hamburg, Germany


K. Reicherter
Department of Neotectonics and Natural Hazards, RWTH,
52056 Aachen, Germany

Present Address:
J. Just
Faculty of Geosciences, University of Bremen,
Klagenfurter Strasse,
28359 Bremen, Germany

Introduction

During the Messinian, tectonic uplift caused the closure of the Mediterranean–Atlantic connection, which consisted of several gateways in southern Spain and northern Africa (Esteban et al. 1996). The Iberian corridors became restricted prior to the Messinian (Martín et al. 2001; Betzler et al. 2006). The closure of the African gateways caused a substantial sea-level drop within the entire Mediterranean basin, triggering the Messinian Salinity Crisis (MSC; Hsü et al. 1973; Ryan and Cita 1978; CIESM 2008; Ryan 2009). The resulting sub-aerial exposure caused massive erosion of the continental slopes (Rizzini et al. 1978; Clauzon et al. 1996; Lofi et al. 2005; Sage et al. 2005; Bertoni and Cartwright 2006, 2007; Maillard et al. 2006). The sea-level

Published online: 15 July 2010

 Springer

fall further resulted in an increased salinity of Mediterranean water and in the precipitation of evaporites. An overview of various models regarding the timing, duration and degree of sea-level fluctuations during the MSC has recently been presented by CIESM (2008). Notably, basinal evaporites up to some km in thickness have been intensely studied by means of seismic reflection surveys, revealing differences west and east of the Sicily Strait (Fig. 1; see below). Based on individual water budgets for the basins, it has been speculated that, during the MSC, the western and eastern basins became separated at the Sicily Sill, located southwest of Sicily.

Because the Sicily Sill is located in the southern part of the Apennines-Calabrian arc (e.g. Dewey et al. 1989; Gueguen et al. 1998; Gelabert et al. 2002), a tectonically active zone, its depth cannot be precisely reconstructed with available data. Nevertheless, Blanc (2006) demonstrated that the timing of accumulation of evaporites in the western and eastern basins is directly linked to the depth position of this swell. During an early phase of the MSC, the western basin water level supposedly reached the sill's top, and the

water level remained constant for some thousand years in this basin, while inflowing water from the Atlantic was bypassed from the western to the eastern basin.

Alternatively, numerical simulations of Messinian sea-level fluctuations by Meijer and Krijgsman (2005) and Gargani and Rigollet (2007) showed that, from the time of sea-level drop below the Sicily Sill, the two basins evolved individually. Later, during the reflooding stage (Zanclean flood) of the Mediterranean Sea, the western basin was filled first until the height of the sill was reached (Meijer and Krijgsman 2005). Afterwards, the water spilled over the sill into the eastern basin, where sea level started to rise. The assumption underlying the model of Meijer and Krijgsman (2005) was that the inflow rate of Atlantic water into the Mediterranean Sea equalled that of the present day. This means that the geometry of the Gibraltar Strait would have been the same as today. Furthermore, the depth of the Sicily Sill was assumed to have been 300 m relative to global sea level (i.e. equal to its present-day depth). However, neither the inflow nor the depth of the sill are precisely known. Accepting the assumptions of Meijer and

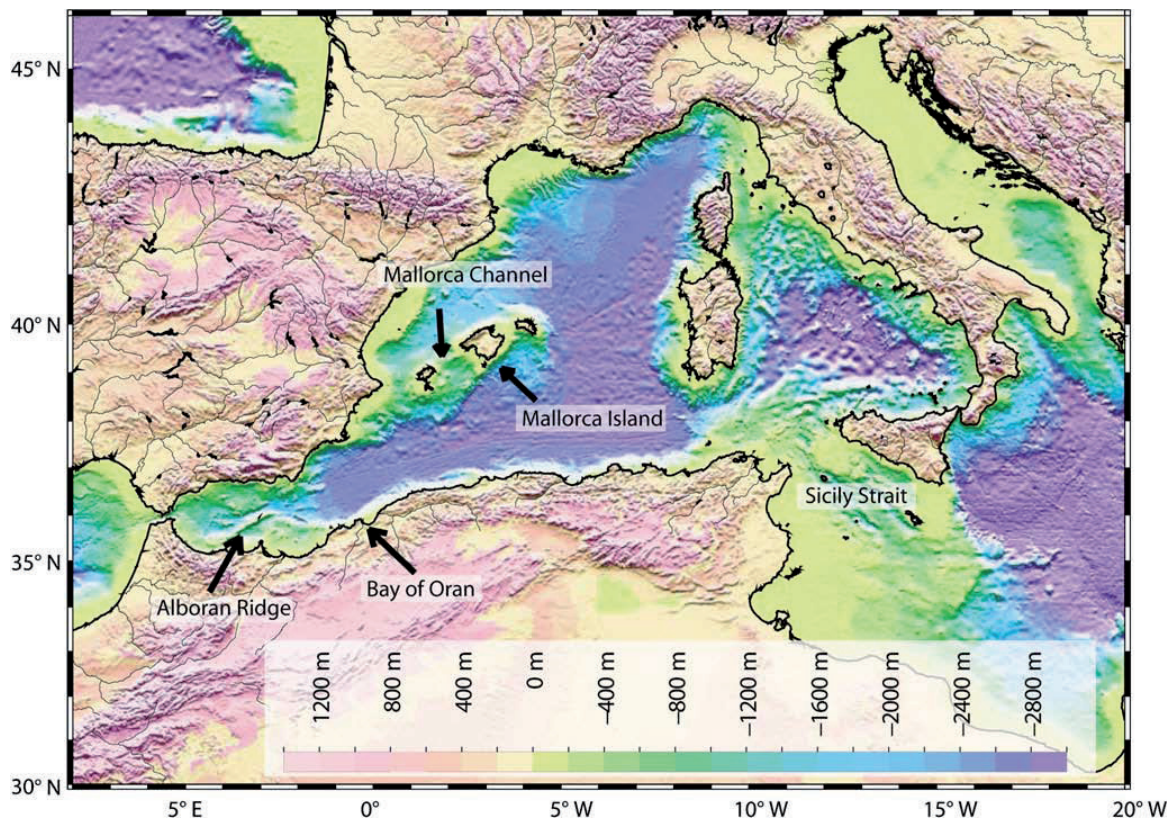


Fig. 1 Bathymetric map of the Western Mediterranean basin, with the study areas indicated by *arrows* (GEBCO One Minute Grid). The western and eastern basins are separated by the Strait of Sicily

Krijgsman (2005), the bypass period of western Mediterranean waters flowing into the eastern basin would have lasted for some thousands of years, until sea level in the eastern basin reached the height of the Sicily Sill. During this time interval, sea level in the western basin would have remained constant (Meijer and Krijgsman 2005; Fig. 2). However, by examining the scenario for a wider and deeper Gibraltar Strait geometry, and the resulting higher inflow rate, Meijer and Krijgsman state that the refilling of the Mediterranean could have been completed much faster. According to Gargani and Rigollet (2007), repeated sea-level fluctuations occurred during the MSC. It can be hypothesized that recurring sea-level stagnancy at the height of the Sicily Sill accompanied each refilling phase.

Blanc (2002) modelled the Zanclean flood in terms of erosional mechanisms at the gateway between the Atlantic and Mediterranean, proposing that a change in geometry due to erosion resulted in increased inflow rates and flow velocities and, consequently, a much faster (11 years) refilling of the Mediterranean. Recently, Garcia-Castellanos et al. (2009) observed erosive channels in the subsurface west and east of the Gibraltar Strait, based on seismic and well data. They concluded that these channels are interconnected and that they were eroded during the terminal flooding of the Mediterranean, and calculated dramatically high inflow rates and velocities at the Gibraltar Strait. The refilling of the western basin would have occurred within 500 days until the height of the Sicily Sill was reached, followed by a 300-day overflow phase into the eastern basin and another 150 days until complete refilling of the entire Mediterranean.

Sea-level stillstands are inherent to both conflicting models described above. In the case of an extended stagnancy in the western Mediterranean basin, however, erosional cliffs and terraces are expected to have formed at

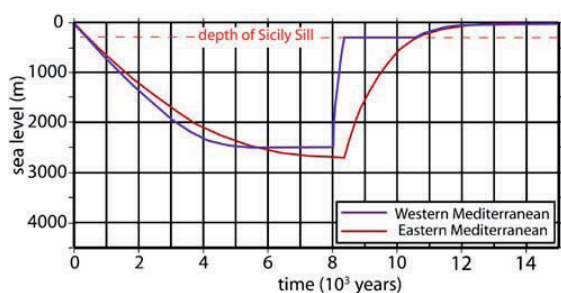


Fig. 2 Modelled sea-level curves for the Western and Eastern Mediterranean (from Meijer and Krijgsman 2005). The sea level in the western and eastern basins evolved differently from the time it dropped below the depth of the Sicilian Sill. The assumptions for this model are the present-day geometry and inflow rates at the Gibraltar Strait and a depth of the Sicily Sill of 300 m. The reflooding of the western basin was rapid until sea level reached the height of the sill, after which sea level remained constant for about 2,000 years

the corresponding position of sea level. Although numerous studies based on seismic reflection data indicate sub-aerial erosion during the MSC, there is a lack of systematic investigations of the Messinian Unconformity at shallow depths. More precisely, for the identification of any erosional features linked to sea-level stagnancies at the level of the Sicily Sill, extensive mapping of this depth interval is needed. Indeed, interpretation based on single profiles is problematic for the discrimination between erosional terraces and other features like incised valleys, fault scarps or head scarps of submarine slides.

In search of evidence of such sea-level stagnancies at the Sicily Sill, and of the duration of stagnant water levels in the Western Mediterranean, we evaluated seismic reflection data from the south-western shelf of Mallorca Island, the Bay of Oran and the Alboran Ridge (Fig. 1), collected in summer 2006 during the CARBMED research cruise M69/1 aboard the R/V *Meteor* (Hübscher et al. 2010). The data further allow constraining the palaeo-depth of the Sicily Sill.

Messinian Salinity Crisis

Deep basin stratigraphy

Current understanding of the Messinian palaeo-environment is based mostly on studies of exposed sedimentary successions in peri-Mediterranean basins (e.g. Crete, Sicily, Cyprus, southern Spain; Clauzon et al. 1996; Riding et al. 1998; Butler et al. 1999; Rouchy and Caruso 2006). However, such marginal basins represent only ~5% of all Messinian evaporites. Our knowledge of the deep basinal evaporites comes largely from seismic reflection data, which can be considered as the most important archive of Messinian environmental changes (Hübscher et al. 2007). Seismic units of MSC deposits have been investigated in several sub-basins of the Western Mediterranean, including along the Ligurian margin (Savoye and Piper 1991), and in the Gulf of Lion (Lofi et al. 2005) and the Valencian Basin (Maillard et al. 2006). Here, three units with distinct seismic facies have been identified (Montadert et al. 1970), formerly labelled the lower evaporite, salt and upper evaporite units. Recently, the nomenclature has been modified to the lower, middle and upper units respectively (Lofi et al. 2010). East of the Sicily Strait, seismic studies of basinal evaporites concentrated on the Cyprus Arc (Bridge et al. 2005; Hall et al. 2005; Hübscher et al. 2009), the Nile cone (Loncke et al. 2004, 2006) and the Levantine Basin (Mart and Bengai 1982; Garfunkel and Almagor 1984; Cohen 1993; Bertoni and Cartwright 2006, 2007). Up to six evaporitic sequences can be traced throughout the Levantine Basin (Hübscher et al. 2007). The differing stratigraphy of basinal evaporites west

and east of the Sicily Sill suggests a separation of the Western and Eastern Mediterranean basins and, consequently, individual water budgets being responsible for the formation of evaporitic sequences.

Messinian erosional surfaces

The MSC sea-level drawdown resulted in sub-aerial exposure of the continental slopes and triggered massive erosion, canyon development, and the deposition of detritus on the lower slopes and adjacent fringing abyssal plains (Rizzini et al. 1978; Clauzon et al. 1996; Lofi et al. 2005; Sage et al. 2005; Bertoni and Cartwright 2006, 2007; Maillard et al. 2006, 2010). Several erosion surfaces have been evidenced on seismic data, labelled as the MES (for margin erosion surface, after Sage et al. 2005), BES (for bottom erosion surface, after Maillard et al. 2006), IES (intermediate erosion surface) and TES (for top erosion surface, after Maillard et al. 2006). For a recent detailed overview, the reader is referred to Lofi et al. (2010) and references therein.

The MES is a widespread unconformity commonly interpreted as resulting from several phases of sub-aerial erosion. It is overlain by Plio-Pleistocene deposits and extends downslope to the onlap point of the deep basin Messinian trilogy deposits. There it passes laterally to the BES, TES and IES, each of these erosion surfaces being defined based on their relationship to the downslope Messinian units. Since the pre-Messinian marine sediments were eroded mainly during the MSC, there is a sharp contrast between the reflection characteristics of the consolidated strata beneath the MES and of the lower Pliocene strata deposited under marine conditions after the reflooding of the Mediterranean (Barber 1981; Stampfli and Höcker 1989; Lofi et al. 2005).

Physical and tectonic setting

The Mediterranean Sea is a semi-enclosed marginal sea located between southern Europe and North Africa, connected to the Atlantic Ocean through the Strait of Gibraltar, and comprising a western and an eastern basin (Fig. 1), each consisting of several sub-basins. The gateway between the western and eastern basins is a relatively narrow seaway around Sicily, separating the Italian peninsula from North Africa. At the Sicily Sill, the present-day water depth is about 300 m.

The Western Mediterranean has undergone a complex tectonic evolution, Gelabert et al. (2002) recognizing three stages: during the first stage, which lasted from the latest Cretaceous until the Eocene–Oligocene transition, E–W-striking subduction of Tethyan oceanic crust beneath the

Iberian and the Austroalpine–Apulian plate occurred. During the Early Oligocene (second stage), the Balearics, Corsica and Sardinia collided with Iberia and the continental blocks of the Internal Zone of the Betics and Rif (Jolivet and Faccenna 2000). From the Late Oligocene until the Middle Miocene (third stage), extensional conditions led to thinning of the continental crust in basins and the formation of back-arc basins (e.g. Gelabert et al. 2002).

The opening of the western Mediterranean basins occurred during the last 30 Ma. The westward subduction (Apennines–Maghrebides arc) of Tethyan crust initiated an extensional tectonic regime in the back-arc zone (e.g. Dewey et al. 1989; Gueguen et al. 1998; Gelabert et al. 2002). Due to changing convergence rates and velocities, the subduction zone retreated eastwards to its present-day position beneath the Italian peninsula, reaching down to Calabria and turning west via Sicily to the North African margin (for details see Gueguen et al. 1998; Faccenna et al. 2001).

Sicily Strait

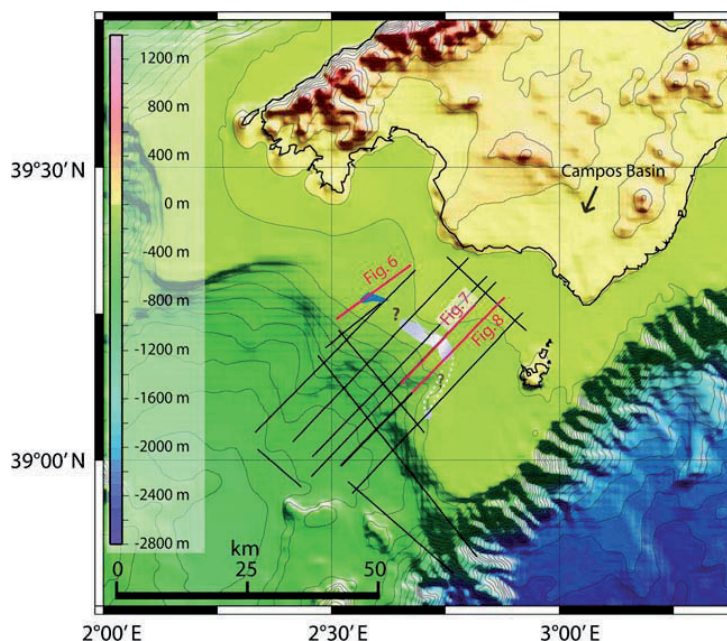
The Central Mediterranean has a complex tectonic history because of the convergence between Africa and Europe (see above). Sicily is located above the Apennines–Calabrian convergence zone and was therefore affected by complex tectonics during the Cainozoic.

The tectonic configuration of the Sicily Strait has been reconstructed for Eocene to Recent times by Reeder et al. (2002). During the Eocene, Neo-Tethyan crust existed between southern Europe (Corsica, Sardinia and the Balearic Islands) and northern Africa (Tunisia, Sicily; Dewey et al. 1989). During the Oligocene and Miocene, the eastward retreat of the Apennines–Calabrian arc caused a reorganisation of the plate boundaries. By the end of the Miocene, the present-day tectonic configuration was developed (Dewey et al. 1989; Reeder et al. 2002). Using the base levels of Western Mediterranean rivers incised during sea-level stagnancy in the western basin, Blanc (2006) reconstructed the depth of the Sicily Sill during the MSC as ranging from 350–400 m relative to present-day sea level.

SW shelf of Mallorca Island

The study area off Mallorca Island comprises the SW shelf and shelf slope in prolongation of the Campos Basin (Fig. 3). The shelf is between 100 and 150 m deep, and the seafloor descends in a SW direction to the Mallorca Channel, where water depths reach 1,000 m. In the southeast the shelf is bounded by the Emile Baudot Escarpment, which has a very steep slope, descending to water depths exceeding 2,400 m.

Fig. 3 Bathymetric map (m) of the SW shelf off Mallorca Island. *Lines* Seismic profiles, *red lines* profiles shown in Figs. 6, 7 and 8; *violet* mapped wide terraces with cliffs, *white* change in dip of the MES; *dotted lines* inferred continuation of terraces between the profiles



During the latest Oligocene and the Early Miocene, the anticlockwise rotation of the Corso-Sardinic block (Montigny et al. 1981) led to extension and crustal thinning between Iberia and the Balearic Promontory. As a consequence, the Valencian Trough was opened (Vegas 1992). During the Early Miocene, the Alboran Microplate started to drift westwards, thereby imposing a compressional tectonic regime on the Balearics. Mesozoic rocks, consisting mainly of carbonates (Barnolas and Simó 1984; Alvaro et al. 1989), were incorporated into the Alpine fold-and-thrust belt during this phase. In the Late Miocene, the persisting rotation of the Corso-Sardinic block and the opening of the South Balearic-Algerian Basin caused an extensional regime on Mallorca. During this phase evolved both the main horst and graben structure, consisting of Mesozoic and partially Palaeozoic basement (Jenkyns et al. 1990), and the small basins on the island (Pomar 1979). From Miocene to Pliocene times, carbonate sediments accumulated in these basins, overlapping onto the faulted blocks (Pomar and Ward 1994; Alonso-Zarza et al. 2003 and references therein).

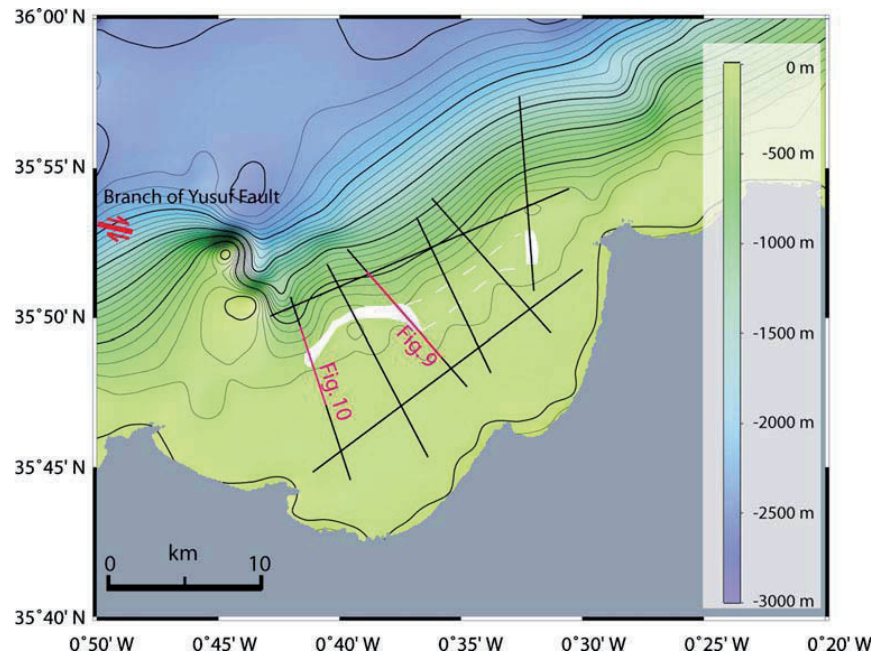
The SW shelf of Mallorca represents the seaward prolongation of the upper Miocene Lluçmajor carbonate platform and of the Campos Basin. The top of the Lluçmajor platform lies today about 70 m above sea level. The Campos Basin subsided during the Pleistocene (Pomar and Ward 1994). Mesozoic and Neogene carbonates are only slightly tilted, due to normal and strike-slip faulting (Pomar 2001).

Earlier seismic data of the Mallorca Channel and the continental slope adjacent to our study area were acquired by Acosta et al. (2001, 2003, 2004), showing an unconformity truncating the poorly to well stratified underlying unit. They interpreted this horizon as the MES (labelled Messinian Unconformity in Acosta et al. 2001, 2003, 2004). In the Mallorca Channel, the MES is at a relatively deep position (approx. 1 s two-way traveltime; Acosta et al. 2004), but ascends to approx. 0.5 s TWT at the shelf slope (Acosta et al. 2001). The unconformity shows an irregular topography and has an erosional appearance. Above this horizon, two units were interpreted to have been deposited during the latest Messinian to Quaternary. According to Acosta et al., the post-Messinian succession is faulted due mainly to gravitational, rather than deep-rooted processes (cf. the latter would indicate vertical movement). One of their published survey lines extends into our new survey area, thus allowing correlating the stratigraphy in both datasets.

Bay of Oran

The Bay of Oran is semi-oval in shape and extends 30 km in a W–E direction. The study area includes the shelf and the continental slope down to a water depth of 1,000 m (Fig. 4). The Yusuf Fault is a NW–SE-oriented strike-slip fault which takes a W–E direction west of the Bay of Oran (Ballesteros et al. 2008). According to Domzig et al. (2006), a branch of this fault may extend into the region of the bay (Fig. 4).

Fig. 4 Bathymetric map (m) of the Bay of Oran (Algeria). *Lines* Seismic profiles, *red lines* profiles shown in Figs. 9 and 10; *white* mapped terraces of the MES correlated between the profiles; *dotted lines* inferred continuation of terraces between the profiles



The structural and geological setting in the vicinity of Oran is dominated by the southward thrusts of the External Tell, which formed during the Alpine continental collision (de Lamotte et al. 2000). Folded and faulted Mesozoic carbonates of the former southern margin of the Tethys are unconformably overlain by post-orogenic Miocene marine to coastal sediments (Cornet et al. 1952). From adjacent areas southwest of Oran, some Messinian carbonate platforms are known which evolved on folded Mesozoic basement (Rouchy and Saint Martin 1992; Cornée et al. 1994 and references therein). The continental margin is characterized by a steep north-dipping escarpment, with possible normal faulting. Onshore, marine terraces of the last interglacial (marine isotope stage 5) have uplifted at rates of approx. 0.02 mm/year (Bouhadad 2001), indicating active deformation in Oran Bay. Betzler et al. (2010) observed that Holocene carbonate production occurs on the shelf in the bay itself. Also, those authors found siliciclastics close to the modern shoreline, but not on the outer shelf.

At present, seismic activity in the region of Oran is moderate in terms of intensity or magnitude, and characterised by long recurrence periods (Bouhadad 2001), two $M < 5$ earthquakes having occurred in 1889 and 1959. Stronger seismic events were recorded in 1790 (Oran, intensity $I=XI$) and 1994 (Mascara earthquake, $M 6.0$), with a high death toll (Ayadi et al. 2002). Generally, the focal mechanisms showed thrust-related dissolution (Bouhadad 2001), whereby strike-slip faults had a dextral component

on N110-130-trending fault planes (Ayadi et al. 2002). This is in accordance with the movement and seismicity along the Yusuf Fault in the western Alboran Sea. Existing bathymetry and seismic data for the Oran region do not show any significant recent offshore tectonic activity, with the exception of the Yusuf Fault (Domzig et al. 2006).

Alboran Ridge

The Alboran Ridge is a SW–NE elongated basement high with a length of 180 km and a width of 30 km (Fig. 5), rising up to 1,000 m above the surrounding abyssal plain and forming Alboran Island. The ridge consists of magmatic and metamorphic rocks (Maldonado et al. 1992 and references therein), while Alboran Island is composed mainly of volcanoclastic rocks on a metamorphic basement (Hoernle et al. 2003). The volcanic rocks are about 9.3 Ma old (Duggen et al. 2004). The Alboran Ridge developed due to compressional activity during the Tortonian to the Present (Bourgeois et al. 1992).

Drilling during ODP Leg 161 was performed in several regions of the Alboran Sea, revealing that the oldest sediments are derived from Early Miocene rocks and overlie the metamorphic basement. Sedimentation continued until the MSC. An erosional surface represents the MES (Campillo et al. 1992; Maldonado et al. 1992), and deposition was re-established after the MSC.

Evidence for Pleistocene to Holocene deformation was found in seismic sections of the ridge (Comas et al. 1999),

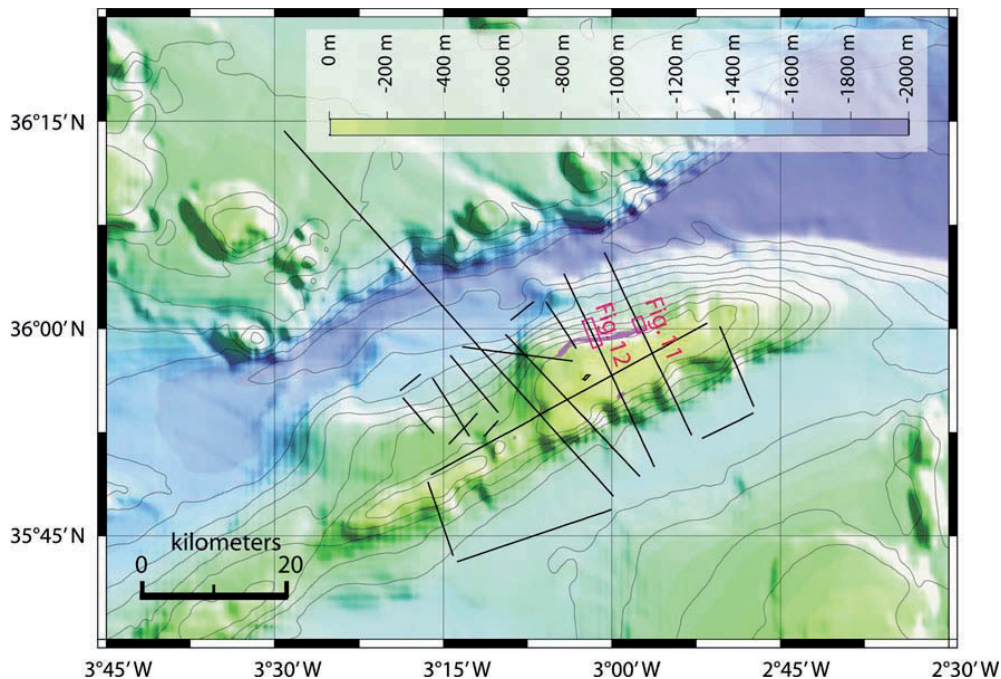


Fig. 5 Bathymetric map (m) of the Alboran Ridge. *Lines* Seismic profiles, *red lines* profiles shown in Figs. 11 and 12; *violet* mapped terraces of the MES

where the MES is characterised by an angular unconformity. Site 976 in the West Alboran Basin reveals two periods of subsidence, one at 11–10.7 Ma (rate of 3 km/10⁶ years), another at 2.5–0 Ma (rate of 0.5 km/10⁶ years), as well as uplift at 5–2.5 Ma (Comas et al. 1999). Compressional structures have been identified along both the southern and the northern flanks of the ridge. On the southern flank, fault-related uplifting and folding can be found within the Pliocene–Holocene sediments. Comas et al. (1999) proposed that both uplifting due to folding and faulting occurred at different locations along the Alboran Ridge since Late Miocene times. Furthermore, based on a fault population analysis Maestro-González et al. (2008) concluded a reactivation of basement faults at the ridge due to compression during the late Tortonian and Messinian. These authors suggest that the compressional regime probably prevailed also during more recent times.

Materials and methods

Seismic data were acquired using a 600-m-long digital streamer incorporating 144 channels (Mallorca), a 150-m-long 24-channel analog streamer (Bay of Oran and Alboran Ridge), and two GI-guns as seismic sources. The volumes for the generator and injector were 45 and 105 cubic inches

respectively, and the pressure within the air chambers was kept constant at 140 bar. The shot distance was 25 m.

For the datasets from the Oran and Alboran study areas, a CMP (common midpoint)-based data processing procedure was used (editing, geometry processing, interactive velocity analysis, stacking, post-stack time migration). The dataset from the Mallorca study area was processed using a CRS (common reflection surface) stacking routine (Mann 2002). The procedure includes stacking over a hyperbolic area and, thus, over neighbouring CMPs. As a result, the fold is increased and, thereby, the data quality (e.g. S/N ratio). The main frequencies were 20–160 Hz for all three study areas. Assigned depths were calculated assuming a seismic velocity of 1,500 m/s for the water column and an average velocity of 1,800 m/s for the post-Messinian sediments.

Seismo-stratigraphic interpretation incorporates previously published information from surrounding areas such as the Valencian Trough (Maillard et al. 2006), the Mallorca and Ibiza channels (Acosta et al. 2003, 2004) and the Alboran Sea (Comas et al. 1999). The correlation was performed on the basis of specific acoustic facies characteristics of individual seismic units and the occurrence of prominent horizons—e.g. the MES.

The locations of seismic profiles acquired during the M69/1 cruise are illustrated in Figs. 3, 4 and 5. Of these, seven are reported in more detail below.

Results

SW shelf of Mallorca

Three seismic profiles from the south-western shelf of Mallorca cover the shelf and upper slope (Figs. 6, 7 and 8). The profile in Fig. 6 has a length of 18 km. In the proximal part, the water depth is about 75 m and the seafloor descends basinwards to a depth of 300 m. The profile in Fig. 7 has a length of about 23 km. On the shallow shelf, the water depth is about 75 m and the seafloor descends south-westwards to 450 m. The profile in Fig. 8 has a length of about 27 km and also strikes perpendicular to the bathymetric contours. In the shallower part of the profile, the water depth is 75–150 m. The seafloor descends to a depth of 375 m towards the SW.

In all seismic profiles for this study area, we identified a prominent high-amplitude reflection with an erosive character in the proximal part of the profiles. This reflection correlates well with the MES of the seismic lines of Acosta et al. (2004). In Fig. 6, the MES is located at 0.55 s TWT in the proximal part, and ascends coastwards to the seafloor, truncating several strong reflections at about 0.5–0.48 s TWT. Adjacent to this truncation, a terrace about 1.5 km wide is present at 0.48 s TWT.

In the distal part of the seismic section in Fig. 7, the MES is downfaulted by 0.05 s TWT. Coastwards of this morphological step, the MES occurs at 0.75 s TWT and ascends at an angle of 1.4° up to a TWT of 0.48 s (approx. 400 m). At this depth, a change in dip is observed, the MES becoming nearly horizontal (0.4°). Coastwards of this 400-m-wide terrace, the MES ascends to 0.34 s TWT (1.5°) before rising more steeply up to 0.19 s TWT. In the

Fig. 6 Seismic section from the SW shelf of Mallorca (for location, see Fig. 3; *VE* vertical exaggeration). The MES (*red line*) truncates internal reflections of the underlying unit at about 0.45 s TWT (*red arrow*), and is overlain by a unit with relatively weak reflections which merges upwards into a unit with strong reflections

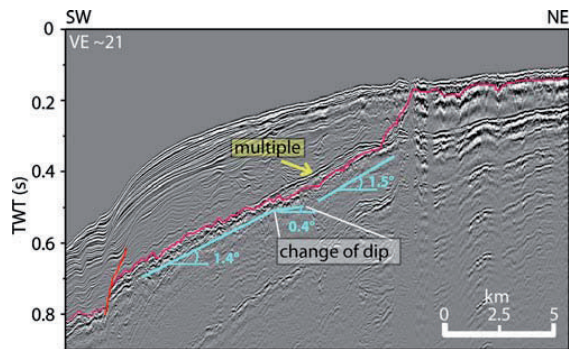
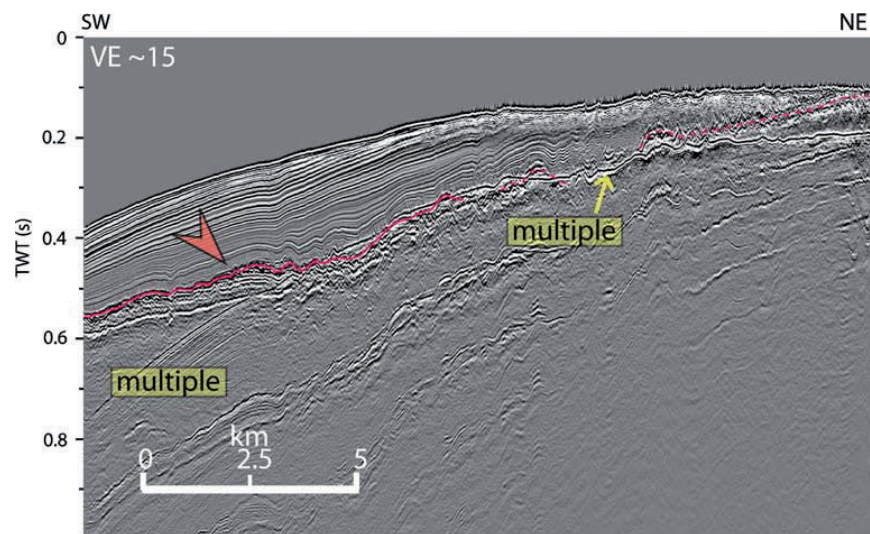


Fig. 7 Seismic section from the SW shelf of Mallorca (for location, see Fig. 3; *VE* vertical exaggeration). In the distal part a fault can be seen, the MES (*red line*) being displaced by about 30 m. The MES ascends up to a TWT of 0.48 s with an angle of 1.4° . At 0.48 s TWT, the MES has a gentle dip of 0.4° for about 1 km. Coastwards, it proceeds more steeply to 0.38 s TWT, where it ascends even more steeply to 0.19 s TWT

proximal part of the profile, the MES has an irregular, near-horizontal morphology.

In Fig. 8, the MES is observed at about 0.8 s TWT in the distal part and at 0.2 s TWT in the proximal part. At about 0.45 s TWT (approx. 380 m), it forms an approx. 1.5-km-wide terrace and a morphologic step; an incision into the underlying unit can be clearly seen at the foot of this step. This change in morphology occurs at a relatively constant depth interval (380–400 m) in all available seismic data from the Mallorcan shelf, except for one profile. In this profile (not shown), a depression in the MES occurs at 0.45 s TWT, but here the morphology of the underlying unit is generally irregular. The changes in MES morphology on the SW shelf of Mallorca and, in

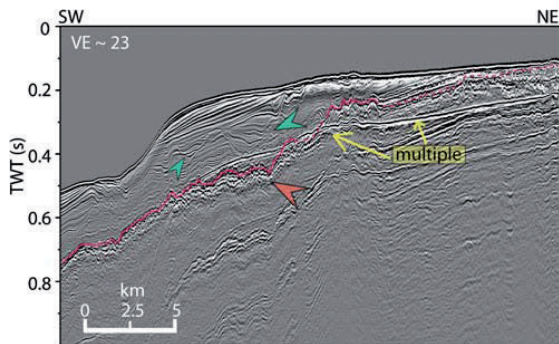


Fig. 8 Seismic section from the SW shelf of Mallorca (for location, see Fig. 3; *VE* vertical exaggeration). At about 0.45 s TWT, the MES (*red line*) is incised into the underlying unit (*red arrow*) and forms a step-like feature about 1.5 km wide. Coastwards, the MES ascends steeply to 0.22 s TWT. Above it, a unit comprising relatively weak reflections is itself truncated at the top. This unconformity is characterized by incisions in the proximal part (*green arrows*), whereas the transition between the two units is more successive in the distal part

particular, the locations of terraces and cliffs are indicated in Fig. 3.

In all seismic profiles, the MES is overlain by two distinct units with different acoustic facies. The lower unit consists of generally continuous, low-amplitude internal reflections parallel or sub-parallel to the MES. In Figs. 6 and 7, undulations in these reflections mirror the irregularities of the MES, and gradually diminish upwards. This lower unit is superimposed by a high-amplitude unit. The transition is marked by an increase in the amplitude of concordant reflections. In Fig. 8, an unconformity marks the boundary between the low-amplitude unit and the overlying unit. In the proximal part of this profile, channels are incised into the low-amplitude unit. The infill deposits

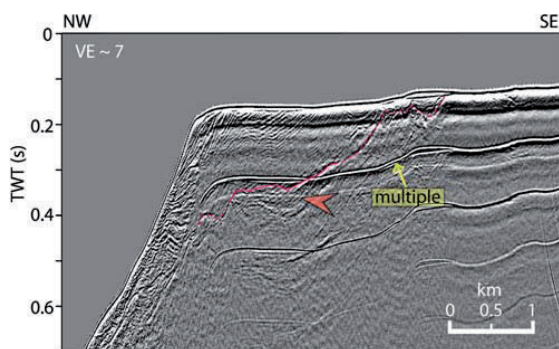


Fig. 9 Seismic section from the Bay of Oran (for location, see Fig. 4; *VE* vertical exaggeration). At about 0.35 s TWT, a morphologic terrace can be seen (*red arrow*) in the prominent reflection (*red line*). This terrace is about 1 km wide; coastwards, the reflection which forms the terrace ascends to 0.18 s TWT. It is overlain by a transparent unit comprising basinward-dipping clinoforms

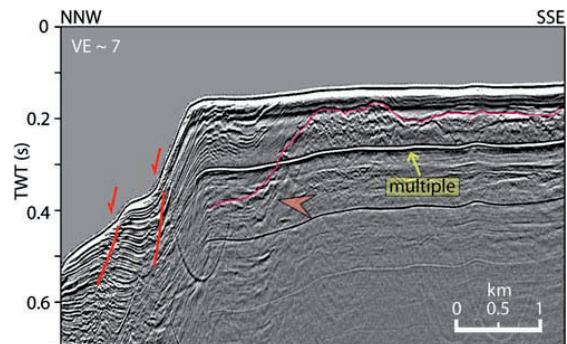


Fig. 10 Seismic section from the Bay of Oran (for location, see Fig. 4; *VE* vertical exaggeration). A strong reflection (*red line*) forms a terrace-like feature at about 0.35 s TWT (*red arrow*), about 500 m wide. Coastwards, the strong reflection ascends to about 0.2 s TWT. In the proximal part of the profile, the reflection is irregular and rugged, probably due to former sub-aerial exposure. Superimposed on the unconformity is a transparent seismic unit which itself is overlain by a unit with basinward-dipping reflections. This latter unit is tilted due to normal faulting in the distal part

of these channels correlate basinwards with higher-amplitude reflections and, accordingly, with the high-amplitude unit of Figs. 6 and 7. Figure 8 also shows a sediment body which overlies the infill deposits of the incised valleys. The internal reflections of the wedge dip basinwards at an angle of about 1°. This unit is notably present only in this seismic profile.

Bay of Oran

Figures 9 and 10 show seismic sections across the shelf and the adjacent continental slope of the Bay of Oran, at water depths of 75–150 m. The continental slope dips at an angle of about 19°. Both profiles reveal an unconformity below the outer shelf deposits. This unconformity forms a terrace at a TWT of about 0.38 s (320 m). In Fig. 9, the width of this terrace is about 1 km, the corresponding value being about 800 m in Fig. 10. This terrace has been identified on four profiles from this study area (Fig. 4), the unconformity being masked by the seafloor multiple on other profiles.

Coastwards, the unconformity ascends to a TWT of about 0.18 s, where another hummocky terrace approx. 2 km wide is visible (Fig. 10). In this region, a truncation of the underlying deposits at the unconformity can not be clearly identified. Above the deeper terraces occurs a prograding wedge composed of several dipping clinoforms; basinwards, it is tilted due to normal faulting.

Alboran Ridge

Figures 11 and 12 show details of seismic profiles from the northern flank of the Alboran Ridge. In Fig. 11, the seafloor

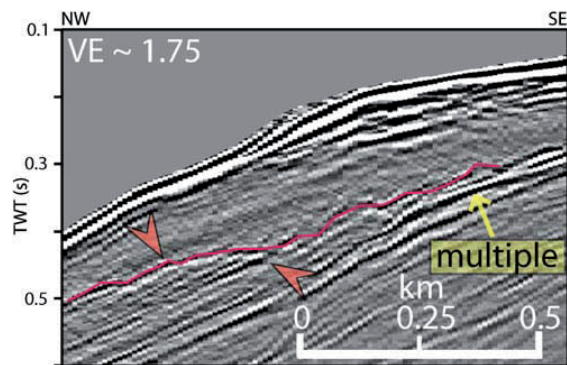


Fig. 11 Seismic section from the Alboran Ridge (for location, see Fig. 5; *VE* vertical exaggeration). At a TWT of about 0.43 s, a reflection (*red line*) truncates the internal reflections of the underlying unit and forms an approx. 150-m-wide, terrace-like feature (*red arrows*). The unconformity is overlain by a transparent seismic unit which, in its proximal part, is characterized by a few strong, basinward-dipping reflections just beyond the seafloor

ascends from 0.4 s (300 m) to 0.15 s TWT (112 m). A distinct unconformity underlies the platform edge at approx. 200 ms TWT under the seafloor. At a TWT of 0.43 s (360 m), underlying reflections are clearly truncated at the unconformity. The unconformity shows a change in dip indicating a 250-m-wide terrace-like feature, above which a transparent seismic unit occurs. Close to the seafloor, some high-amplitude reflections dip basinwards.

In Fig. 12, the seafloor ascends from 0.67 s (502 m) to 0.14 s TWT (105 m). There is a significant change in dip of the seafloor at 0.15 s TWT (112 m), which marks the margin of the flat-topped ridge. At about 0.45 s TWT (approx. 360 m), a 350-m-wide terrace-like feature similar to that in

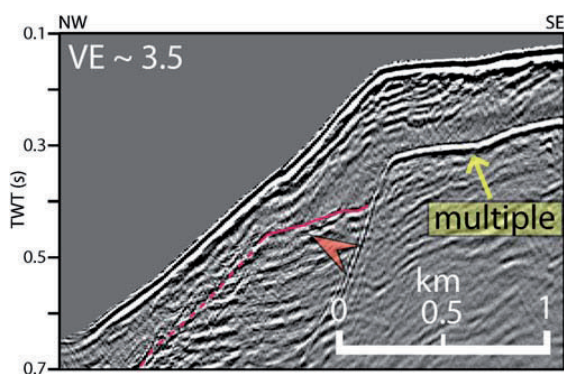


Fig. 12 Seismic section from the Alboran Ridge (for location, see Fig. 5; *VE* vertical exaggeration). An irregular rugged reflection (*red line*) at about 0.43 s TWT represents an erosional unconformity (*red arrow*). As in the case of the Bay of Oran (Fig. 10), this unconformity is overlain by a transparent seismic unit above which basinward-dipping clinoforms are visible

Fig. 10 is present. A transparent seismic unit is again observed to be superimposed on the unconformity. The terrace-like feature was clearly identified on four profiles, mainly along the northern flank of the ridge (Fig. 5).

Discussion and conclusions

Stratigraphy

Mallorca

On the seismic profiles off Mallorca, the morphology of the MES resembles an embayment with cliffs and terraces at its margins but a much smoother morphology at its centre (Fig. 3). This laterally changing MES morphology probably reflects the existence of calmer hydrodynamic conditions in the interior part of the embayment and higher energy along the offshore margins. The transparent unit overlying the MES consists of lower Pliocene sediments, and has been identified in many other parts of the Mediterranean (e.g. Acosta et al. 2004; Maillard et al. 2006). Because of the low reflection amplitudes, it is likely that this unit is composed of hemipelagic sediments which have accumulated during a sea-level highstand. The incisions at the top of this unit can be related to a drop in sea level, presumably dating to the Mid or Late Pliocene. The infill deposits, as well as their distal equivalents, accumulated during the subsequent sea-level rise and highstand. The superimposed sediment body on Fig. 8 with basinward-dipping reflections is interpreted to have formed during Pleistocene to Holocene times.

Bay of Oran

No seismic data from the Bay of Oran have previously been published and the stratigraphy can not be linked to any well data. However, marine and coastal sediments of Neogene age occur in the vicinity of Oran (Cornet et al. 1952). Furthermore, Miocene carbonate platforms are known from onshore sites NW of Oran (Cornée et al. 1994). In the seismic data, a distinct unconformity can be recognized at the base of the progradational unit. There is no indication of sub-aerial exposure within this superimposed unit. We therefore interpret the unconformity as the MES, at which underlying rocks have been eroded during the MSC. The progradational unit is most likely composed mainly of carbonates which were produced on the shelf and exported to the continental slope since the Pliocene. This interpretation is corroborated by the analytical data of Betzler et al. (2010), who found Holocene carbonates unconformably overlying Miocene to Pliocene or older rocks on the outer shelf.

Alboran Ridge

Seismic and sedimentologic data from the Alboran Basin show that the sediments have accumulated on a folded metamorphic basement, while the seismic data from the Alboran Ridge reveal that it is composed of volcanoclastic and volcanic rocks (Hoernle et al. 2003; Duggen et al. 2004). Betzler et al. (2010) show that neritic carbonates are produced on the ridge, which probably was also the case during past episodes of sea-level highstands. Our data suggest that sediments are present on the ridge crest as well as on its flanks. An erosional surface can be seen in the seismic sections which we interpret as the MES. Although the composition of the basement rocks (carbonates or volcanoclastics) is unclear, the pattern of basinward-dipping reflections below the MES suggests the presence of sedimentary strata.

Since terrigenous input from adjacent areas can be neglected, we conclude that the superimposed transparent unit, which partly shows dipping reflections above the MES, consists of material exported from the ridge crest, which is expected to represent an admixture of volcanoclastics and carbonates.

Evolution of erosional terraces

In each of the investigated areas, terrace-like features and morphologic elongated steps coastwards of these are observed along a high-amplitude reflection. Commonly, these may result from normal faulting or submarine landsliding. Assuming faulting, the step would represent the fault plane of the footwall block. If the step is considered to result from mass wasting, it would represent a head scarp upslope of the slide (Locat and Lee 2002). However, a deep-rooted fault should also be observable in the seismic data in the downward prolongation of the escarpment, which is not the case. Furthermore, the spatial extent of a normal fault should be linear. If the escarpment is considered to result from sliding, a curved head scarp should have the concave side facing the basin (Lewis 1971;

Dingle 1977). However, these diagnostic features differ from the mapped escarpment and terrace morphology. Off Mallorca, the morphologic step and terraces are present only at the offshore margins of an embayment-like feature, and not in its interior part (Fig. 3). In the Bay of Oran, the step is bended with the convex side facing the deep basin (Fig. 4). At the Alboran Ridge, no distinct step has been observed, which rules out the presence of faulting or sliding. Thus, we conclude that the terraces are formed by erosion and, consequently, the elongated steps represent cliffs which were generated during the MSC.

The presence of terraces at similar depths in three different study areas strongly suggests that a common regional event triggered their development. The notion of a constant sea level in the Western Mediterranean at the depth of the Sicily Sill during the MSC, as proposed by Blanc (2000, 2006) and Meijer and Krijgsman (2005), is consistent with these observations if the terraces evolved contemporaneously and at essentially the same depth.

In the Bay of Oran, the TWT of these terraces corresponds to a depth of approx. 320 m, whereas in the study area on the Alboran Ridge they are found at about 360 m depth. Off Mallorca, the erosional truncation and the terraces of the MES are present at a depth of about 380 m (cf. all values calculated using a velocity of 1,500 m/s for the water column and 1,800 m/s within the sediments). These slight differences in terrace depths could be explained by distinct subsidence and uplift rates in the various study areas. Late Miocene reefs exist about 70 m above present-day sea level in the hinterland of Mallorca (Pomar 1979; Pomar and Ward 1995). According to Haq et al. (1987), sea level was about 70–80 m higher in the Late Miocene than today, but lower values (50–60 m higher sea level) have recently been published (e.g. Müller et al. 2008). Although subsidence during the Pleistocene in the Campos Basin was reported by Pomar and Ward (1995), we conclude that the study area off Mallorca has been relatively stable in terms of vertical movements since the Miocene. The difference between the depths of the Mallorcan and the

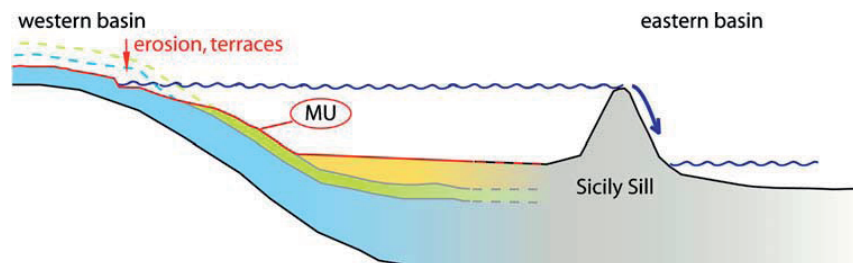


Fig. 13 Schematic sketch illustrating the development of the MES and associated terraces in the Western Mediterranean. During flooding or drawdown events, water overflowed into the eastern basin, while the sea level in the western basin remained constant. These events

triggered the development of erosional terraces due to abrasion, dissolution and karstification close to sea level on western Mediterranean continental margins

Alboran Ridge terraces corresponds to an uplift rate of 0.004 mm/year at the ridge, which is consistent with data reported by Comas et al. (1999). In the study area off Oran, the calculated uplift rate based on terrace depth is about 0.012 mm/year in terms of a stable Mallorca scenario. This value is in the order of previously published uplift rates (0.02 mm/year) since the last interglacial (Bouhadad 2001).

As our observations reflect the postulated uplift trends in the Oran (Bouhadad 2001) and Alboran region (Bourgois et al. 1992; Comas et al. 1999; Maestro-González et al. 2008), and a possible minor subsidence trend off Mallorca (Pomar and Ward 1995), we infer a contemporaneous development of the terraces at essentially the same depth in these areas.

Implication of occurrences of erosional terraces

Considering the sea-level history of the Mediterranean basins during the MSC, the Sicily Sill is of central importance. According to our interpretation for the sediment-starved continental slopes investigated in this paper, the margin erosion surface was shaped during periods of sea-level stagnancy when water from the western Mediterranean Sea overflowed into the eastern basin. During these stillstands, hydrodynamic processes and, accordingly, mechanical abrasion resulted in massive erosion of MSC and older deposits. In addition, intensified dissolution and karstification at or close to the sea level could have contributed to the development of the observed terraces and cliffs (Fig. 13).

Since the stratigraphy off Mallorca suggests that no significant uplift or subsidence occurred after the Messinian, we conclude that uplift must have occurred at the Alboran Ridge and the Bay of Oran. Furthermore, we infer that the palaeo-depth of the Sicily Sill corresponds to the observed terrace depth of 380 m off Mallorca, thereby contributing to the ongoing debate about the Sicily Sill depth during the MSC. It remains unclear whether this erosion appeared during the sea-level drawdown (Blanc 2000, 2006), during sea-level fluctuation in the MSC (Gargani and Rigollet 2007) or during the terminal flooding at the end of the MSC (Meijer and Krijgsman 2005). In the case of rapid flooding (Blanc 2000, 2006; Garcia-Castellanos et al. 2009), hydrodynamic processes would not have the potential for massive erosion of the subsurface. Even within such a scenario, however, modelling of the genesis of evaporitic sequences in the Mediterranean suggests that, during an early drawdown of the sea level, water spilled over the Sicily Sill and stagnated in the western basin during some thousand years (Blanc 2000, 2006). Such a protracted period of sea-level stagnancy would plausibly suffice to erode the continental shelves and to produce the detected terraces. Consequently, our obser-

ations support all those scenarios which accommodate long-term sea-level stagnancies during the MSC.

Future work should focus on areas of minor sediment input to validate this hypothesis. In such settings, the geometries of the continental slopes are essentially affected only by hydrodynamic processes—e.g. erosion at the wave base or in the breaker zone. Such data could provide valuable information on the sea-level history of the time period in question. Furthermore, if this concept were to be verified at other locations of a wider study region, this would be a valuable tool for reconstructing subsidence and uplift rates along the Western Mediterranean margins since the Messinian Salinity Crisis.

Acknowledgements We gratefully acknowledge the scientific party as well as captain and crew of the research vessel *Meteor* for their support during CARBMED cruise M69/1. Thanks go to P. Meijer, an anonymous reviewer and the journal editors for valuable comments which helped improve the manuscript. We would also like to thank Stefan Dümmon for his support by providing a CRS routine. The STRATEC project was funded by the Deutsche Forschungsgemeinschaft (DFG research grant Hu698/16).

References

- Acosta J, Muñoz A, Herranz P, Palomo C, Ballesteros M, Vaquero M, Uchupi E (2001) Geodynamics of the Emile Baudot Escarpment and the Balearic Promontory, western Mediterranean. *Mar Petrol Geol* 18:349–369
- Acosta J, Canals M, López-Martínez J, Muñoz A, Herranz P, Urgeles R, Palomo C, Casamor JL (2003) The Balearic Promontory geomorphology (western Mediterranean): morphostructure and active processes. *Geomorphology* 49:177–204
- Acosta J, Canals M, Carbó A, Muñoz A, Urgeles R, Muñoz-Martín A, Uchupi E (2004) Sea floor morphology and Plio-Quaternary sedimentary cover of the Mallorca Channel, Balearic Islands, western Mediterranean. *Mar Geol* 206:165–179
- Alonso-Zarza AM, Armenteros I, Braga JC (2003) Tertiary. In: Gibbons W, Moreno T (eds) *The geology of Spain*. Geological Society, London, pp 293–334
- Alvaro M, Barnolas A, Cabra P, Comas-Rengifo MJ, Fernández-López SR, Goy A, del Olmo P, del Pozo JR, Simo A, Ureta S (1989) El Jurásico de Mallorca (Islas Baleares). *Cuad Geol Ibér* 13:67–120
- Ayadi A, Ousadou-Ayadi F, Bourouis S, Benhallou H (2002) Seismotectonics and seismic quietness of the Oranie region (Western Algeria): the Mascara earthquake of August 18th 1994, Mw = 5.7, Ms = 6.0. *J Seismol* 6:13–23
- Ballesteros M, Rivera J, Muñoz A, Muñoz-Martín A, Acosta J, Carbó A, Uchupi E (2008) Alboran Basin, southern Spain - Part II: neogene tectonic implications for the orogenic float model. *Mar Petrol Geol* 25:75–101
- Barber PM (1981) Messinian subaerial erosion of the proto-Nile Delta. *Mar Geol* 44:253–272
- Barnolas A, Simó A (1984) Sedimentología. In: Barnolas-Cortinas (ed) *Sedimentología del Jurásico de Mallorca*, Excursion Guide. Grupo Español Mesozoico, Palma de Mallorca, pp 73–119
- Bertoni C, Cartwright JA (2006) Controls on the basinwide architecture of late Miocene (Messinian) evaporites on the Levant margin (Eastern Mediterranean). *Sediment Geol* 188(189):93–114

- Bertoni C, Cartwright JA (2007) Major erosion at the end of the Messinian Salinity Crisis: evidence from the Levant Basin, Eastern Mediterranean. *Basin Res* 19:1–18
- Betzler C, Braga JC, Martin JM, Sanchez-Almazo IM, Lindhorst S (2006) Closure of a seaway: stratigraphic record and facies (Guadix basin, Southern Spain). *Int J Earth Sci* 95:903–910
- Betzler C, Braga JC, Jaramillo-Vogel D, Römer M, Hübscher C, Schmiedl G, Lindhorst S (2010) Late Pleistocene and Holocene cool-water carbonates of the Western Mediterranean Sea. *Sedimentology*. doi:10.1111/j.1365-3091.2010.01177.x
- Blanc P-L (2000) Of sills and straits: a quantitative assessment of the Messinian Salinity Crisis. *Deep Sea Res I Oceanogr Res Pap* 47:1429–1460
- Blanc PL (2002) The opening of the Plio-Quaternary Gibraltar Strait: assessing the size of a cataclysm. *Geodin Acta* 15:303–317
- Blanc P-L (2006) Improved modelling of the Messinian Salinity Crisis and conceptual implications. *Palaeogeogr Palaeoclimatol Palaeoecol* 238:349–372
- Bouhadad Y (2001) The Murdjado, Western Algeria, fault-related fold: implications for seismic hazard. *J Seismol* 5:541–558
- Bourgeois J, Mauffret A, Ammar A, Demnati A (1992) Multichannel seismic data imaging of inversion tectonics of the Alboran Ridge (western Mediterranean Sea). *Geo-Mar Lett* 12(2/3):117–122. doi:10.1007/BF02084921
- Bridge C, Calon TJ, Hall J, Aksu AE (2005) Salt tectonics in two convergent-margin basins of the Cyprus arc, Northeastern Mediterranean. *Mar Geol* 221:223–259
- Butler RWH, McClelland E, Jones RE (1999) Calibrating the duration and timing of the Messinian salinity crisis in the Mediterranean: linked tectonoclimatic signals in thrust-top basins of Sicily. *J Geol Soc* 156:827–835
- Campillo AC, Maldonado A, Mauffret A (1992) Stratigraphic and tectonic evolution of the western Alboran Sea: late Miocene to Recent. *Geo-Mar Lett* 12(2/3):165–172. doi:10.1007/BF02084928
- CIESM (2008) The Messinian Salinity Crisis from mega-deposits to microbiology—A consensus report. CIESM, Monaco
- Clauzon G, Suc J-P, Gautier F, Berger A, Loutre M-F (1996) Alternate interpretation of the Messinian salinity crisis: controversy resolved? *Geology* 24:363–366
- Cohen A (1993) Halite-clay interplay in the Israeli Messinian. *Sediment Geol* 86:211–228
- Comas MC, Platt JP, Soto JJ, Watts AB (1999) The origin and tectonic history of the Alboran Basin: insights from Leg 161 results. In: Zahn R, Comas MC, Klaus A (eds) *Proc ODP. Sci Results. Ocean Drilling Program, College Station*, pp 555–579
- Cornée JJ, Saintmartin JP, Conesa G, Muller J (1994) Geometry, paleoenvironments and relative sea-level (accommodation space) changes in the Messinian Murdjajo carbonate platform (Oran, Western Algeria) - Consequences. *Sediment Geol* 89:143–158
- Cornet A, Dalloni M, Deleau P, Flandrin J, Gautier M, Gourinard Y, Gousskov N, Laffite R (1952) *Carte géologique de l'Algérie, Echelle 1/500.000, 2ème edn.* Gouvernement Général de l'Algérie, Direction du Commerce, de l'Energie et de l'Industrie, Service de la Carte Géologique, Gaillac-Monrocq, Paris
- de Lamotte DF, Saint Bezar BA, Bracène R, Mercier E (2000) The two main steps of the Atlas building and geodynamics of the western Mediterranean. *Tectonics* 19:740–761
- Dewey JF, Helman ML, Knott SD, Turco E, Hutton DHW (1989) Kinematics of the western Mediterranean. *Geol Soc Lond Spec Publ* 45:265–283
- Dingle RV (1977) The anatomy of a large submarine slump on a sheared continental margin (SE Africa). *J Geol Soc* 134:293–310
- Domzig A, Yelles K, Le Roy C, Déverchère J, Bouillin J-P, Bracène R, Mercier de Lépinay B, Le Roy P, Calais E, Kherroubi A, Gaullier V, Savoye B, Pauc H (2006) Searching for the Africa-Eurasia Miocene boundary offshore western Algeria (MAR-ADJA'03 cruise). *C R Geosci* 338:80–91
- Duggen S, Hoernle K, van den Bogaard P, Harris C (2004) Magmatic evolution of the Alboran region: the role of subduction in forming the western Mediterranean and causing the Messinian Salinity Crisis. *Earth Planet Sci Lett* 218:91–108
- Esteban M, Braga JC, Martin JM, Santisteban C (1996) Western Mediterranean reef complexes. In: Franseen EK, Esteban M, Ward WC, Rouchy JM (eds) *Models for carbonate stratigraphy from Miocene reef complexes of Mediterranean regions*. SEPM, Tulsa, pp 55–72
- Faccenna C, Becker TW, Lucente FP, Jolivet L, Rossetti F (2001) History of subduction and back-arc extension in the Central Mediterranean. *Geophys J Int* 145:809–820
- García-Castellanos D, Estrada F, Jiménez-Munt I, Gorini C, Fernández M, Vergés J, De Vicente R (2009) Catastrophic flood of the Mediterranean after the Messinian salinity crisis. *Nature* 462:778–781
- Garfunkel Z, Almogor G (1984) Geology and structure of the continental-margin off Northern Israel and the adjacent part of the Levantine Basin. *Mar Geol* 62:105–131
- Gargani J, Rigollet C (2007) Mediterranean Sea level variations during the Messinian salinity crisis. *Geophys Res Lett* 34:L10405. doi:10.1029/2007GL029885
- Gelabert B, Sabat F, Rodriguez-Perea A (2002) A new proposal for the late Cenozoic geodynamic evolution of the western Mediterranean. *Terra Nova* 14:93–100
- Gueguen E, Doglioni C, Fernandez M (1998) On the post-25 Ma geodynamic evolution of the western Mediterranean. *Tectonophysics* 298:259–269
- Hall J, Calon TJ, Aksu AE, Meade SR (2005) Structural evolution of the Latakia Ridge and Cyprus Basin at the front of the Cyprus Arc, Eastern Mediterranean Sea. *Mar Geol* 221:261–297
- Haq BU, Hardenbol J, Vail PR (1987) Chronology of fluctuating sea levels since the Triassic. *Science* 235:1156–1167
- Hoernle K, Duggen S, Geldmacher J, Klügel A, party sbs (eds) (2003) *METEOR Cruise No. 51, Leg 1, Vulkosa: Vulkanismus Ostatlantik-Alboran*. GEOMAR, Kiel
- Hsü KJ, Ryan WBF, Cita MB (1973) Late Miocene desiccation of the Mediterranean. *Nature* 242:240–244
- Hübscher C, Cartwright J, Cypionka H, De Lange GJ, Robertson A, Suc J-P, Urai JL (2007) Global look at salt giants. *Eos Trans AGU* 88(16):177. doi:10.1029/2007EO160002
- Hübscher C, Tahchi E, Klauke I, Maillard A, Sahling H (2009) Salt tectonics and mud volcanism in the Latakia and Cyprus Basins, eastern Mediterranean. *Tectonophysics* 470:173–182
- Hübscher C, Betzler C, Grevemeyer I (eds) (2010) *Sedimentology, rift-processes and neotectonic in the western Mediterranean, Cruise No. 69, August 08 - September 20, 2006. Meteor-Berichte 10-1*, Universität Hamburg, Hamburg
- Jenkyns HC, Sellwood BW, Pomar L (1990) A field guide to the Island of Mallorca. *Geologists' Association, London*
- Jolivet L, Faccenna C (2000) Mediterranean extension and the Africa-Eurasia collision. *Tectonics* 19:1095–1106
- Lewis KB (1971) Slumping on a continental slope inclined at 1°–4°. *Sedimentology* 16:97–110
- Locat J, Lee HJ (2002) Submarine landslides: advances and challenges. *Can Geotech J* 39:193–212
- Lofi J, Gorini C, Berné S, Clauzon G, Tadeu Dos Reis A, Ryan WBF, Steckler MS (2005) Erosional processes and paleo-environmental changes in the Western Gulf of Lions (SW France) during the Messinian Salinity Crisis. *Mar Geol* 217:1–30
- Lofi J, Déverchère J, Gaullier V, Gillet H, Gorini C, Guennoc P, Loncke L, Maillard A, Sage F, Thinin I (eds) (2010) *Atlas of the Messinian seismic markers in the Mediterranean and Black Seas*. CCGM, Paris (in press)

- Loncke L, Mascle J, Parties FS (2004) Mud volcanoes, gas chimneys, pockmarks and mounds in the Nile deep-sea fan (Eastern Mediterranean): geophysical evidences. *Mar Petrol Geol* 21:669–689
- Loncke L, Gaullier V, Mascle J, Vendeville B, Camera L (2006) The Nile deep-sea fan: an example of interacting sedimentation, salt tectonics, and inherited subsalt paleotopographic features. *Mar Petrol Geol* 23:297–315
- Maestro-González A, Bárcenas P, Vázquez JT, Díaz-del-Río V (2008) The role of basement inheritance faults in the recent fracture system of the inner shelf around Alboran Island, Western Mediterranean. *Geo-Mar Lett* 28(1):53–64. doi:10.1007/s00367-007-0089-8
- Maillard A, Gorini C, Mauffret A, Sage F, Lofi J, Gaullier V (2006) Offshore evidence of polyphase erosion in the Valencia Basin (Northwestern Mediterranean): scenario for the Messinian Salinity Crisis. *Sediment Geol* 188(189):69–91
- Maillard A, Hübscher C, Benkhelil J, Tahchi E (2010) Deformed Messinian markers in the Cyprus Arc: tectonic and/or Messinian Salinity Crisis indicators? *Basin Res* (in press). doi:10.1111/j.1365-2117.2010.00464.x
- Maldonado A, Campillo AC, Mauffret A, Alonso B, Woodside J, Campos J (1992) Alboran Sea late Cenozoic tectonic and stratigraphic evolution. *Geo-Mar Lett* 12(2/3):179–186. doi:10.1007/BF02084930
- Mann J (2002) Extensions and applications of the Common-Reflection-Surface Stack Method. Logos, Berlin
- Mart Y, Bengai Y (1982) Some depositional patterns at the continental-margin of the Southeastern Mediterranean Sea. *AAPG Bull* 66:460–470
- Martín JM, Braga JC, Betzler C (2001) The Messinian Guadalhorce corridor: the last northern, Atlantic-Mediterranean gateway. *Terra Nova* 13:418–424
- Meijer PT, Krijgsman W (2005) A quantitative analysis of the desiccation and re-filling of the Mediterranean during the Messinian Salinity Crisis. *Earth Planet Sci Lett* 240:510–520
- Montadert L, Sancho J, Fail JP, Debyser J, Winnock E (1970) De l'âge tertiaire de la série salifère responsable des structures diapiriques en Méditerranée Occidentale (Nord-Est des Baléares). *C R Acad Sci* 271:812–815
- Montigny R, Edel JB, Thuizat R (1981) Oligo-Miocene rotation of Sardinia: K-Ar ages and paleomagnetic data of Tertiary volcanics. *Earth Planet Sci Lett* 54:261–271
- Müller RD, Sdrolias M, Gaina C, Steinberger B, Heine C (2008) Long-term sea-level fluctuations driven by ocean basin dynamics. *Science* 319:1357–1362
- Pomar L (1979) La evolución tectonosedimentaria de las Baleares: análisis crítico. *Acta Geol Hisp* 14:293–310
- Pomar L (2001) Ecological control of sedimentary accommodation: evolution from a carbonate ramp to rimmed shelf, Upper Miocene, Balearic Islands. *Palaeogeogr Palaeoclimatol Palaeoecol* 175:249–272
- Pomar L, Ward WC (1994) Response of a late Miocene Mediterranean reef platform to high-frequency eustasy. *Geology* 22:131–134
- Pomar L, Ward WC (1995) Sea-level changes, carbonate production and platform architecture: the Lluçmajor Platform, Mallorca, Spain. In: Haq BU (ed) *Sequence stratigraphy and depositional response to eustatic, tectonic and climate forcing*. Kluwer, Amsterdam, pp 87–112
- Reeder MS, Rothwell G, Stow DAV (2002) The Sicilian gateway: anatomy of the deep-water connection between East and West Mediterranean basins. *Geol Soc Lond Mem* 22:171–189
- Riding R, Braga JC, Martín JM, Sánchez-Almazo IM (1998) Mediterranean Messinian Salinity Crisis: constraints from a coeval marginal basin, Sorbas, southeastern Spain. *Mar Geol* 146:1–20
- Rizzini A, Vezzani F, Cococetta V, Milad G (1978) Stratigraphy and sedimentation of a Neogene-Quaternary section in the Nile delta area. *Mar Geol* 27:327–348
- Rouchy JM, Caruso A (2006) The Messinian salinity crisis in the Mediterranean basin: a reassessment of the data and an integrated scenario. *Sediment Geol* 188(189):35–67
- Rouchy JM, Saint Martin JP (1992) Late Miocene events in the Mediterranean as recorded by carbonate-evaporite relations. *Geology* 20:629–632
- Ryan WBF (2009) Decoding the Mediterranean salinity crisis. *Sedimentology* 56:95–136
- Ryan WBF, Cita MB (1978) Nature and distribution of Messinian erosional surfaces—indicators of a several-kilometer-deep Mediterranean in the Miocene. *Mar Geol* 27:193–230
- Sage F, Von Gronefeld G, Déverchère J, Gaullier V, Maillard A, Gorini C (2005) Seismic evidence for Messinian detrital deposits at the western Sardinia margin, northwestern Mediterranean. *Mar Petrol Geol* 22:757–773
- Savoye B, Piper DJW (1991) The Messinian event on the margin of the Mediterranean Sea in the Nice area, southern France. *Mar Geol* 97:279–304
- Stampfli GM, Höcker CFW (1989) Messinian palaeorelief from 3-D seismic survey in the Tarraco concession area (Spanish Mediterranean Sea). *Geol Mijnb* 68:201–210
- Vegas R (1992) The Valencia trough and the origin of the western Mediterranean basins. *Tectonophysics* 203:249–261